

Ventricular Electromechanics in Chronic Myocardial Infarction with Substrate for Sudden Cardiac Death

心臓突然死の基質を有する慢性心筋梗塞における
心室エレクトロメカニクス

Hiroshi Ashikaga, MD
足利 洋志

A dissertation submitted to the University of Tokyo in conformity with
the requirements for the degree of Doctor of Philosophy.

Tokyo, Japan
2007

Copyright © 2007 by Hiroshi Ashikaga
All rights reserved.

Contents

	<i>Page</i>
Chapter 1 Specific aims	... 6
Chapter 2 Sudden cardiac death	... 8
2.1 Definition	... 9
2.2 Epidemiology	... 9
2.3 Etiology	... 9
2.4 Implantable cardioverter-defibrillator	... 10
2.5 Clinical need for noninvasive risk assessment of sudden cardiac death	... 11
Chapter 3 Cardiac electromechanics	... 13
3.1 Cardiac microstructures	... 14
3.1.1 Spiral fiber orientation	... 14
3.1.2 Laminar sheet structure	... 16
3.2 Cardiac electrophysiology	... 18
3.2.1 Electrical activation sequence	... 18
3.2.2 Recording cardiac electrophysiology	... 19
3.3 Cardiac mechanics	... 20
3.3.1 Lagrangian Green's strain tensor	... 20
3.3.2 Regional mechanics with transmural bead set	... 23
3.3.3 Global mechanics with MRI	... 27
Chapter 4 Regional mechanics during relaxation in normal heart	... 32
4.1 Abstract	... 33
4.2 Introduction	... 33
4.3 Materials and Methods	... 34
4.3.1 Surgical preparation	... 34
4.3.2 Experimental protocol	... 34
4.3.3 Spherical correction and 3-D reconstruction of cineradiographic images	... 36
4.3.4 Histology	... 36
4.3.5 Strain analysis	... 36
4.3.6 Statistical analysis	... 37

4.4 Results	... 38
4.4.1 Hemodynamic parameters	... 38
4.4.2 Fiber and sheet orientation	... 38
4.4.3 Strains during early relaxation in cardiac coordinates	... 39
4.4.4 Strains during early relaxation in fiber-sheet coordinates	... 39
4.5 Discussion	... 41
4.5.1 Fiber and sheet orientation	... 41
4.5.2 Left ventricular mechanics during early relaxation	... 42
4.5.3 Limitations	... 44
4.6 Conclusions	... 44
Chapter 5 Regional mechanics during relaxation in hypertrophied heart	... 45
5.1 Abstract	... 46
5.2 Introduction	... 46
5.3 Materials and Methods	... 46
5.3.1 Experimental protocol	... 46
5.3.2 Histology	... 48
5.3.3 Finite strain analysis	... 48
5.3.4 Statistical analysis	... 49
5.4 Results	... 50
5.4.1 Hemodynamic parameters	... 50
5.4.2 Transmural fiber and sheet angles	... 50
5.4.3 Strain time course	... 51
5.5 Discussion	... 55
5.5.1 Diastolic hemodynamics and volume overload hypertrophy	... 55
5.5.2 Diastolic fiber and sheet mechanics and volume overload hypertrophy	... 56
5.5.3 Limitations	... 57
5.6 Conclusions	... 58
Chapter 6 Regional electromechanics in normal heart	... 59
6.1 Abstract	... 60
6.2 Introduction	... 60
6.3 Materials and Methods	... 60
6.3.1 Experimental protocol	... 60
6.3.2 Histology	... 61
6.3.3 Data analysis	... 62
6.3.4 Statistical analysis	... 63
6.4 Results	... 63
6.4.1 Fiber orientation	... 63
6.4.2 Myofiber mechanics	... 63
6.4.3 Bipolar electrical recordings	... 67
6.5 Discussion	... 68
6.5.1 Transmural sequence of electrical activation and myofiber shortening	... 68
6.5.2 Transmural sequence of electrical repolarization and myofiber relaxation	... 68
6.5.3 Clinical implications	... 70

6.5.4 Limitations	... 70
6.6 Conclusions	... 70
Chapter 7 Regional electromechanics in paced heart	... 71
7.1 Abstract	... 72
7.2 Introduction	... 72
7.3 Materials and Methods	... 73
7.3.1 Experimental protocol	... 73
7.3.2 Statistical analysis	... 76
7.4 Results	... 76
7.4.1 End-systolic wall thickening and fiber-sheet strains during epicardial pacing	... 77
7.4.2 Time course of finite strains at the pacing site	... 77
7.4.3 Transmural mechanical activation sequence at the pacing site	... 79
7.5 Discussion	... 80
7.5.1 Mechanism of impaired endocardial wall thickening at the epicardial pacing site	... 80
7.5.2 Reversal of transmural mechanical activation	... 81
7.5.3 Limitations	... 81
7.6 Conclusions	... 81
Chapter 8 Global electromechanics in infarct heart	... 82
8.1 Abstract	... 83
8.2 Introduction	... 83
8.3 Materials and Methods	... 83
8.3.1 Surgical procedures	... 84
8.3.2 Data acquisition	... 84
8.3.3 Data analysis	... 85
8.3.4 Statistical analysis	... 86
8.4 Results	... 86
8.4.1 Infarct map	... 86
8.4.2 Electrical activation map	... 87
8.4.3 Strain map	... 88
8.5 Discussion	... 91
8.5.1 Impact of infarct geometry on electromechanical properties in the infarct zone	... 91
8.5.2 Mechanism of impaired systolic function in the infarct border zone	... 91
8.5.3 Limitations	... 92
8.6 Conclusions	... 92
Chapter 9 Global electromechanics in infarct heart with substrate for sudden cardiac death	... 93
9.1 Abstract	... 94
9.2 Introduction	... 94
9.3 Materials and Methods	... 95
9.3.1 Creation of myocardial infarction	... 95
9.3.2 <i>In vivo</i> MRI	... 95
9.3.3 Electrical recording system	... 96

9.3.4 Induction of monomorphic ventricular tachycardia	... 97
9.3.5 Postmortem studies	... 97
9.3.6 Data processing	... 97
9.3.7 Electromechanical data registration	...100
9.3.8 Statistical analysis	...100
9.4 Results	...100
9.4.1 General parameters	...100
9.4.2 Infarct geometry	...102
9.4.3 Characteristics of prestretch	...103
9.4.4 Correlation between prestretch and electromechanical indices	...106
9.5 Discussion	...110
9.5.1 Overview	...110
9.5.2 Animal model of chronic myocardial infarction with substrate for sudden cardiac death	...111
9.5.3 Mechanical characteristics of prestretch in chronic myocardial infarction	...111
9.5.4 Prestretch and stretch-induced arrhythmia	...111
9.5.5 Clinical implications	...112
9.5.6 Limitations	...112
9.6 Conclusions	...112
Chapter 10 Thesis conclusions	...113
<i>Bibliography</i>	...115
<i>Acknowledgement</i>	...127
<i>List of Abbreviations and Acronyms</i>	...128
<i>List of Figures and Tables</i>	...130

Chapter 1

Specific aims

The overall goal of the thesis is to assess anatomical correlation between cardiac mechanics and electrophysiology *in vivo*, and to investigate whether it is possible to predict electrical behaviors from mechanical behaviors of the heart. There are six specific aims to achieve this goal. Specific aims 1 and 2 focused on assessment of regional cardiac mechanics and correlated it to cardiac microstructures such as fibers and sheets. Specific aims 3 and 4 investigated the correlation between the regional cardiac mechanics and the transmural electrical activation sequence. Specific aims 5 and 6 focused on the anatomical correlation between cardiac mechanics and electrophysiology at the global ventricular level.

Aim 1: To conduct detailed assessment of regional left ventricular (LV) mechanics during relaxation in normal heart. The structure(s) contributing to diastolic recoil (e.g., myocardial fibers) would demonstrate the earliest and most prominent return to diastolic configuration during early relaxation. To investigate the contribution of the fiber and sheet structures to LV mechanics during early relaxation, three-dimensional (3-D) finite deformation was determined in the LV anterior wall during early relaxation in normal dog hearts *in vivo* (Chapter 4).

Aim 2: To conduct detailed assessment of regional LV mechanics during relaxation in hypertrophied heart. To test the hypothesis that the changes in passive properties in chronic volume-overload heart failure are associated with abnormal sheet mechanics during diastolic filling, myocardial 3-D finite deformation in the LV anterior wall of dogs *in vivo* in volume-overload hypertrophy was determined. The time course of myocardial strains in fiber-sheet coordinates referred to the end-diastolic configuration was determined during diastolic filling. Thus the dynamic changes were studied during diastolic filling at the level of myofibers and sheet structures before and after development of diastolic dysfunction (Chapter 5).

Aim 3: To conduct detailed assessment of regional electromechanics in normal heart. To test the hypothesis that there is transmural dispersion of both myofiber shortening and relaxation, the time course of transmural myofiber mechanics and electrical sequence of activation and repolarization in the LV anterior wall of normal canine heart *in vivo* were studied using transmurally implanted mechanical markers and plunge electrodes, respectively (Chapter 6).

Aim 4: To conduct detailed assessment of regional electromechanics in paced heart. To test the hypothesis that LV epicardial pacing would reverse transmural mechanical activation sequence and thereby mitigate normal transmural deformation, the effects of LV epicardial pacing on transmural fiber-sheet mechanics were investigated by determining 3-D finite deformation during normal atrioventricular (AV) conduction and LV epicardial pacing in the anterior wall of normal dog hearts *in vivo* (Chapter 7).

Aim 5: To conduct detailed assessment of global electromechanics in infarct heart. To test the hypothesis that alterations in electrical activation sequence contribute to depressed systolic function in the infarct border zone, the anatomical correlation of abnormal electromechanics with reference to infarct geometry was qualitatively and quantitatively examined in a canine model of chronic myocardial infarction (MI) (Chapter 8).

Aim 6: To conduct detailed assessment of global electromechanics in infarct heart with substrate for SCD. To test the hypothesis that abnormal mechanical stretch (“prestretch”) in chronic MI with a substrate for SCD alters the local action potential duration (APD) *in vivo*, the anatomical correlation between prestretch and activation recovery intervals (ARI) was quantitatively examined in a swine model of chronic MI where sustained monomorphic ventricular tachycardia (VT) is inducible with programmed electrical stimulation (PES) (Chapter 9).

Chapter 2

Sudden cardiac death

2.1 Definition

Sudden cardiac death (SCD) is defined as the unexpected natural death from a cardiac cause within a short time period, generally less than 1 hour from the onset of symptoms, in a person without any prior condition that would appear fatal (269, 270). The definition of SCD strongly influences epidemiological data (145). The proportion of all natural deaths due to SCD is 13% when a definition of 1 hour from onset of symptoms is used, and 18.5% when a definition of 24 hour is used (74); the application of a 24-hour definition of SCD increases the fraction of all natural deaths falling into the “sudden” category but reduces the proportion of all sudden natural deaths of cardiac origins (145). Approximately a half of all deaths in coronary heart disease (CHD) are sudden and unexpected, occurring shortly after the onset of a change in clinical status, with some geographical variation in the fraction of coronary deaths that are sudden (101).

2.2 Epidemiology

The incidence of SCD depends on the prevalence of CHD in different regions (201). Estimates for the US (60, 85, 102, 265) range from less than 200,000 to more than 450,000 SCDs annually, with the most widely used estimates in the range of 300,000 to 350,000 SCDs annually (119). The variation is based, in part, on the inclusion criteria used in individual studies. Overall, event rates in Europe are similar to those in the US (201), with significant geographic variations reported. The age-adjusted CHD mortality is decreasing, however, it does not imply a decrease in absolute numbers of cardiac or sudden deaths (119, 179); instead, it simply indicates the increasing prevalence of chronic heart disease because of the growth and aging of the US and European populations (39).

2.3 Etiology

Most SCD cases are associated with CHD; approximately 75% of SCD victims have evidence of prior myocardial infarction (MI) (180), and survivors of acute MI are at high risk of SCD, particularly within the first year (72, 159, 212). The electrical rhythm most often recorded at the time of SCD is ventricular fibrillation (VF). Previous studies suggest that 75-80% of SCD result from ventricular tachyarrhythmia (180-182), which can arise from chronic scar without active or clinically obvious myocardial ischemia (30, 171, 250, 270). The rest of SCD cases (15-20%) are attributed to bradyarrhythmias, including advanced atrioventricular (AV) block and asystole (157). Bayes de Luna *et al* (30) noted that in 157 ambulatory patients who had SCD while undergoing Holter recording, 62.4% had ventricular tachycardia (VT), 12.7% had torsades de pointes, 8.3% had primary VF, and the rest had bradyarrhythmias (16.5%). The true incidence of bradyarrhythmias is not clear because a rhythm beginning as VF may appear to be asystole when the first ECG is recorded. VF can be considered a final common pathway for the expression of an electrically unstable heart. For example, patients with CHD may develop sustained reentry VT, which is a somewhat more organized rhythm than VF. Because most VTs are hemodynamically unstable, the sustained VT induces global ischemia and eventually evolves into VF.

At present, it is not possible to predict when the asymptomatic, apparently stable, individual suddenly develops SCD. Unknown combinations of factors, including physical activity, transient ischemia, pH and electrolyte changes, inflammation, hypoxia, stretch, ion

channel abnormalities, neuroendocrine actions, drugs, may interact with a fixed substrate in the heart to precipitate the arrhythmia.

2.4 Implantable cardioverter-defibrillator

Recent prospective multicenter clinical trials demonstrate a major survival benefit with the implantable cardioverter-defibrillator (ICD) for SCD in high-risk subgroups with LV dysfunction due to prior MI and nonischemic cardiomyopathy (149) (Figure 2-1). ICD therapy, compared with conventional or traditional antiarrhythmic drug therapy, has been associated with mortality reductions from 23-55%, depending on the risk group participating in the trial, with the improvement in survival due almost exclusively to a reduction in SCD. The trials can be categorized into 2 types: primary prevention (prophylactic) trials in which the subjects have not experienced a life-threatening ventricular arrhythmia or a symptomatic equivalent, and secondary prevention trials involving subjects who have had an abortive cardiac arrest, a life-threatening VT, or unexplained syncope with work-up suggesting a high probability that a ventricular tachyarrhythmia was the cause of the syncope.

Important ICD advancements continue to occur in the transvenous implantation procedure, generator size reduction, system longevity, arrhythmia detection, and multiprogrammable features. However, it is important to remember that device failure, although rare, can occur. Current ICDs include options for single-chamber, dual-chamber, and biventricular cardiac resynchronization pacing for nonshock termination of ventricular arrhythmia in addition to multilevel shock discharge for VT or VF.

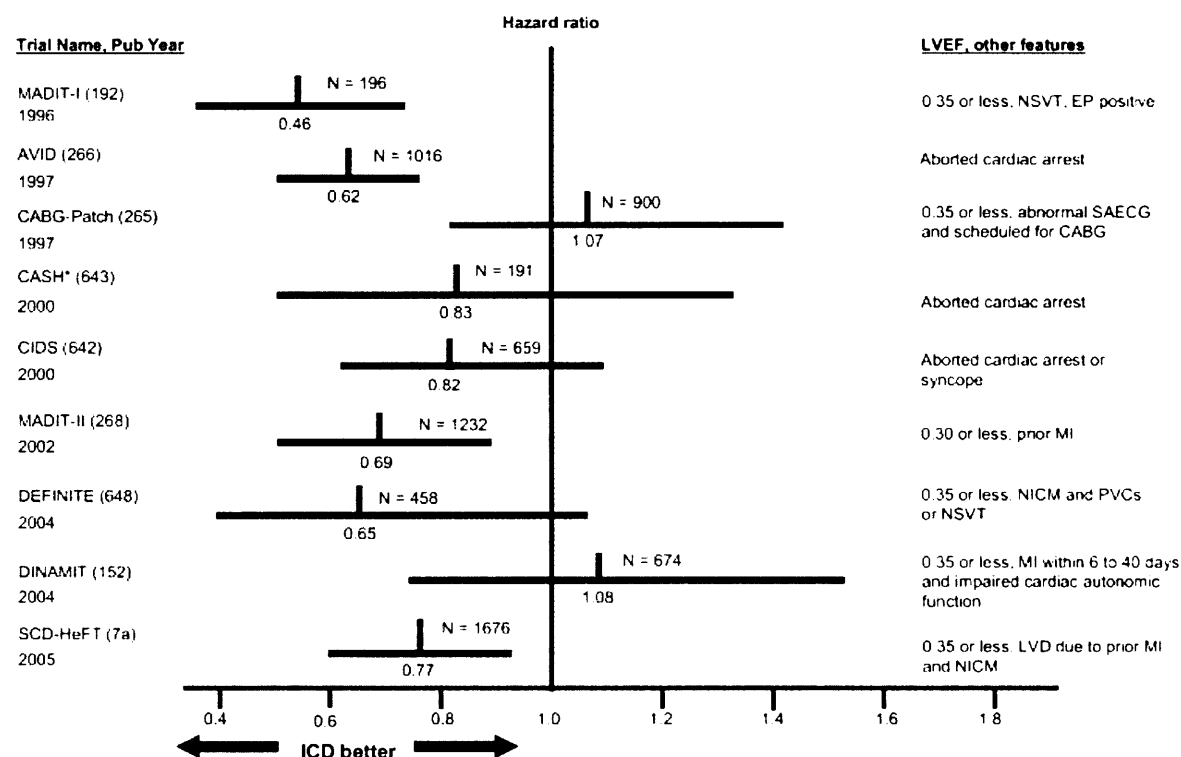


Figure 2-1. Major implantable cardioverter-defibrillator (ICD) trials (269). Hazard ratios (vertical line) and 95% confidence intervals (horizontal lines) for death from any cause in the ICD group compared with the non-ICD group. *Includes only ICD and amiodarone patients from CASH. AVID = Antiarrhythmics Versus Implantable Defibrillators; CASH = Cardiac Arrest Study Hamburg; CIDS = Canadian Implantable Defibrillator Study; EF = ejection fraction; HF = heart failure; MADIT = Multicenter Automatic Defibrillator Implantation Trial; MUSTT = Multicenter UnSustained Tachycardia Trial; SCD-HeFT = Sudden Cardiac Death in Heart Failure Trial; CABG = coronary artery bypass graft surgery; EP = electrophysiological study; LVD = left

ventricular dysfunction; MI = myocardial infarction; N = number of patients; NICM = nonischemic cardiomyopathy; NSVT = nonsustained ventricular tachycardia; PVCs = premature ventricular complexes; SAEKG = signal-averaged electrocardiogram.

Problems associated with ICD therapy include inappropriate shock discharge mostly for atrial fibrillation (AF) with rapid ventricular response, defibrillator storm with appropriate recurrent ICD discharge for recurrent ventricular tachyarrhythmias or inappropriate discharge for a variety of reasons, infections related to device implantation, and exacerbation of heart failure when a high percentage of the heartbeats are paced from the right ventricular (RV) apex, especially when ventricular function is already compromised. Potential solutions include the selection of an appropriately low minimum rate and an appropriately long atrioventricular (AV) interval. Avoidance of overly aggressive rate acceleration in rate-modulated modes and, in some recent pacemaker models, the use of an automatic pacing mode selecting algorithms that strongly favor atrial over ventricular pacing (249). The heart failure is likely to occur in the setting of advanced LV dysfunction with the ICD unit programmed to dual-chamber pacing at heart rates that dominate the rhythm, thus contributing to paced ventricular desynchronization.

2.5 Clinical need for noninvasive risk assessment of sudden cardiac death

Although the ICD trials have succeeded in identifying the subgroups at risk for SCD who benefit from ICD therapy, the target populations in ICD trials are considered relatively high risk (Figure 2-2). These subgroups constitute only a small fraction of all the SCDs, thus interventions in these subgroups do not have a major impact on the general public health problem of SCD (183). In fact, at least 50% of all SCDs due to CHD occur as a first clinical event or among subgroups of patients thought to be at relatively low risk for SCD (179). Therefore, the majority of the potential SCD victims are not protected by the current guidelines, primarily due to lack of specific markers with high predictive value (269). Inducibility of sustained monomorphic VT during the invasive electrophysiological study with PES is clinically equivalent to having an arrhythmic substrate, thus has been used as a prognosticator for subsequent mortality (47). However, its prognostic accuracy is relatively low (47, 48, 70). Moreover, its invasive nature does not warrant its use in the “unprotected” yet low-risk subgroups. It is critical to develop a noninvasive diagnostic test to safely perform the risk assessment of SCD in those “unprotected” subgroups.

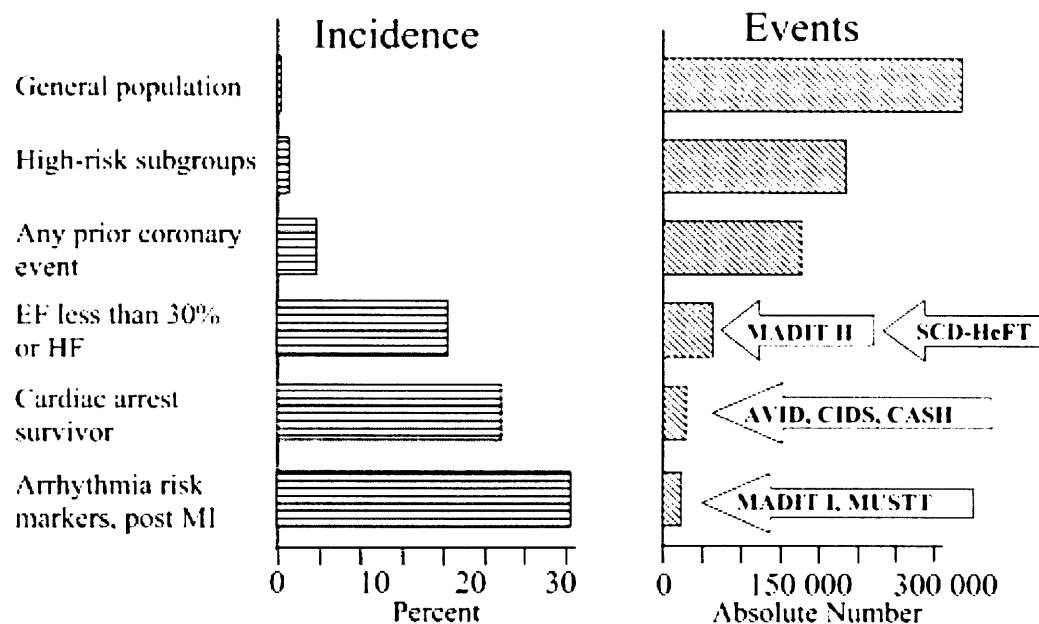


Figure 2-2. Absolute numbers of events and event rates of SCD in the general population and in specific subpopulations over 1 year (183, 269). General population refers to unselected population age greater than or equal to 35 years old, and high-risk subgroups to those with multiple risk factors for a first coronary event. Clinical trials that include specific subpopulations of patients are shown in the right side of the figure.

Chapter 3

Cardiac electromechanics

3.1 Cardiac microstructures

The primary function of the heart is mechanical: to receive blood from a source and to pump it out to a sink. A human heart contracts at 70 beats per minute (bpm), and pumps out 6 Liters of blood every minute. Despite the enormous work that the heart performs as an organ, mechanical function of individual cardiomyocytes, or fibers, that constitute the heart is not extremely spectacular. Longitudinal shortening of a contractile fiber is 15% at best, and radial thickening is only 8%, if the cell volume is assumed constant during contraction. However, a human heart reduces the volume of the LV by 60% or more and the LV wall thickens by greater than 40% during each contraction. Apparently, some kind of spatial organization of fibers is needed to connect the missing link in the structure-function relationship between the cellular and the organ levels.

3.1.1 Spiral fiber orientation

The first task is to place the contractile fibers on the surface of the LV in such a manner as to reduce the chamber volume by more than 60% when the fibers shorten by 15% (121, 211). For simplicity, the LV is assumed to be a cylindrical chamber (Figure 3-1). If the fibers are placed longitudinally, 15% fiber shortening results in a 15% reduction of chamber volume. If the fibers are placed circumferentially, 15% fiber shortening results in a 28% reduction in chamber volume. If the fibers are placed in a spiral, virtually any ejection fraction (EF) up to 100%, can be generated from spiral fibers capable of shortening by only 15%, depending only upon the cylinder dimensions and the pitch angle of the spiral.

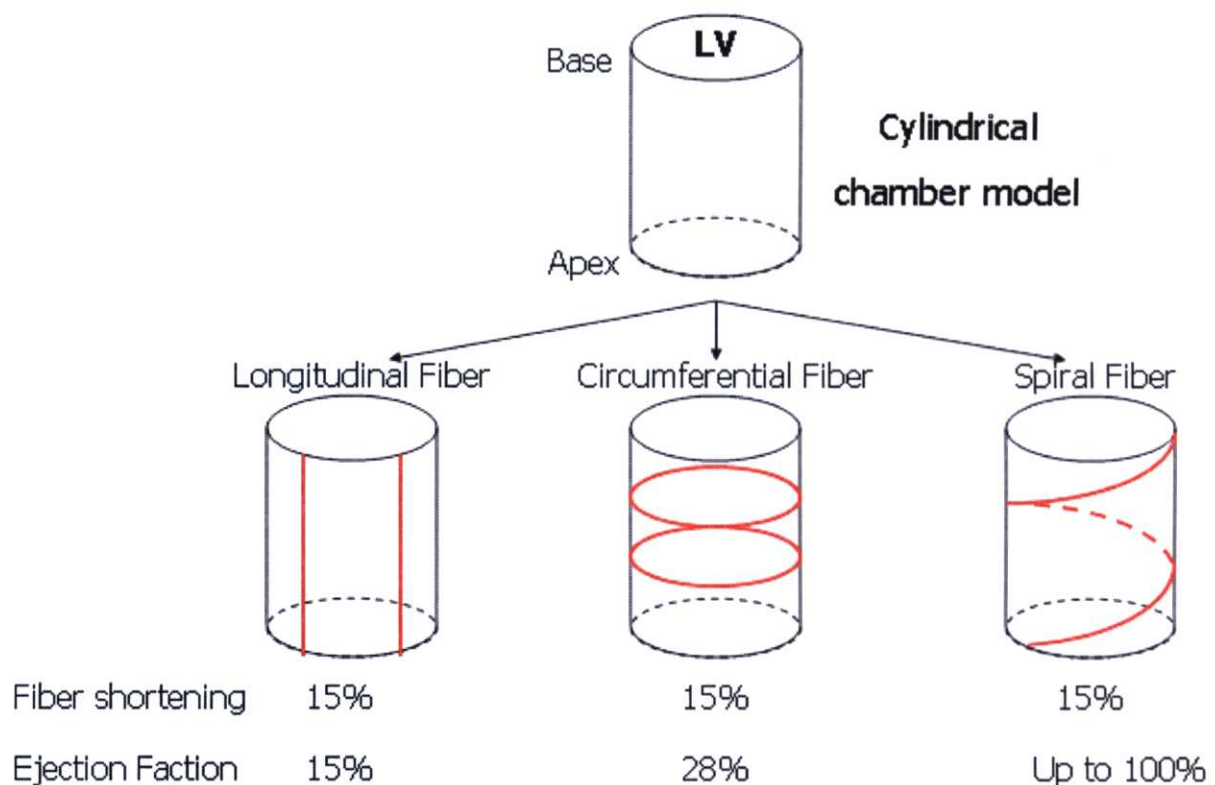


Figure 3-1. Fiber orientation and ejection fraction in a cylindrical LV model. Figure modified from (121).

However, this spiral fiber model has two problems. First, a single layer of spiral fibers cannot generate physiologic LV pressures, because such spiral fibers have a large radius of curvature, thus any force they develop does not translate maximally into LV pressure. Second, spiral fibers generate a huge torsion of the chamber with each contraction which may lead to large, inefficient shears.

In reality, myofibers mostly run parallel to the epicardial tangent plane, and the principal fiber orientation gradually rotates counterclockwise from the epicardium to the endocardium, resulting in a local spiral architecture of myofibers with a transmural angle gradient from approximately -60 degrees to positive 60 degrees (Figure 3-2) (225). This transmural fiber orientation does not significantly change from systole to diastole.

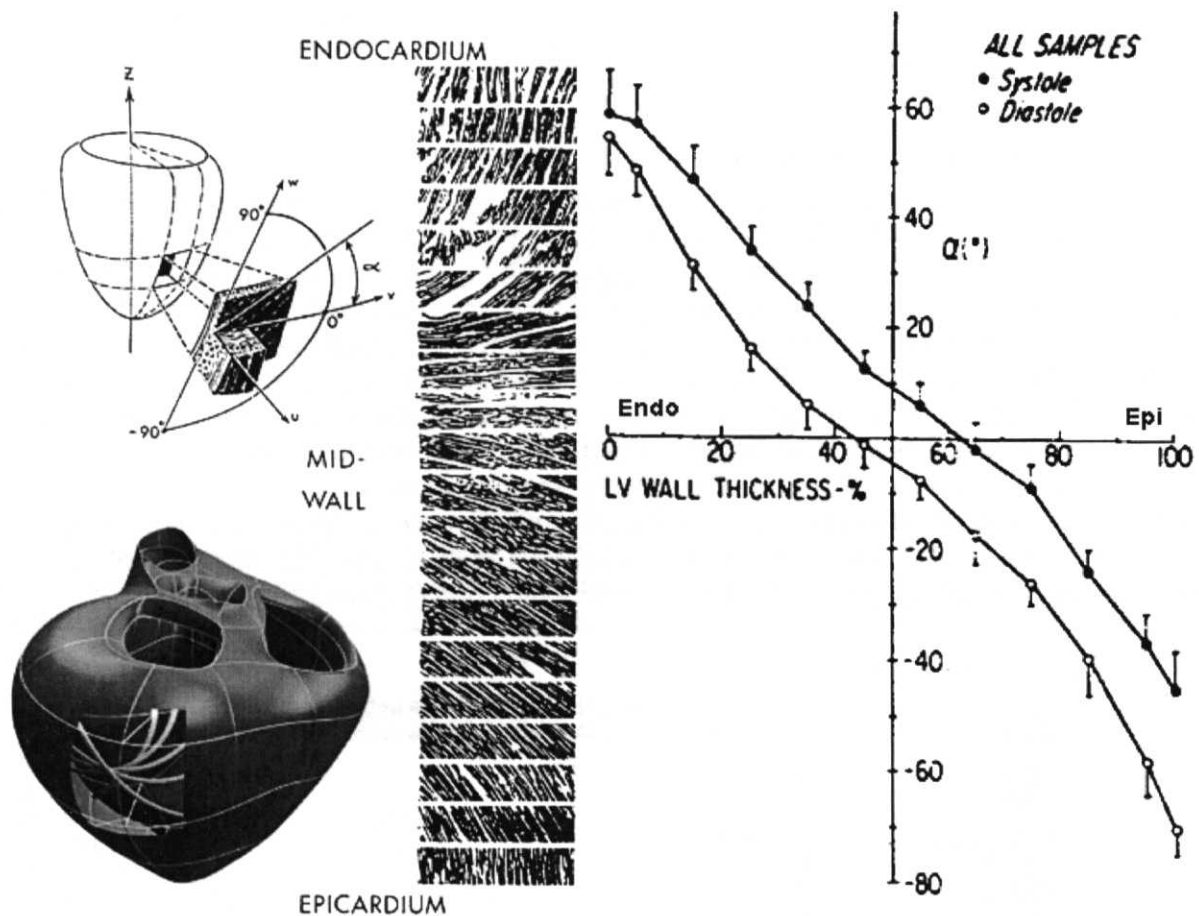


Figure 3-2. Transmural fiber orientation (218, 225).

Therefore, the real LV chamber has spiral fibers in the endocardium, circumferential fibers at midwall, and counter-spiral fibers in the epicardium (Figure 3-3) (13, 15, 121). Spiral fibers help generate large EF, and circumferential fibers help generate physiological LV pressures, because tension developed in circumferential fibers translates optimally to pressure within the chamber. The combination of spiral and counter-spiral fibers help minimize global LV torsional deformation. In addition, the local spiral architecture of myofibers helps equalize transmural fiber strain and stress.

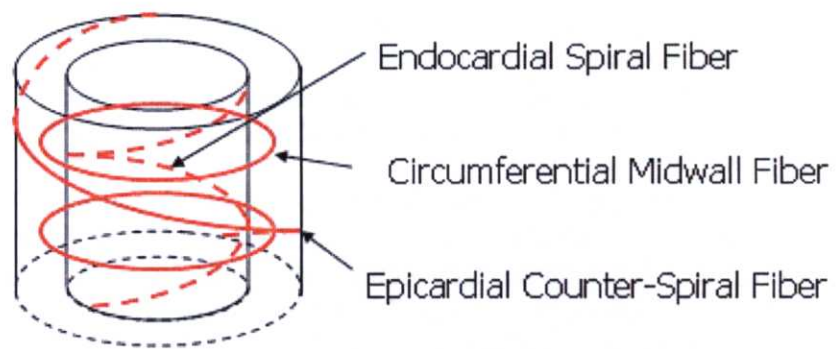


Figure 3-3. Transmurular fiber structure. Combination of spiral and circumferential fibers 1) generates large EF (>60%), 2) generates physiological LV pressures, 3) minimizes global LV torsional deformation, and 4) equalizes transmural fiber strain and stress. Figure modified from (121).

3.1.2 Laminar sheet structure

The next task is to organize the contractile fibers in the LV wall so that the LV wall thickens greater than 40% when radial fiber thickening is only 8%. In 1973, Spotnitz *et al.* discovered the phenomenon now termed myofiber rearrangement during contraction (Figure 3-4) (222). They examined the number of fibers per unit area (shown in red), and the number of fibers across the wall (shown in green), with different wall thickness in rat hearts. They found that the number of fibers per unit area decreases as the wall thickens, which reflects fiber thickening, whereas the number of fibers across the wall increases as the wall thickens. Therefore, the change in wall thickness is primarily determined by a change in the number of fibers across the wall. As the wall thickens, fibers are displaced by shearing along the myocardial cleavage planes perpendicular to fibers. The myocardial unit between these cleavage planes are called myocardial lamina or sheet, which are approximately four cells thick (150). The direction of sheets or cleavage planes is always perpendicular to the fiber direction (Figure 3-5).

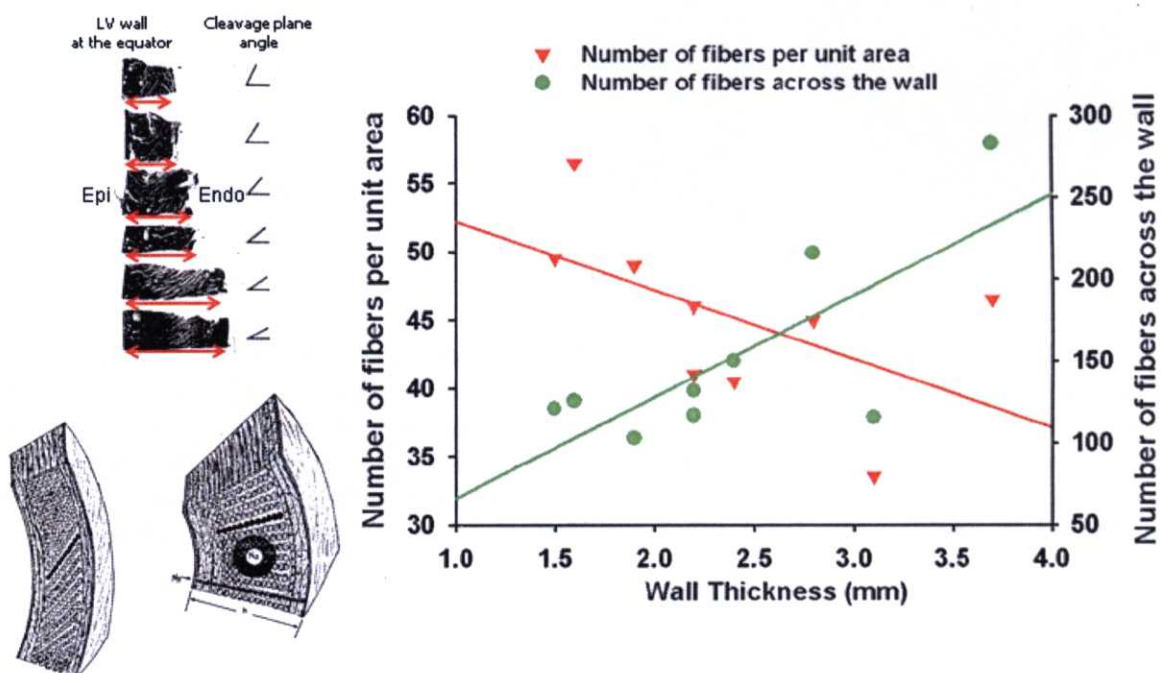


Figure 3-4. Systolic shearing of fibers along cleavage planes (222).

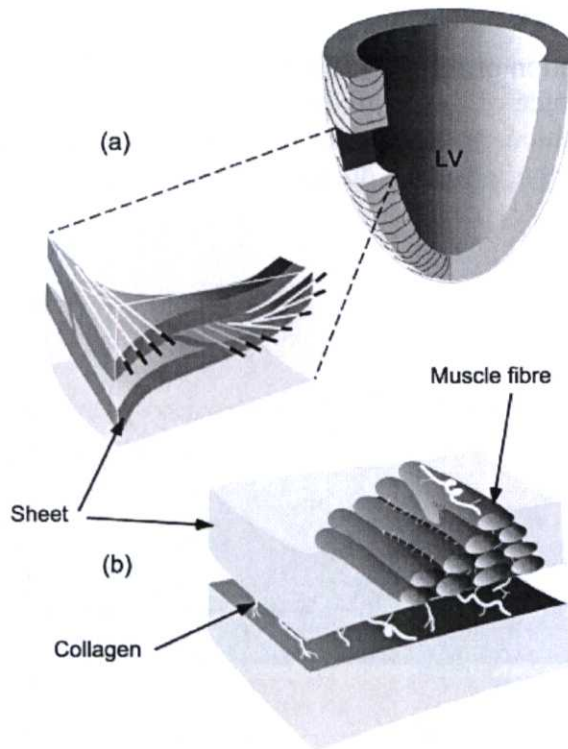


Figure 3-5. Laminar sheet structure (218).

In 1999, Costa *et al.* demonstrated that systolic wall thickening is almost exclusively accounted for by sheet shear and sheet extension (66). In Figure 3-6, sheet shear increases the wall thickness from T_0 to T_1 , and sheet extension increases the wall thickness from T_1 to T_2 . The combination of the sheet shear and extension allows systolic wall thickening of greater than 40%, from T_0 to T_2 .

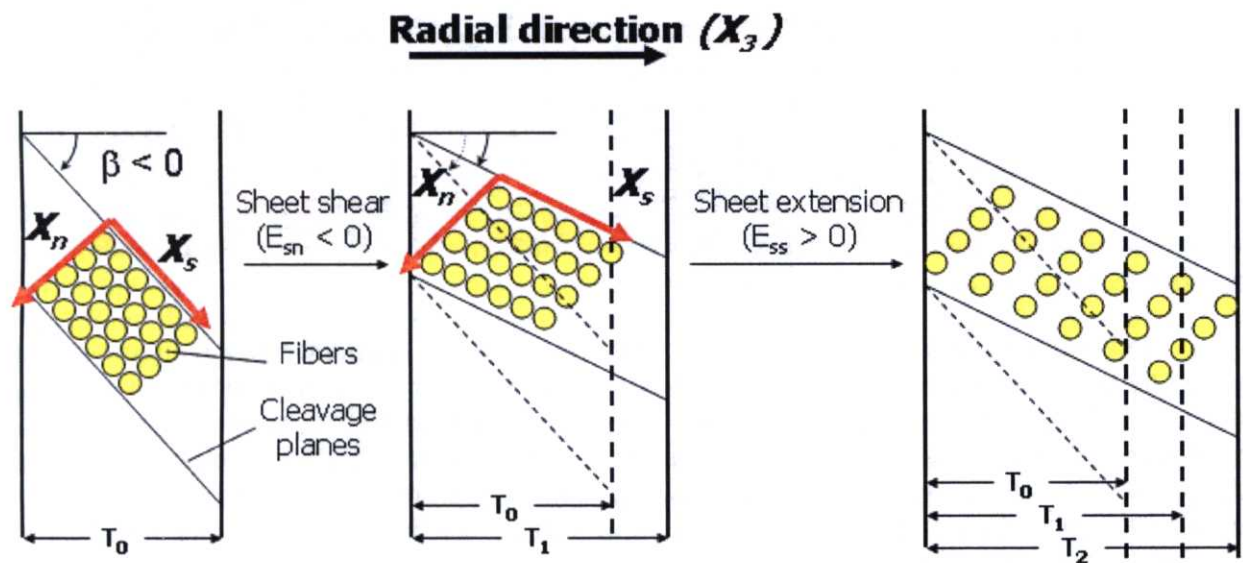


Figure 3-6. Sheet shear and extension allow systolic wall thickening of >40%. Each circle represents a cross-section of myofiber. X_n , direction normal to the sheet; X_s , sheet direction; X_3 , radial direction; β , sheet angle; E_{sn} , sheet shear; E_{ss} , sheet extension. Figure modified from Costa *et al* (66).

3.2 Cardiac electrophysiology

3.2.1 Electrical activation sequence

In cardiomyocytes, electrical activation or depolarization occurs by the inflow of sodium ions across the cell membrane. The amplitude of the action potential is approximately 100 mV. A plateau phase follows cardiac depolarization, and thereafter repolarization takes place mainly as a consequence of the outflow of potassium ions. The duration of the action impulse is about 300 ms (Figure 3-7).

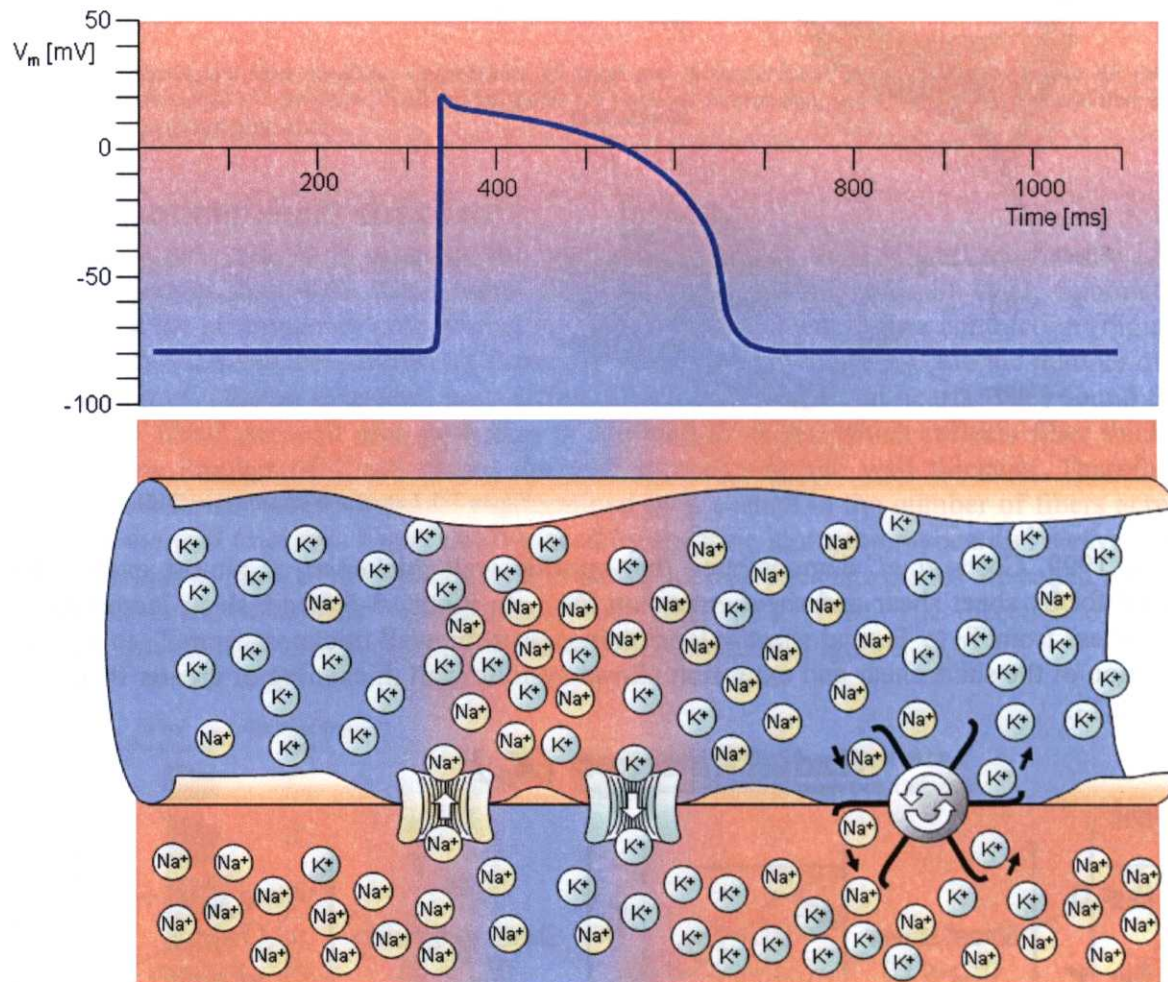


Figure 3-7. Cardiac action potential (162).

In cardiac muscle, activation can propagate from one cell to another in any direction; as a result, the activation wavefronts are rather complex. The only exception is the boundary between the atria and ventricles, which the activation wave normally cannot cross except along a special conduction system, since a nonconducting barrier of fibrous tissue is present. A classical study of the propagation of excitation in human heart was made by Durrer *et al.* (Figure 3-8) (79). They isolated the heart from a subject who had died of various cerebral conditions and who had no previous history of cardiac diseases. The heart was removed within 30 minutes postmortem and was perfused. Up to 870 electrodes were placed in the heart, and the activation sequence was recorded with a temporal resolution better than 1 ms. The isochrone surfaces show clearly that

ventricular activation starts from the endocardial wall of the left ventricle and proceeds radially toward the epicardium. In the terminal part of ventricular activation, the excitation wavefront proceeds more tangentially.

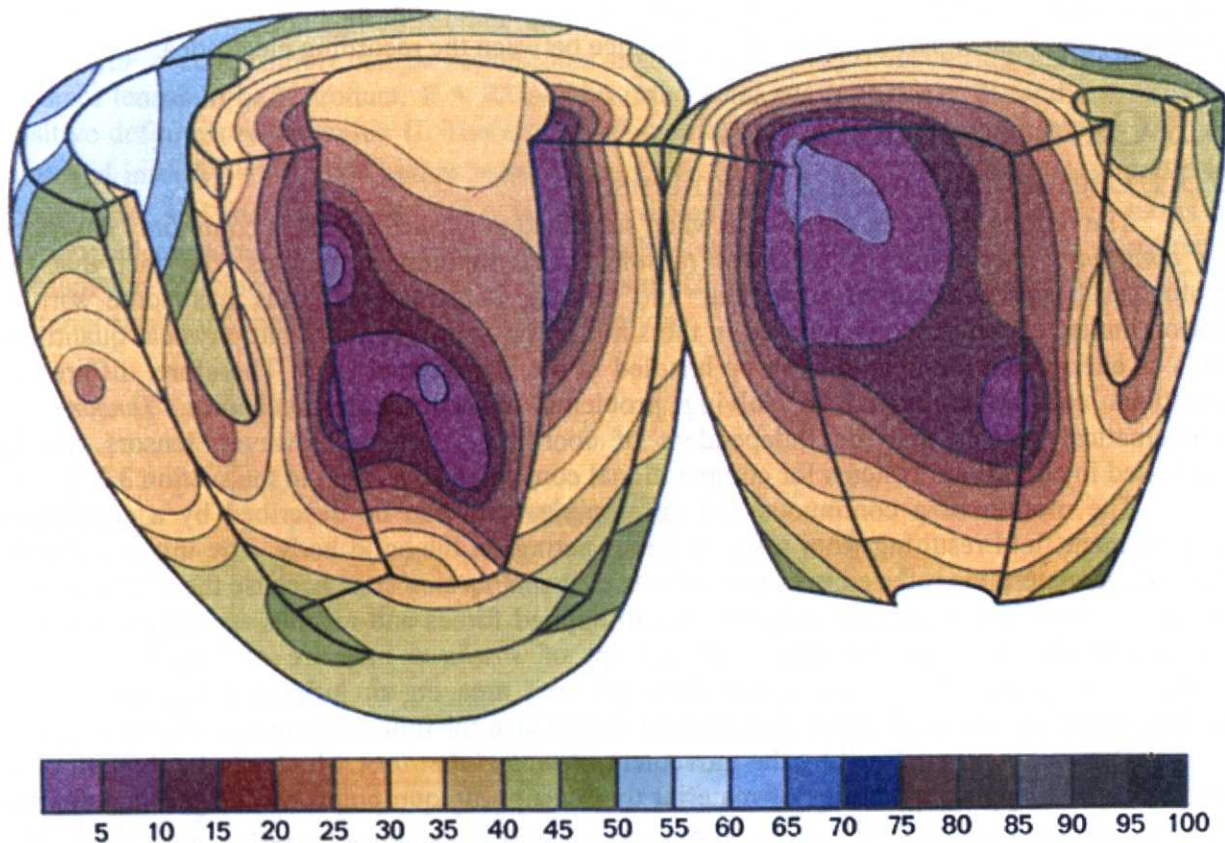


Figure 3-8. 3-D isochronic representation of the activation of the human heart (79). Zero time is the beginning of the LV potential.

3.2.2 Recording cardiac electrophysiology

Clinical electrogram recordings are differential recordings from one source that is connected to the negative input of the recording amplifier and a second source that is connected to the positive input (224).

Unipolar recordings are obtained by positioning the exploring electrode in the heart and the second, indifferent, electrode distant from the heart such that it has little or no cardiac signal. The morphology of the unipolar recording indicates the direction of wavefront propagation. When the exploring electrode is located at the site of initial activation, depolarization produces a wavefront that spreads away from the electrode generating a monophasic QS-complex. The major disadvantage of unipolar recordings is that they contain substantial far-field signal generated by depolarization of tissue remote from the recording electrode. In normal tissue the maximum negative slope is a good indication of local depolarization. In abnormal regions, such as infarct scars, the tissue beneath the recording electrode may be small relative to the surrounding myocardium outside the scar. A large far-field signal can obscure the small local potential.

Bipolar recordings are obtained by connecting two electrodes that are exploring the area of interest to the recording amplifier. At each point in time the potential generated is the sum of the potential from the positive input and the potential at the negative input. The potential at the

negative input is inverted, and thus subtracted from that at the positive input. Because the far-field signal is similar at each instant in time, it is largely subtracted out, leaving the local signal. In a homogeneous sheet of tissue, the initial peak of the bipolar signal coincides with depolarization beneath the recording electrode. The precision of locating the source of a particular electrical signal depends on the distance between the recording electrodes.

3.3 Cardiac mechanics

3.3.1 Lagrangian Green's strain tensor

The motion of the cardiac tissue when subjected to applied forces is commonly described by *continuum mechanics* using *strain tensors*. In continuum mechanics, the fact that the biological tissue consists of molecular and cellular substructures, thus has some sort of discontinuity, is conveniently ignored in the simplifying approximation that physical quantities, such as energy and momentum, can be handled in the infinitesimal limit. Therefore, differential equations can be employed in solving problems in continuum mechanics. *Tensors* are mathematical objects that are independent of coordinate system. However, tensors can be expressed in coordinate systems for computational convenience, as seen in the section 3.3.2.

The motion of a continuous and deformable solid can be described by a continuous displacement field resulting from a set of forces acting on the solid body. The initial unloaded state of the material is referred to as the *reference* or *undeformed* state because the displacements are zero. The material then reconfigures due to applied forces and reaches an equilibrium state referred to as the *deformed* state. The concept of *strain*, a measure of length change or displacement gradient, and *stress*, the force per unit area on an infinitesimally small plane surface within the material, are of fundamental importance for finite deformation theory (185).

Deformation is defined by the movement of *material points*, which can be thought of as small non-overlapping quantities of material that occupy unique points within the undeformed body. Each material point, \bar{X} , can be defined by a set of rectangular Cartesian coordinates, (X_1, X_2, X_3) , in the undeformed body. As the body deforms, the coordinate axes deform with it and so orthogonal coordinate axes in the undeformed state are no longer orthogonal in the deformed configuration. These coordinates are referred to as *Lagrangian coordinates* where a unique material point is always identified by the same coordinate values as the body deforms. Each point in space is defined by a set of *Eulerian coordinates* relative to a fixed reference Cartesian coordinate system. A particular spatial point, \bar{x} , with coordinates, (x_1, x_2, x_3) , may identify different material points as they pass through the point, \bar{x} , during the deformation. Conversely, a fixed material point, \bar{X} , may move to several spatial positions during the deformation. The Lagrangian coordinates, \bar{X} , may be chosen to coincide with the Eulerian coordinates, \bar{x} , in the undeformed state.

To quantify the deformation of a material, it is necessary to consider the change in length of *material segments*, or sets of adjacent material points within the body. In Figure 3-9, an infinitesimal material line segment, $d\bar{X}$, in the undeformed body B_0 has components (dX^1, dX^2, dX^3) with respect to global rectangular Cartesian coordinates (Y_1, Y_2, Y_3) . In the deformed body B the same material points that constituted $d\bar{X}$ have reconfigured, due to applied forces, into $d\bar{x}$, which has components (dx^1, dx^2, dx^3) with respect to (Y_1, Y_2, Y_3) . The deformation is quantified by the *deformation gradient tensor* \mathbf{F} , which carries the line segment, $d\bar{X}$, into $d\bar{x} = \mathbf{F} d\bar{X}$, or in component form, $dx^i = F^i_M dX^M$. The deformation gradients are defined in Eq. 3.1.

$$F_M^i = \frac{\partial x^i}{\partial X^M} \quad (3.1)$$

Any deformation can be divided into two processes: a rigid body rotation and a stretch. This *polar decomposition* can be represented mathematically by considering the deformation gradient tensor to be a product, $\mathbf{F} = \mathbf{R}\mathbf{U}$, of an orthogonal *rotation tensor* \mathbf{R} , and a symmetric positive definite *stretch tensor* \mathbf{U} . Therefore, the undeformed line segment components dX^M are stretched into $dy^L = U_M^L dX^M$ before being rotated into $dx^i = R_L^i dy^L$. The line segment could be rotated first and then stretched, but it is more convenient to interpret the stretch in terms of Lagrangian coordinates and then relate the stretched material lines to the Eulerian coordinates through the rotation tensor, \mathbf{R} . The stretch tensor, \mathbf{U} , contains a complete description of the material strain, independent of any rigid body motion.

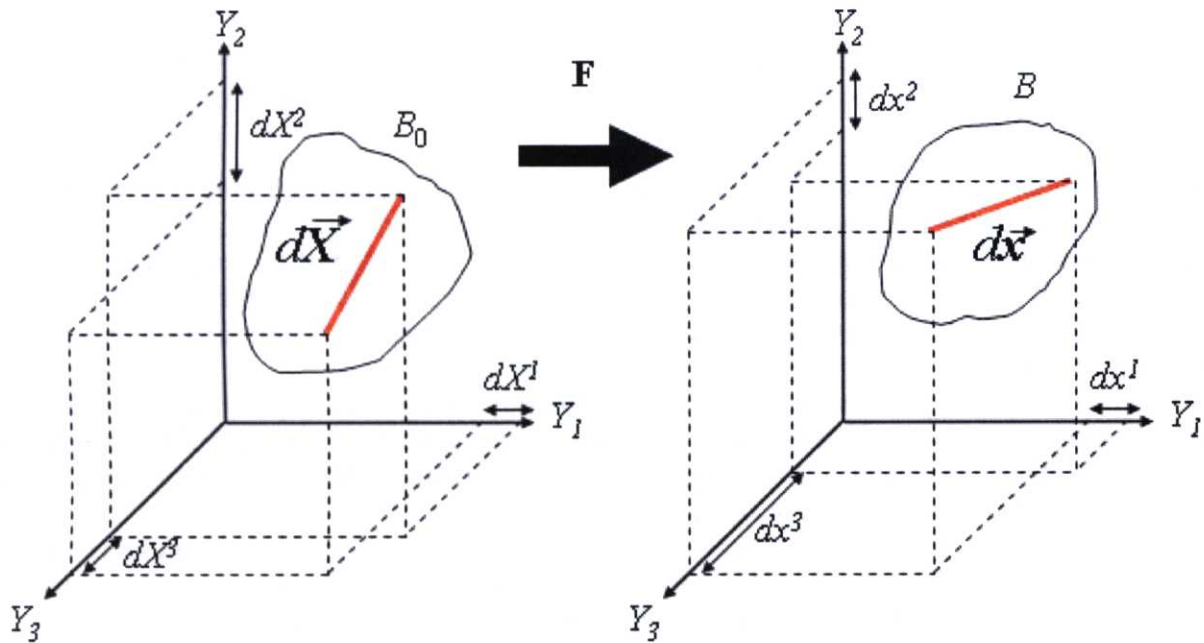


Figure 3-9. The deformation gradient tensor, \mathbf{F} , carries line segment $d\vec{X}$ into $d\vec{x}$.

Strain in a deforming body is determined by measuring segment length changes. Eq. 3.2 uses the Pythagorean theorem to determine the length of the deformed segment $d\vec{x}$.

$$ds^2 = dx^i dx^i = (d\vec{x})^T (d\vec{x}) = (\mathbf{F} d\vec{X})^T (\mathbf{F} d\vec{X}) = (d\vec{X})^T \mathbf{F}^T \mathbf{F} d\vec{X} = (d\vec{X})^T \mathbf{C} d\vec{X} \quad (3.2)$$

where

$$\mathbf{C} = \mathbf{F}^T \mathbf{F} = \left\{ \frac{\partial x_k}{\partial X_M} \frac{\partial x_k}{\partial X_N} \right\} \quad (3.3)$$

\mathbf{C} in Eq. 3.3 is termed *Green's deformation tensor* or the *right Cauchy-Green deformation tensor*, which indicates how each component of the undeformed line segment $d\vec{X}$ contributes to the

squared length of the deformed line segment $d\vec{x}$. The deformation tensor \mathbf{C} is related to the stretch tensor \mathbf{U} in Eq. 3.4 using the polar decomposition theorem,

$$\mathbf{C} = \mathbf{F}^T \mathbf{F} = (\mathbf{R}\mathbf{U})^T (\mathbf{R}\mathbf{U}) = \mathbf{U}^T \mathbf{R}^T \mathbf{R} \mathbf{U} = \mathbf{U}^T \mathbf{U} = \mathbf{U}^2 \quad (3.4)$$

because \mathbf{R} is orthogonal ($\mathbf{R}^T = \mathbf{R}^{-1}$) and \mathbf{U} is symmetric. \mathbf{C} is symmetric and positive definite like \mathbf{U} , therefore both \mathbf{U} and \mathbf{C} are expressed in terms of Lagrangian coordinates.

One method to calculate the stretch tensor \mathbf{U} from the deformation gradient tensor \mathbf{F} is to first calculate $\mathbf{C} = \mathbf{F}^T \mathbf{F}$, then calculate the eigenvalues $(\lambda_1)^2$, $(\lambda_2)^2$ and $(\lambda_3)^2$, and orthogonal eigenvectors \vec{s}_1 , \vec{s}_2 and \vec{s}_3 of \mathbf{C} using a similarity transformation. \mathbf{U} may then be constructed using Eq. 3.5.

$$\mathbf{C} = \mathbf{\Omega} \mathbf{\Lambda}^2 \mathbf{\Omega}^T = \mathbf{\Omega} \begin{pmatrix} (\lambda_1)^2 & 0 & 0 \\ 0 & (\lambda_2)^2 & 0 \\ 0 & 0 & (\lambda_3)^2 \end{pmatrix} \mathbf{\Omega}^T, \mathbf{U} = \mathbf{\Omega} \mathbf{\Lambda} \mathbf{\Omega}^T = \mathbf{\Omega} \begin{pmatrix} \lambda_1 & 0 & 0 \\ 0 & \lambda_2 & 0 \\ 0 & 0 & \lambda_3 \end{pmatrix} \mathbf{\Omega}^T \quad (3.5)$$

where the columns of $\mathbf{\Omega}$ are the orthonormal eigenvectors of \mathbf{C} and are the *principal axes of stretch*, and λ_i are the principal stretches (there is no shear when the deformation is referred to the principal axes). Because \mathbf{C} is a real symmetric matrix, the eigenvectors are orthogonal and therefore $\mathbf{\Omega}$ is an orthogonal matrix, ($\mathbf{\Omega}^T \mathbf{\Omega} = \mathbf{I}$). In essence, the similarity transformation diagonalizes \mathbf{C} and the positive square root of the resulting diagonal matrix is used to calculate the stretch tensor \mathbf{U} .

The two orthogonal tensors \mathbf{R} and $\mathbf{\Omega}$, derived from \mathbf{F} , have quite different physical interpretations. \mathbf{R} describes the rigid body rotation component of the deformation with no information about the material stretching, whereas the columns of $\mathbf{\Omega}$ are the orientations of the principal stretch axes *relative to the Lagrangian coordinates*.

In 3-D, the deformation tensor is a 3x3 matrix. There are three invariants (scalar combinations of the components of \mathbf{C}), which remain unchanged under coordinate rotations at a given state of deformation. These principal invariants are given in Eq. 3.6.

$$I_1 = \text{tr } \mathbf{C} \quad I_2 = \frac{1}{2} \{ (\text{tr } \mathbf{C})^2 - \text{tr } \mathbf{C}^2 \} \quad I_3 = \det \mathbf{C} \quad (3.6)$$

where the trace of \mathbf{C} , denoted by $\text{tr } \mathbf{C}$, is the sum of the diagonal terms, C_{MM} , and the determinant of \mathbf{C} , $\det \mathbf{C}$, is a measure of volume change.

The similarity transformation of Eq. 3.5 may be used to express the invariants of \mathbf{C} in terms of the principal stretch ratios as in Eq. 3.7.

$$\begin{aligned} I_1 &= (\lambda_1)^2 + (\lambda_2)^2 + (\lambda_3)^2 \\ I_2 &= (\lambda_1)^2 (\lambda_2)^2 + (\lambda_2)^2 (\lambda_3)^2 + (\lambda_3)^2 (\lambda_1)^2 \\ I_3 &= (\lambda_1)^2 (\lambda_2)^2 (\lambda_3)^2 \end{aligned} \quad (3.7)$$

Eq. 3.8 is the additional kinematic constraint that must be imposed on the deformation field for incompressible materials.

$$\det \mathbf{C} = I_3 = (\lambda_1 \lambda_2 \lambda_3)^2 = 1 \quad (3.8)$$

Eq. 3.9 shows how the *Lagrangian Green's strain tensor* \mathbf{E} , with respect to rectangular Cartesian coordinates, is related to the right Cauchy-Green deformation tensor \mathbf{C} .

$$\mathbf{E} = \frac{1}{2}(\mathbf{C} - \mathbf{I}) \quad (3.9)$$

3.3.2 Regional mechanics with transmural bead set

Waldman *et al.* developed a technique to apply continuum mechanics to evaluate cardiac mechanics (245). This technique measures 3-D myocardial deformation by tracking the 3-D displacements of three transmural columns of radiopaque beads placed within the LV free wall under thoracotomy (for technical details, see Chapter 6). The 3-D displacements of the beads, or material points, are calculated from the coordinates in two separate projection views using high-speed cineradiographic images (120-125 frames/second) (Figure 3-10, 3-11).

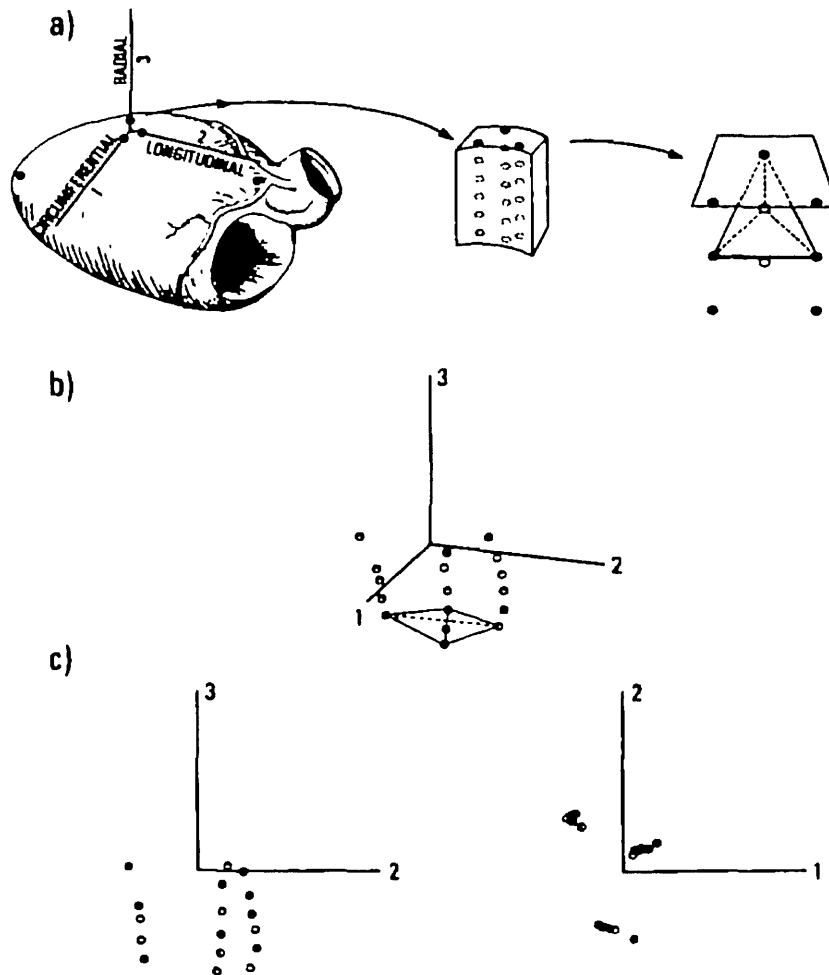


Figure 3-10. a) Five reference markers (apex bead, base bead and three epicardial beads) used to calculate a cardiac coordinate system, b) The 3-D coordinates of three columns of markers from in the reference coordinate system, c) Two projection views of the marker set to calculate the 3-D coordinates (245).

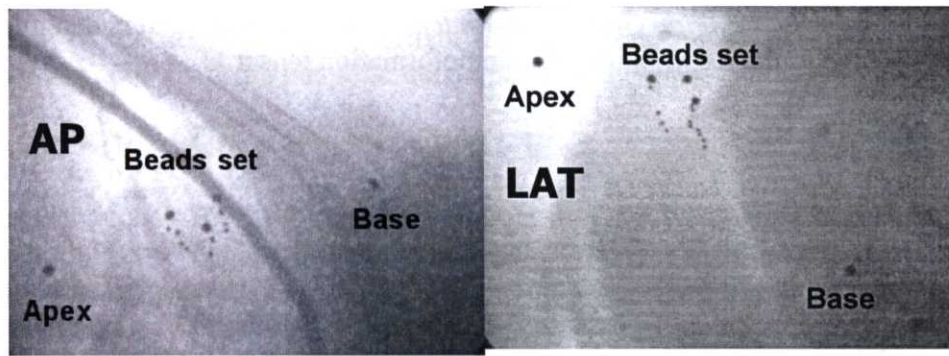


Figure 3-11. Two projection views of the high-speed cineradiographic images. AP, anteroposterior view; LAT, lateral view.

The setup includes five reference markers sutured to the epicardium: three directly above the three columns, one at the bifurcation of the left main coronary artery (base), and one at the apical dimple. These five reference markers define a local cardiac coordinate system: circumferential (X_1), longitudinal (X_2), and radial (X_3) axes of the LV wall (172). The positive radial direction (X_3) is orthogonal to the epicardial tangent plane defined by the three epicardial surface beads, and is directed from the endocardium to the epicardium. The positive longitudinal direction (X_2) is directed from the base bead to the apical bead, and the positive circumferential direction (X_1) is defined to be orthogonal to both the radial and the circumferential axes so that the circumferential, longitudinal and radial axes make a right-handed Cartesian coordinate system (Figure 3-12).

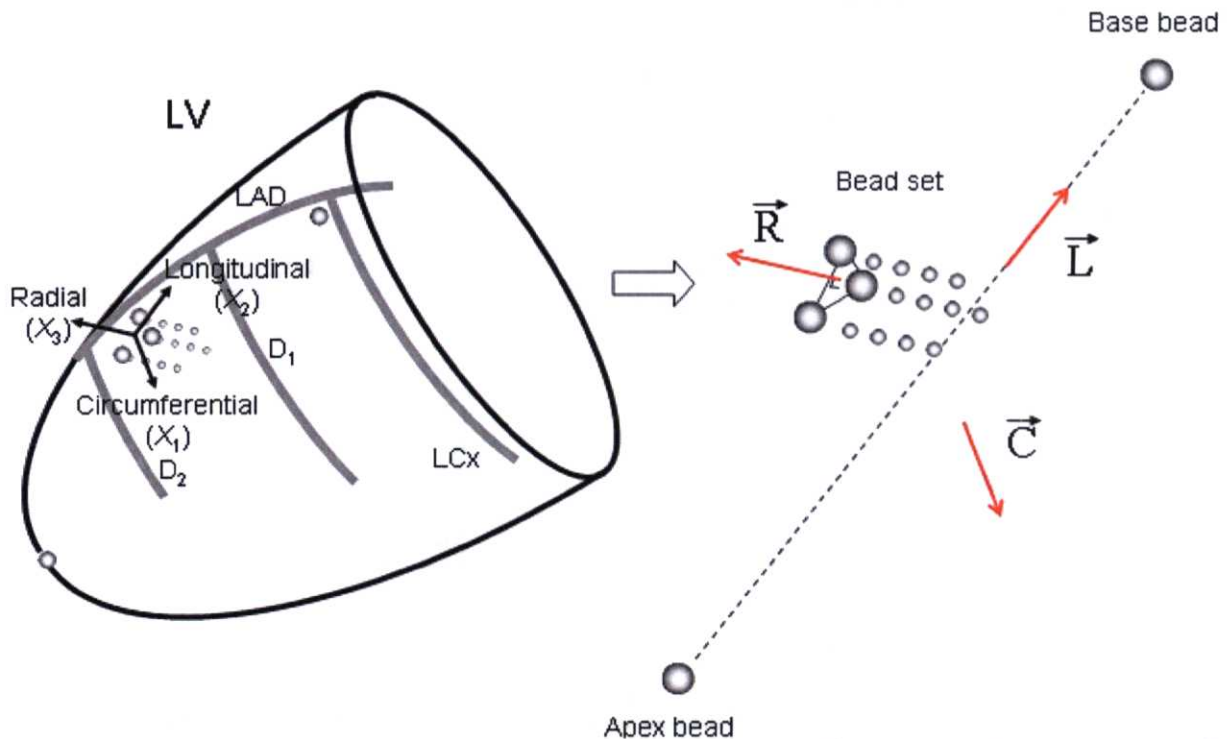


Figure 3-12. A local cardiac coordinate system defined by the transmural bead set. \vec{R} , radial axis; \vec{L} , longitudinal axis; \vec{C} , circumferential axis. When \vec{R} , \vec{L} , \vec{C} are unit vectors, $\vec{C} = \vec{L} \times \vec{R}$. LAD, left anterior descending coronary artery; LCx, left circumflex coronary artery; first (D_1) and second (D_2) diagonal branches of the LAD.

Differentiation of the deformed position with respect to the reference position provides the deformation gradient tensor \mathbf{F} , which depends on position. The Lagrangian Green's strain tensor \mathbf{E} (3x3 matrix) is then calculated at various values of reference wall depth. Thus, continuous, nonhomogeneous transmural distributions of 3-D finite strains are obtained. Six independent finite strains were computed in the local cardiac coordinate system. The three normal strain components reflect myocardial stretch or shortening along the circumferential (E_{11}), longitudinal (E_{22}), and radial (E_{33}) axes, and the three shear strains (E_{12} , E_{13} , and E_{23}) represent angle changes between pairs of the initially orthogonal coordinate axes. These six strain components can also be described as E_{cc} , E_{ll} , E_{rr} , E_{cl} , E_{cr} , E_{lr} to represent circumferential (c), longitudinal (l) and radial (r) axes (Eq. 3-10).

$$\mathbf{E}^{(\text{cardiac})} = \begin{pmatrix} E_{11} & E_{21} & E_{31} \\ E_{12} & E_{22} & E_{32} \\ E_{13} & E_{23} & E_{33} \end{pmatrix} = \begin{pmatrix} E_{cc} & E_{lc} & E_{rc} \\ E_{cl} & E_{ll} & E_{rl} \\ E_{cr} & E_{lr} & E_{rr} \end{pmatrix} \quad (3-10)$$

where $E_{12} = E_{21}$, $E_{13} = E_{31}$, $E_{23} = E_{32}$ ($E_{cl} = E_{lc}$, $E_{cr} = E_{rc}$, $E_{lr} = E_{rl}$) because $\mathbf{E}^{(\text{cardiac})}$ is an orthogonal matrix ($E_{ij} = E_{ji}$). This strain tensor is termed $\mathbf{E}^{(\text{cardiac})}$ because it contains the strain components along the local cardiac coordinate axes (66).

To relate the finite strains to the local 3-D microstructures of the LV wall, a local fiber-sheet coordinate system (X_f , X_s , X_n) can be constructed which defines the muscle fiber axis (X_f), the sheet axis (X_s) that lies within the sheet plane and is perpendicular to X_f , and the orthogonal X_n axis oriented normal to the sheet plane (Figure 3-13) (65). With the values of fiber (α) and sheet angles (β) at all depths, the strain tensor $\mathbf{E}^{(\text{cardiac})}$ can be converted from the cardiac coordinate system to the fiber-sheet coordinate system using an orthogonal transformation to obtain the strain tensor $\mathbf{E}^{(\text{fiber-sheet})}$ that contains the strain components along the local fiber-sheet coordinate axes (Eq. 3-11).

$$\mathbf{E}^{(\text{fiber-sheet})} = \mathbf{M} \mathbf{E}^{(\text{cardiac})} \mathbf{M}^T = \begin{pmatrix} E_{ff} & E_{sf} & E_{nf} \\ E_{fs} & E_{ss} & E_{ns} \\ E_{fn} & E_{sn} & E_{nn} \end{pmatrix} \quad (3-11)$$

where

$$\mathbf{M} = \begin{pmatrix} \cos \alpha & \sin \alpha & 0 \\ -\sin \alpha \sin \beta & \cos \alpha \sin \beta & \cos \beta \\ \sin \alpha \cos \beta & -\cos \alpha \cos \beta & \sin \beta \end{pmatrix}$$

and $E_{fs} = E_{sf}$, $E_{fn} = E_{nf}$, $E_{sn} = E_{ns}$ because $\mathbf{E}^{(\text{fiber-sheet})}$ is an orthogonal matrix ($E_{ij} = E_{ji}$) (66). The relationship between the local cardiac coordinate axes and the local fiber-sheet coordinate axes is schematically described in Figure 3-13A. Fiber angle (α) is measured in the circumferential-longitudinal plane (X_1 - X_2) at each transmural depth between the positive fiber axis (X_f) and the positive circumferential axis (X_1), with a positive angle defined as rotation toward the longitudinal axis (X_2) (Figure 3-13B). Sheet angle (β) is measured in the radial-cross-fiber plane (X_3 - X_{cf}) with reference to the radial axis (X_3), with a positive angle defined as rotation towards the positive cross-fiber axis (X_{cf}) (Figure 3-13C). The fiber axis (X_f), the cross-fiber axis (X_{cf}) and

the radial axis (X_3) compose a right Cartesian system. Similarly, the fiber axis (X_f), the sheet axis (X_s) and the normal axis (X_n) oriented normal to the sheet plane (X_f - X_s) also present a right Cartesian system.

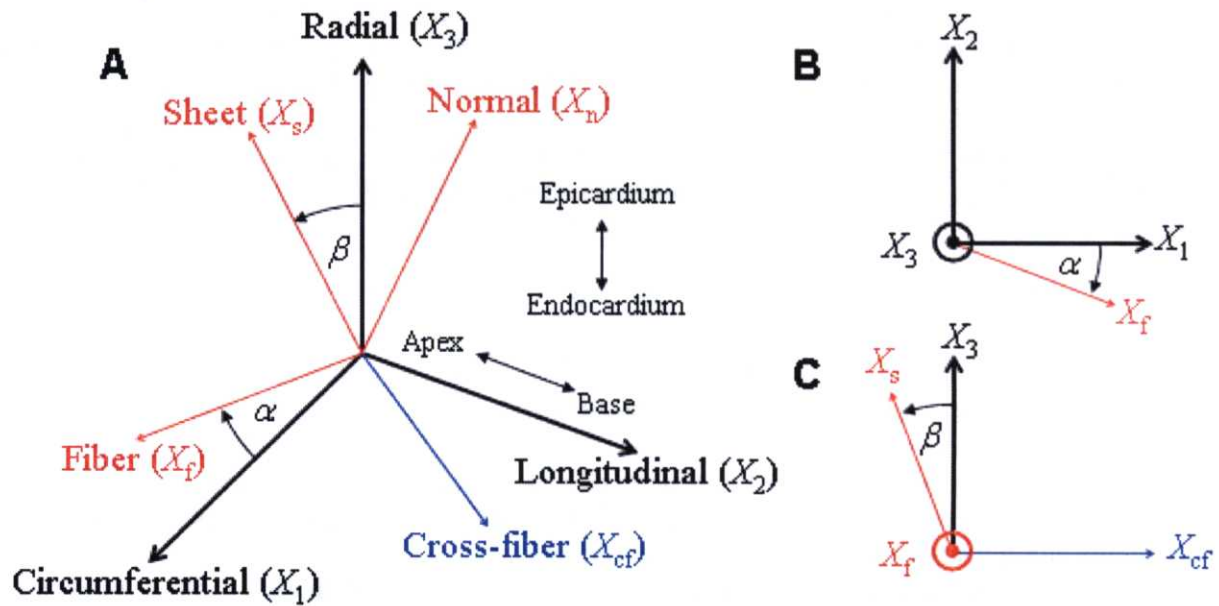


Figure 3-13. Relationship between the local cardiac coordinate axes (X_1 , X_2 , X_3) and the local fiber-sheet coordinate axes (X_s , X_f , X_n). In B, the radial axis (X_3) points out of the paper. In C, the fiber axis (X_f) points out of the paper. α , fiber angle; β , sheet angle.

This transmural model of fiber-sheet structure contains important structural assumptions. The myocardial fibers are assumed to run parallel to the epicardial plane, and this assumption is generally valid at the basal and mid-ventricular level. However, the angle between the true fiber direction and the epicardial tangent plane, called imbrication angle, becomes large toward the apical region and thus can be a source of error in strain estimation. In addition, the dispersion of fiber angles at each layer is ignored and usually the average fiber angle is used for the calculation. The dispersion of sheet angles is also ignored, and usually the average sheet angle is used for the calculation. This can be a source of error in strain estimation when there are multiple sheet populations within the same layer (12, 17)

$E^{(\text{fiber-sheet})}$ contains another set of six finite strains (fiber-sheet strains): the three normal strains represent stretch or shortening along the fiber direction (E_{ff}), along the sheet direction (E_{ss}), and normal to the fiber-sheet plane (E_{nn}), whereas the three shear strains measure shear within the sheet plane (E_{fs}) and shear that results from sliding of adjacent sheets parallel to the fiber direction (E_{fn}) or transverse to the fiber axis (E_{sn}).

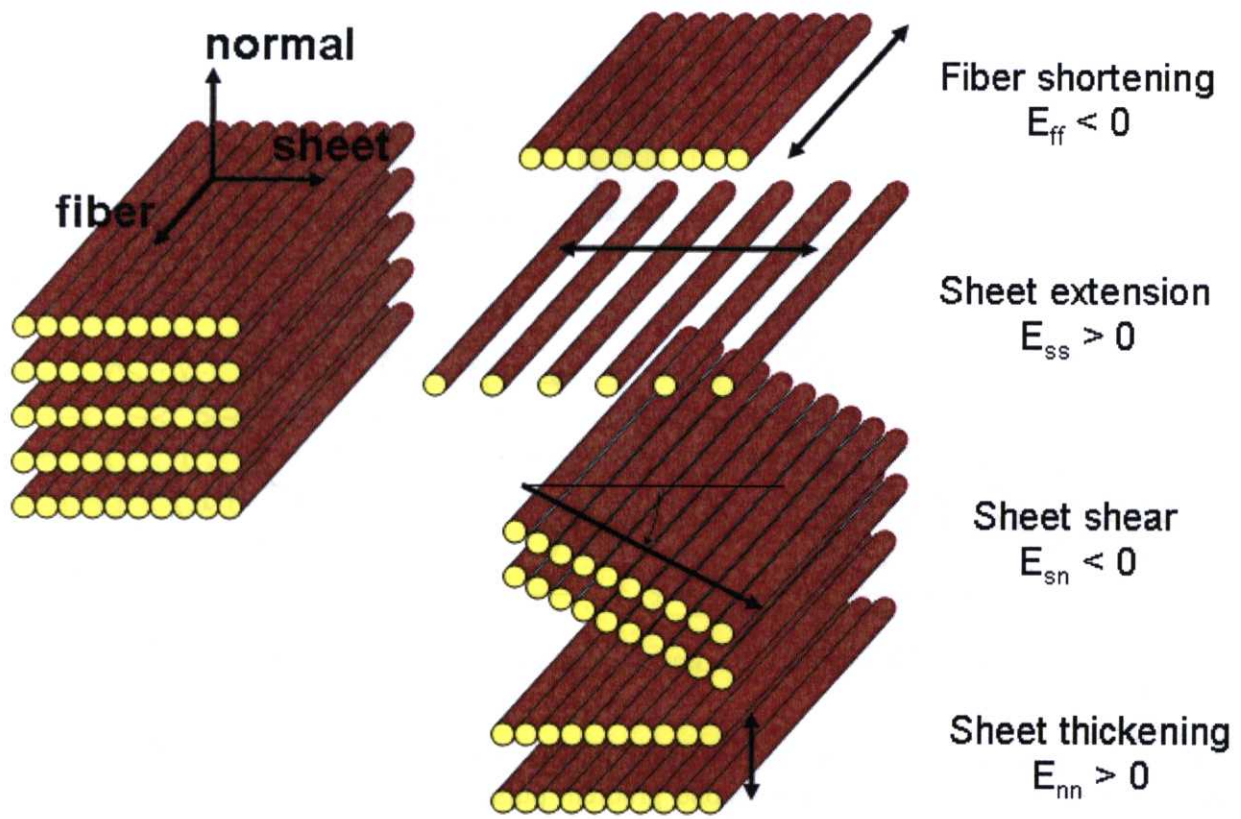


Figure 3-14. A local fiber-sheet coordinate system and its major strain components.

3.3.3 Global mechanics with MRI

The principles of magnetic resonance imaging (MRI) can be found in excellent textbooks and reviews (106, 178, 189), which form a basis of this section. In essence, MRI can noninvasively detect signals from hydrogen atoms (H). Because more than 90% of hydrogen atoms in human body consist of water (H₂O), the MRI signals are dominated by water in biomedical imaging. MRI is sensitive to motion, and thus provides the data from which mechanics of the heart during contraction can be described (24). A pair of pulsed field gradients (PFG) is a commonly used technique that is applied to phase-contrast velocity encoding, diffusion weighted imaging and displacement encoding (194). This section focuses on PFG-based displacement encoding from which Lagrangian Green's strain tensors can be calculated.

In PFG schemes, a gradient pulse with a strength of G and a duration of δ (Figure 3-14) is applied to introduce the phase shift $\phi(x)$ with respect to an arbitrarily defined reference point ($x = 0$) (Eq. 3-12),

$$\phi(x) = \gamma G \delta x \quad (3-12)$$

where γ is the gyromagnetic ratio for the spin ($2.765 \times 10^8/\text{s, T}$), which relates its resonance frequency to the strength of the local magnetic field, and x is the location of the sample along the x axis. Thus, the initial location of the sample is encoded in the phase information by the gradient pulse, which is termed a dephasing gradient.

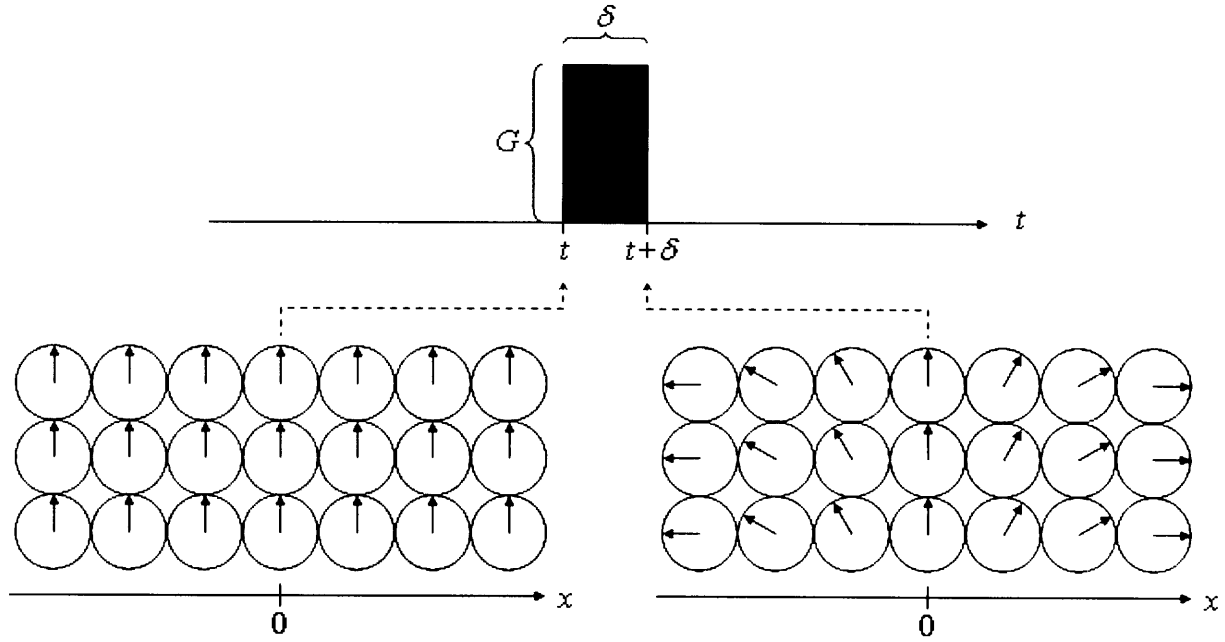


Figure 3-15. Encoding of the initial location by the a gradient pulse. A circle and an arrow represent a sample and its phase at each time point, respectively.

After a time period Δ , during which the tissue moves along the x axis from the initial location $x(t)$ to a new location $x(t + \Delta)$, the second gradient pulse of the same size, but of the opposite direction ($-G$), is applied (Figure 3-15). The second gradient pulse is often called a rephrasing gradient, which confers each sample a phase shift \mathcal{G} that is proportional to the displacement $x(t + \Delta) - x(t)$ of the complex-valued sample at each image pixel (Eq. 3.13).

$$\mathcal{G} = \gamma G \delta \{x(t + \Delta) - x(t)\} \quad (3.13)$$

The precision of the motion measurement based on PFG methods is determined by the area of the pulsed gradients ($= G\delta$), and is independent of the spatial resolution of the image. However, the measured value represents a superposition of all the signals from the whole voxel, therefore is an average of the motion over the whole voxel. In addition, dispersive motions in a given voxel, including diffusion, shear, compression, and rotations, can cause signal attenuation due to destructive interference caused by the reduction in phase coherence (223). Moreover, potential aliasing of the phase information must be evaluated either by restricting the range of phase evolution to $-\pi < \mathcal{G} < \pi$, or by obtaining additional measurements to assist in resolving the ambiguity (194). In general, a single displacement-encoded sample does not provide sufficient information to recover the actual displacements due to the presence of additional sources of phase in the MRI signal, including B_0 inhomogeneity and RF coil phase. These effects can largely be canceled though the use of reference scans and phase cycling schemes.

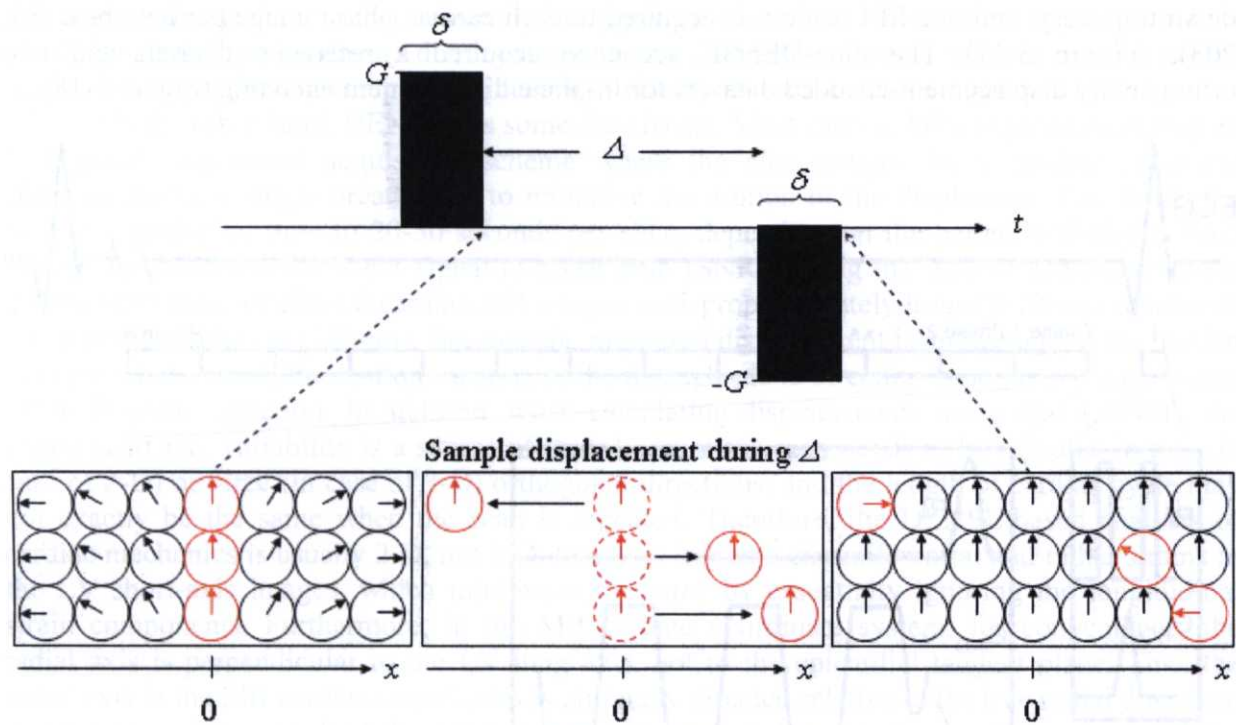


Figure 3-16. A pair of dephasing (G) and rephasing ($-G$) gradient pulses to encode the displacement of each sample from the initial location.

The bipolar encoding sequence shown in Figure 3-15 is not optimal to track cardiac motion because the signal decays rapidly with T_2^* and suffers phase distortions due to local B_0 inhomogeneities. A family of recently developed, highly sensitive motion-encoding schemes, called DENSE (=Displacement ENcoding of Stimulated Echoes) (3-5), employs an ECG-gated pulsed gradient stimulated echo (PGSTE) sequence (50) to reduce attenuation to T_1 by storing one component of the magnetization along M_z and to allow motion-encoding periods ($=\Delta$) sufficiently long for cardiac motion (Figure 3-16).

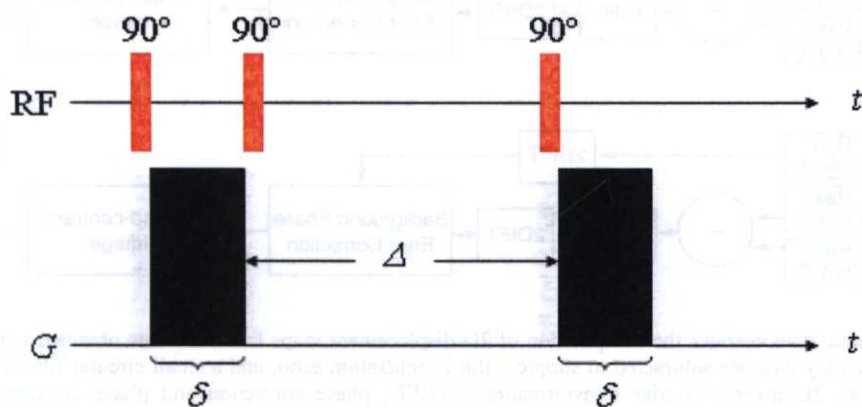


Figure 3-17. Pulsed gradient stimulated echo (PGSTE) sequence, which stores one component of the magnetization along longitudinal magnetization.

A derivative of DENSE, known as cine-DENSE, acquires two-dimensional (2D) displacement-encoded images at multiple phases of the cardiac cycle (137). The cine-DENSE sequence employs a gradient-echo type three-echo flyback echo-planer imaging (EPI) readout with a top-

down trajectory, and one EPI readout is acquired to each cardiac phase image per heartbeat (83, 203). (Figure 3-17). The cine-DENSE sequence acquired a reference dataset, and two orthogonally displacement-encoded datasets for in-plane displacement encoding (Figure 3-18).

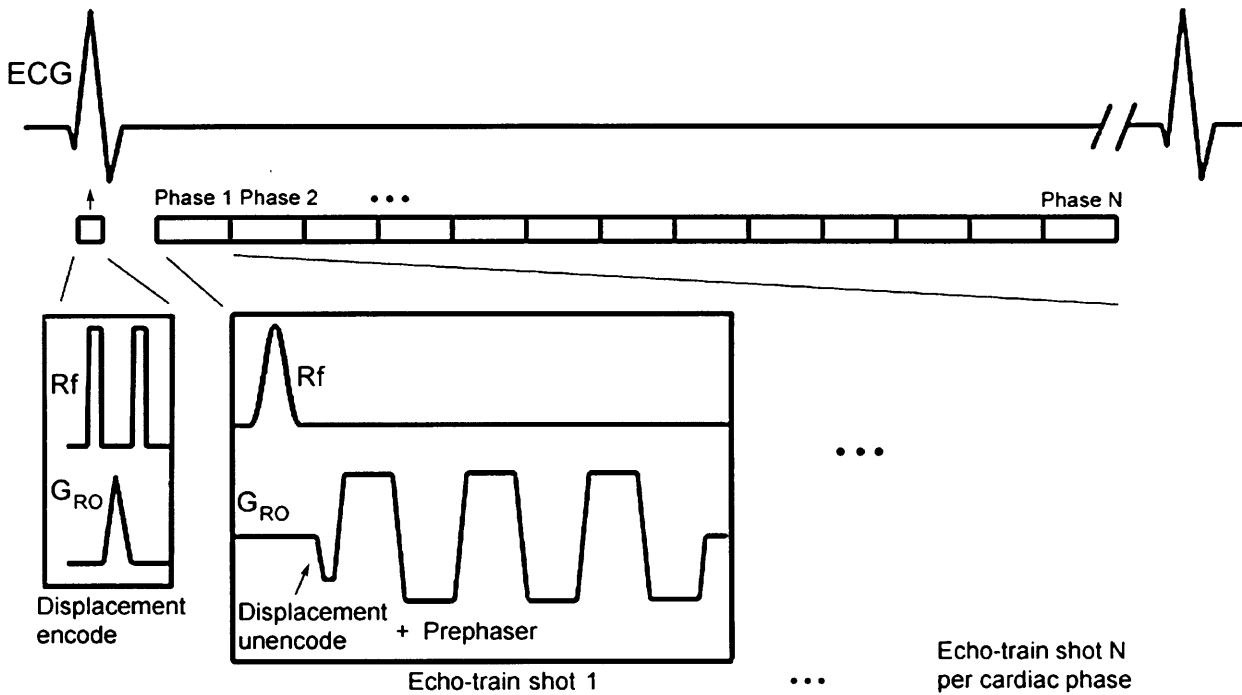


Figure 3-18. Pulse sequence diagram for cine-DENSE. Following an ECG trigger, the dephasing gradient pulse is emitted to encode displacement. A segmented fast gradient-echo echo-planar imaging sequence modified to include the DENSE unencoding (= rephrasing) gradient is used to rapidly sample the displacement-encoded longitudinal magnetization at multiple cardiac phases. G_{RO} = readout gradient, Rf = radiofrequency (137).

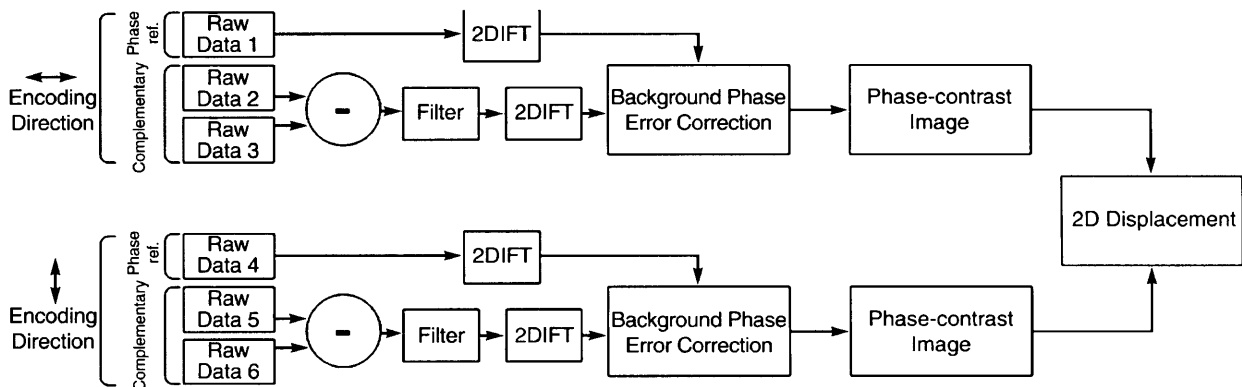


Figure 3-19. Schematic demonstrates the computation of 2D displacement maps from raw data obtained with cine DENSE MR imaging. Complementary data are subtracted to suppress the T_1 relaxation echo, and a small circular filter is applied to remove residual signal. After 2D inverse Fourier transformation (2DIFT), phase correction and phase unwrapping are performed, followed by computation of one-dimensional displacement values. Vector addition of orthogonal one-dimensional displacement values yields a 2D displacement map. *Phase ref.* = phase reference (137).

The DENSE-based analysis of cardiac mechanics has three major advantages over other techniques. First, the site of measurement of myocardial strains is not limited by implantation of physical materials. Therefore, strains can be calculated virtually anywhere in the heart. Second, it

is a noninvasive technique that can easily be applied to human patients. Third, while it achieves pixelwise spatial resolution and direct extraction of displacement data, it requires much less user input for post-processing compared with earlier techniques such as tissue tagging (25, 264).

On the other hand, DENSE has some drawbacks. Most cardiac MRI sequences employ an ECG-gated, segmented acquisition scheme where the cine images for a cardiac cycle are acquired during a single breath hold to minimize the motion of the diaphragm. This limits the realistic acquisition time to 20-30 seconds per slice, depending on the patient's ability to hold breath. To achieve a sufficient signal-to-noise ratio (SNR) during the limited acquisition time, the slice thickness of clinical cardiac MR images is disproportionately large (8-10mm) relative to the in-plane resolution (1-2mm). Because the measured displacement is an average of the motion over the whole voxel, the motion tracking in the through-plane direction is not as accurate as that of the in-plane direction. In addition, when calculating displacements using cine-DENSE, the innate heart rate variability is a source of error because the scan needs to be repeated in two (in case of 2-D) or three (in case of 3-D) orthogonal directions, and the length of cardiac cycle may not exactly be the same when the scan is repeated. Therefore, the DENSE-based analysis of cardiac mechanics is usually 2-D, not 3-D, to assess in-plane circumferential and radial strains in the LV short-axis images, which minimizes the error by essentially ignoring the longitudinal strain components. Furthermore, in the MR cardiac coordinate system, for convenience, the radial axis is perpendicular to the LV long axis, not to the epicardial tangent plane. Thus the radial axis in the MR cardiac coordinates is obliquely directed relative to the true radial direction, and the angle between the MR radial axis and the true radial axis becomes larger toward the apical region. This makes it difficult to compare values the radial strains between the MR-based technique and the conventional techniques such as the transmural bead set.

Chapter 4

Regional mechanics during relaxation in normal heart

4.1 Abstract

Early relaxation in the cardiac cycle is characterized by rapid torsional recoil of the LV wall. To elucidate the contribution of the transmural arrangement of the myofiber to relaxation, the time course of 3-D fiber-sheet strains was determined in the anterior wall of 5 adult mongrel dogs *in vivo* during early relaxation, using biplane cineangiography (125Hz) of implanted transmural markers. Fiber-sheet strains were found from transmural fiber and sheet orientations directly measured in the heart tissue. Strain time course was determined during early relaxation in the epicardial, mid, and endocardial layers, referenced to the end-diastolic configuration. During early relaxation, significant circumferential stretch, wall thinning, in-plane and transverse shear were observed ($P < 0.05$). Significant stretch along myofibers in the epicardial layers, and sheet shortening and shear in the endocardial layers were also observed ($P < 0.01$). Importantly, predominant epicardial stretch along the fiber direction and endocardial sheet shortening occurred during isovolumic relaxation ($P < 0.05$). In conclusion, LV mechanics during early relaxation involves substantial deformation of fiber and sheet structures with significant transmural heterogeneity. Predominant epicardial stretch along myofibers during isovolumic relaxation appears to drive global torsional recoil to aid early diastolic filling.

4.2 Introduction

The LV myocardium is composed of intricately woven structures of myofibers which run parallel to the epicardial tangent plane (188, 225), and are arranged in radially oriented laminae or sheets (150). The principal fiber orientation presents a gradual counterclockwise rotation from the epicardium to the endocardium, resulting in a local helical architecture of myofibers with a transmural angle gradient spanning $\sim 120^\circ$. The helical architecture of the LV myofibers is the mechanistic basis of global LV torsion, or twisting about the LV long axis (41, 121, 122), which facilitates homogeneous distribution of systolic shortening of the myofibers across the LV wall (14, 33). The laminar or sheet structure of the myocardium consists of a layered arrangement of branching myofiber bundles approximately four cells thick with extensive cleavage planes between the layers (150, 192). The myocardial sheet architecture exhibits a transmural and regional variation, and the sheet angles undergo a dynamic change during the cardiac cycle (230), whereas the muscle fiber angles do not (225). Sheet extension, thinning and shear appear to be part of the mechanistic basis of systolic LV wall thickening, which contributes to minimizing end-systolic volume, thus maximizing stroke volume (66). The myocardial fiber and sheet structures therefore play an important role in LV contraction, however, the mechanistic significance of these structures during LV relaxation remains unknown.

Early relaxation in the cardiac cycle is a critical period for LV untwisting or torsional recoil, which releases energy stored during systole, likely contributing to ventricular suction during early filling (32, 33, 202, 226, 260). Torsional recoil is impaired in myocardial infarction (184), tachycardia-induced cardiomyopathy (32, 232), and aortic stenosis (226), suggesting its importance in normal cardiac function.

In the present study, it was reasoned that the structure(s) contributing to recoil (e.g., myofibers) would demonstrate the earliest and most prominent return to diastolic configuration during early relaxation. To investigate the contribution of the fiber and sheet structures to LV mechanics during early relaxation, 3-D finite deformation in the LV anterior wall was determined during early relaxation in normal dog hearts *in vivo*. The strain analysis indicated complex fiber and sheet mechanics with transmural heterogeneity during early relaxation, represented by myofiber stretch in the epicardial layers, which confirms modeling predictions of

a predominant role of epicardial fibers, and sheet shortening transverse to the fibers in the endocardial layers, all of which may aid early diastolic filling.

4.3 Materials and Methods

All animal studies were performed according to the National Institutes of Health guidelines for the care and use of laboratory animals in research. All protocols were approved by the Animal Subjects Committee of the University of California, San Diego, which is accredited by the American Association for Accreditation of Laboratory Animal Care.

4.3.1 Surgical preparation

Five adult mongrel dogs (19-28 kg) were anesthetized with intravenous thiopental (8-10 mg/kg), intubated, mechanically ventilated with isoflurane (0.5-2.5%), nitrous oxide (3L/min) and medical oxygen (3L/min) to maintain a surgical plane of anesthesia. A median sternotomy was performed to expose the heart, which was placed in a pericardial cradle. The surface electrocardiogram (ECG) was recorded throughout the study. An 8 Fr pigtail micromanometer catheter (Millar Instruments, Houston, TX) was inserted through a 9 Fr arterial introducer placed in the left femoral artery, and the catheter tip was advanced into the LV. LV pressure was monitored with the pigtail micromanometer catheter, and the pressure was matched with that recorded from the sideholes of the same catheter that was connected to a fluid-filled transducer. Central aortic pressure was monitored through another 8 Fr fluid-filled catheter placed in the left brachiocephalic artery.

To measure 3D myocardial deformation in each heart, three transmural columns of four to six 0.8-mm-diameter gold beads were placed within the anterior wall between the first (D_1) and the second diagonal branches (D_2) of the left anterior descending (LAD) coronary artery (Figure 4-1A), using techniques described previously (245). Briefly, an 8-mm-thick Plexiglas template, with three holes drilled at the corners of a 10-mm equilateral triangle to act as guides for the bead insertion trocar, was sutured to the epicardium. After the bead insertion was complete, the platform was removed, and a 1.7-mm-diameter surface gold bead was sewn onto the epicardium above each column. Gold beads (2-mm diameter) were sutured to the apical dimple (apical bead, Figure 4-1A) and on the epicardium at the bifurcation of the left anterior descending and left circumflex coronary arteries (base bead, Figure 4-1A) to provide end-points for a LV long axis. The local epicardial tangent plane defined by the three epicardial surface gold beads and the LV long axis were used to define a local cardiac coordinate system aligned with the circumferential, longitudinal and radial axes of the LV wall (172). A pair of pacing wires was sutured to the left atrial appendage (LAA, Figure 4-1A).

4.3.2 Experimental protocol

Atrial pacing was performed by stimulating both atrial electrodes (Figure 4-1A) via a square-wave, constant-voltage electronic stimulator at a frequency 20% above baseline heart rate to suppress native sinus rhythm. Stimulation parameters (voltage 10% above threshold, duration 8 ms, and frequency) were kept constant in each animal. The animal was positioned in a biplane radiography system, with image planes adjusted such that all the bead markers were visible in both the anteroposterior (AP) and the lateral (LAT) views.

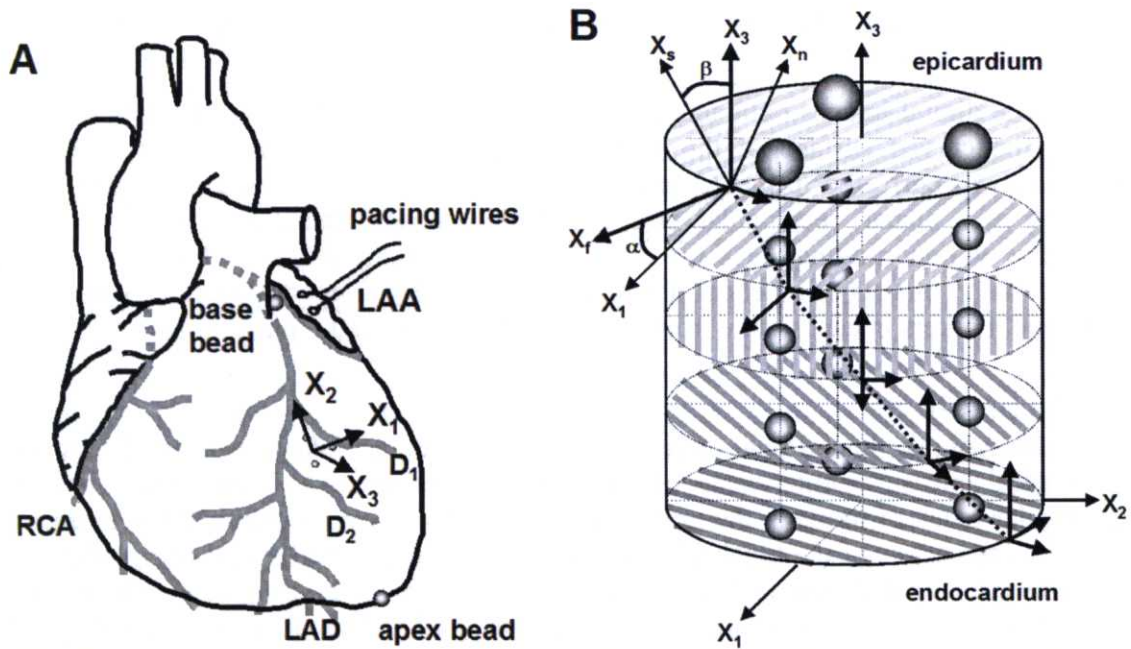


Figure 4-1. Sites of marker implantation. A: Schematic representation of the heart. X_1 : circumferential axis, X_2 : longitudinal axis, X_3 : radial axis, LAA: left atrial appendage, RCA: right coronary artery, LAD: left anterior descending, D₁, D₂: first and second diagonal branch of LAD, respectively. B: Schematic representation of excised tissue block containing the bead set. Fiber angle (α) was measured in the circumferential-longitudinal (X_1 - X_2) plane at each transmural depth with reference to the positive circumferential axis (X_1), with a positive angle defined as rotation towards the longitudinal axis (X_2). Sheet angle (β) was measured in the plane perpendicular to the fiber angle at each transmural depth with reference to the radial axis (X_3), with a positive angle defined as rotation towards the positive crossfiber direction (X_{cf}). X_f : fiber axis, X_s : sheet axis, X_n : axis oriented normal to the sheet plane. The X_f , X_s , and X_n axes present a right Cartesian system.

The image acquisition system for dual digital camera operation was based on two MegaPlus™ ES310/T cameras (Redlake, San Diego, CA) controlled by custom software (Forster System Engineering, Irvine, CA). With mechanical ventilation suspended at end expiration, synchronous biplane cineradiographic images of the bead markers were digitally acquired at 125 frames/sec for a total of four seconds with simultaneous recording of ECG, LV pressure and camera shutter markers for subsequent correlation of cine images with physiological events. At the end of the study, snares were placed around the lung hila, and the inflow and outflow vessels of the heart. A 22-26 Fr cannula with side holes was inserted into the ascending aorta through a brachiocephalic artery. An overdose of pentobarbital sodium was administered, and the heart was brought to arrest by tightening the ligatures around the inflow vessels. The aortic cannula was perfused with normal saline at 100 ~ 110 mmHg which closed the aortic valve and perfused the coronary arteries. After coronary flow was established, the LV pressure was adjusted to the end-diastolic pressure observed in the study by injection of normal saline into the LV cavity, the right ventricle was vented, and the heart fixed by switching the aortic cannula perfusate to buffered glutaraldehyde (2.5%) (257). Because the heart was fixed at end-diastolic pressure, fiber and sheet orientations in the fixed hearts were assumed to represent the fiber-sheet structure in the end-diastolic reference configuration (66). The heart was excised and stored in 2.5% buffered glutaraldehyde for 24 hr, then transferred to 10% buffered formalin for 24-48 hr.

4.3.3 Spherical correction and 3-D reconstruction of cineradiographic images

The digital images obtained from the biplane X-ray intensifiers are spherically distorted due to the curved surface of the image intensifiers and the camera lenses. This spherical distortion was corrected in the AP and LAT views separately, using cubic interpolation of the mapping of a planar, rectangular grid of reference beads attached to the front of the image intensifier without moving the X-ray tubes and image intensifiers from their positions during the study. Finally, images of a helical phantom were recorded to reconstruct the 3-D coordinates of gold bead markers in each frame from the spherically corrected biplane images (158).

4.3.4 Histology

To avoid the distortional effects of dehydration and shrinkage associated with embedding, histological measurements were obtained using freshly fixed heart tissue. A transmural rectangular block of tissue in the implanted bead set was carefully removed from the ventricular wall, with the edges of the block cut parallel to the local circumferential, longitudinal and radial axes of the LV as determined from the same epicardial markers used for the strain analysis. The transmural thickness of the block was measured, and the block was sliced into 1-mm-thick sections parallel to the epicardial tangent plane, forming a series from the epicardium to the endocardium to measure the fiber angles across the LV wall. Fiber angle (α) was determined under a dissection microscope with reference to the positive circumferential axis (α , Figure 4-1B). Mean fiber angle was calculated at each transmural depth as described previously (66). Each 1-mm-slice tissue was then embedded with Tissue-Tek[®] O.C.T. compound (Sakura Finetek USA, Inc. Torrance, CA) and quickly frozen in a 2-methybutane bath cooled with dry ice. Multiple serial thin sections (5 μ m) perpendicular to the mean fiber direction were made from each slice tissue, transferred to a glass slide, and allowed to desiccate for 10 min. Digital images of the tissue section were acquired at low-power magnification (x 20), using a digital camera (Coolpix 990, Nikon, Melville, NY) mounted on a light microscope (Optiphot-2, Nikon, Melville, NY). The images were transferred to a Windows-based computer with image processing software (Image J version 1.30g, NIH). Myocardial laminae, or sheets, were directly visible with no further enhancement of the digital montage. Sheet angle (β) was measured with reference to the positive radial axis (Figure 4-1B, β), as reported previously (66). Angle measurements were made for all visible cleavage planes in 3-9 sections to achieve 100 ~ 300 measurements per slice tissue, and mean sheet angle (β) was calculated in each 1-mm slice tissue. This process was repeated from the epicardial slice to the endocardial slice to yield transmural distribution of mean sheet angles.

4.3.5 Strain analysis

The 3-D coordinates of the implanted markers were obtained as described above for an entire cardiac cycle selected for each animal. In principle, continuous, nonhomogeneous transmural distributions of 3-D finite strains were calculated using an approach developed by Waldman *et al.* (245), later by McCulloch *et al.* (166) and most recently by Costa *et al.* (66). However, many of the fitting algorithms used in this study have been revised and the software rewritten for a Windows-based system. Briefly, a continuous polynomial position field that mapped the beads in the undeformed reference configuration to those in the deformed configuration was determined. In essence, the deformed position of a bead was approximated by a polynomial function of its reference position. The degrees of freedom in the polynomial position field were optimized to give the best fit of the measured bead positions relative to the

approximated or fit bead positions. The order of the polynomial is at most linear in circumferential and apex-base, and the maximum order in radius is typically quadratic. To eliminate oscillations in the fitting polynomial, the number of degrees of freedom was kept much smaller than the number of measurements, typically 10-fold fewer. With this continuous polynomial mapping from reference position to current position, differentiation with respect to reference position gives the deformation gradient tensor, \mathbf{F} , which depends on position. Then the Lagrangian Green's strain tensor was calculated as $0.5(\mathbf{F}^T\mathbf{F}-\mathbf{I})$ at various values of reference wall depth.

Six independent finite strains were computed in the cardiac coordinate system (X_1, X_2, X_3) (172). The three normal strain components reflect myocardial stretch or shortening along the circumferential (E_{11}), longitudinal (E_{22}), and radial (E_{33}) cardiac axes, and the three shear strains (E_{12} , E_{13} , and E_{23}) represent angle changes between pairs of the initially orthogonal coordinate axes. To relate the finite strains to the local 3-D structure of the LV wall, a local fiber-sheet coordinate system (X_f, X_s, X_n) was constructed in each heart, which defines the muscle fiber axis (X_f), the sheet axis (X_s) that lies within the sheet plane and is perpendicular to X_f , and the orthogonal X_n axis oriented normal to the sheet plane (65). With the values of the fiber (α) and sheet angles (β) at all depths, an orthogonal transformation was performed to convert the strain tensor from the cardiac coordinate system to the fiber-sheet coordinate system (65). This yields another set of six finite strains ("fiber-sheet strains"): the three normal strains represent stretch or shortening along the fiber direction (E_{ff}), sheet direction (E_{ss}) and normal to the fiber-sheet plane (E_{nn}), whereas three shear strains measure shear within the sheet plane (E_{fs}), shear that results from sliding of adjacent sheets parallel to the fiber direction (E_{fn}), or transverse to the fiber axis (E_{sn}) (230).

Transmural finite strains were calculated for each frame (125 frames/sec) during early relaxation as a deformed configuration, with end-diastole (defined at the time of the peak of the ECG R-wave) as the reference state. The pressure at the nadir of the dicrotic notch of the central aortic pressure was used to estimate the time of end-systole from the micromanometer tracing. Early relaxation was defined as the period beginning at end-systole (time = 0 %) and ending at minimum LV pressure (time = 100%, Figure 4-2) (130). The strain data in each animal during the early relaxation period were linearly interpolated to determine finite strains at 10% increments in time. The strain time course was determined at three wall depths: 25% (epicardium), 50% (midwall) and 75% (endocardium) wall depth from the epicardial surface. Fiber-sheet strains deeper than 75% were not determined because of the presence of two separate populations of sheets in the inner 20% of the wall (See Results).

4.3.6 Statistical analysis

Values are means \pm SE unless otherwise specified. The effects of wall depth and time on each strain component were determined by two-factor repeated measures ANOVA. The Student-Newman-Keuls method was used for ANOVA post-hoc analysis. Statistical tests were performed using SigmaStat 3.0 (SPSS, Inc. Chicago, IL). Statistical significance was accepted at $P < 0.05$.

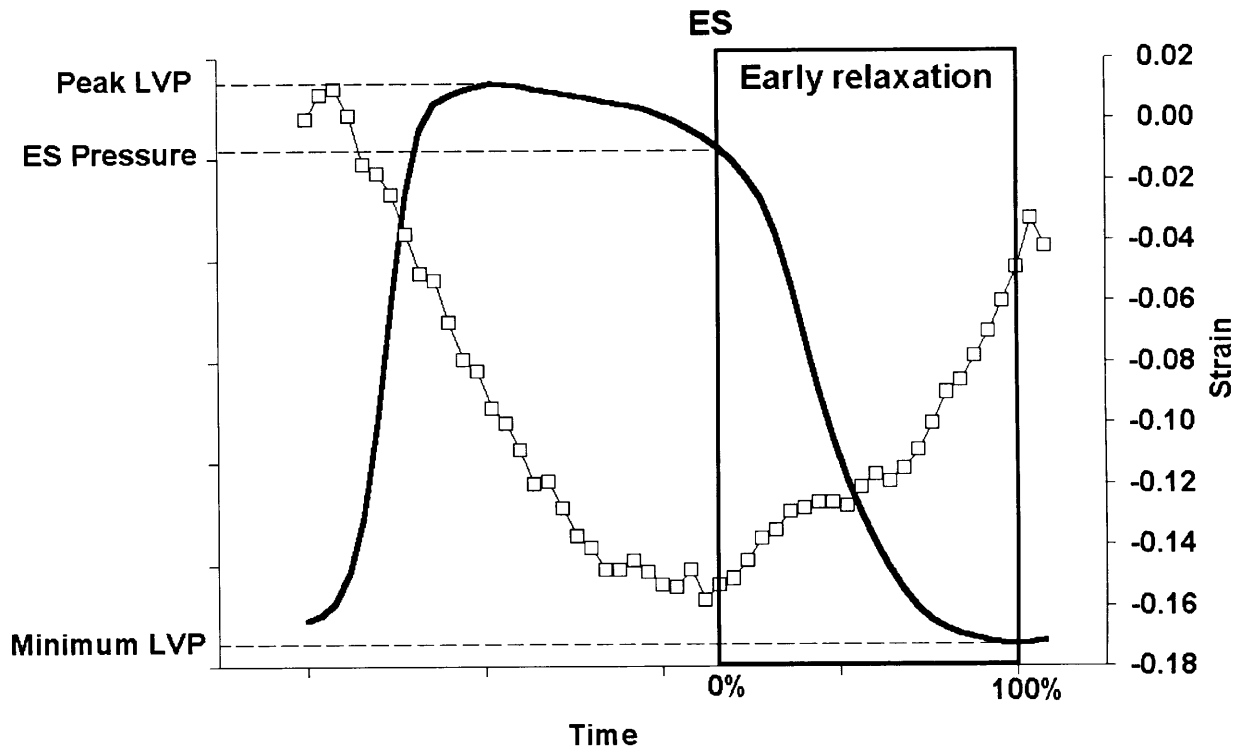


Figure 4-2. Early relaxation. Early relaxation was defined as the period beginning at end-systole (ES) and ending at minimum LV pressure (LVP, solid line). White squares represent circumferential strain (E_{11}) at midwall.

4.4 Results

4.4.1 Hemodynamic parameters

Heart rate was 133 ± 12 beats/min, LV end-diastolic pressure 9 ± 1 mmHg, LV end-systolic pressure 99 ± 6 mmHg, and LV pressure at the end of early relaxation 3 ± 2 mmHg. The duration of early relaxation was 134 ± 15 msec, and early relaxation contained 17 ± 2 data sets prior to time interpolation. The time constant of LV isovolumic pressure decay (τ) was 23 ± 5 msec (logarithmic method) (197, 247). The bead set location was 65 ± 1 % of the distance from base to apex along the LV long axis, in a region of the anterior LV free wall 1 ~ 1.5 cm away from the LAD. Mean wall thickness at the bead set location was 10 ± 1 mm, and the deepest bead was located at 91 ± 2 % wall depth.

4.4.2 Fiber and sheet orientation

Figure 4-3 illustrates the transmural distribution of the measured fiber (α) and sheet (β) angles, which were consistent among all the animals studied. The mean fiber angles (α) ranged approximately from -60° to $+60^\circ$, from epicardium to endocardium, resulting in a transmural gradient of $\sim 120^\circ$. The mean sheet angles (β) were predominantly negative with small variations across the wall ($-36^\circ \sim -2^\circ$). However, in four hearts out of five, an emergence of another sheet population $70 \sim 90^\circ$ apart within the endocardial 20% of the wall was observed, resulting in a transition of the mean sheet orientation from negative to positive in each of these four hearts. One population remained relatively constant throughout the wall, while another population coexisted only in the inner wall.

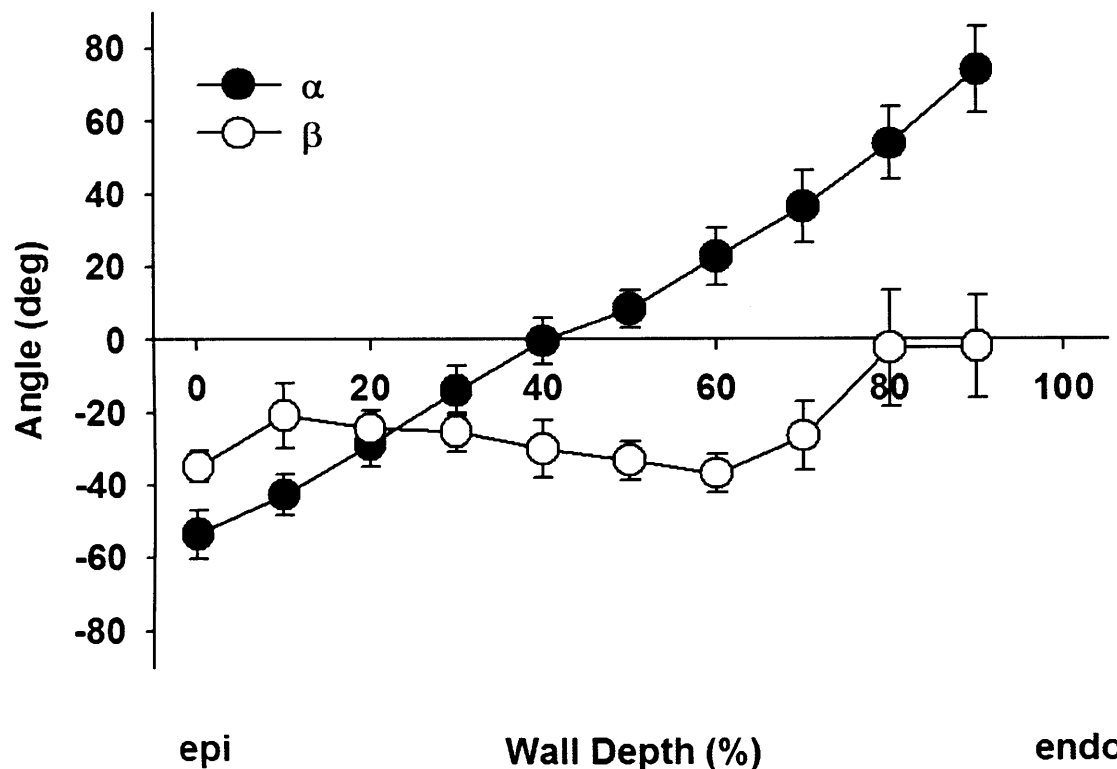


Figure 4-3. Measured fiber (α) and sheet (β) angles vs. % wall depth ($n = 5$, mean \pm SE). The mean fiber angles (α) ranged approximately from -60° to $+60^\circ$, from epicardium to endocardium, resulting in a transmural gradient of $\sim 120^\circ$. The mean sheet angles (β) were predominantly negative with small variations across the wall ($-36^\circ \sim -2^\circ$). epi: epicardium, endo: endocardium.

4.4.3 Strains during early relaxation in cardiac coordinates

Time course of local cardiac strains during early relaxation is shown in Figure 4-4. During early relaxation, significant myocardial stretch in the circumferential direction (E_{11} , $P < 0.001$), and wall thinning (E_{33} , $P < 0.001$) were observed (Table 4-1). Significant effects of depth were also observed in E_{11} ($P = 0.002$) and E_{33} ($P < 0.001$), with both circumferential stretch and wall thinning more pronounced in the endocardium than in the epicardium (Table 4-1). No significant change was observed in longitudinal stretch (E_{22}) during early relaxation ($P = 0.298$). Mean circumferential-longitudinal shear strain (E_{12}) was positive at end-systole and decreased during early relaxation ($P < 0.001$). E_{12} exhibited a significant effect of depth ($P = 0.046$), more prominent in the epicardium (Table 4-1). Transverse shear strain (E_{13}) also showed a significant change during early relaxation ($P < 0.001$).

4.4.4 Strains during early relaxation in fiber-sheet coordinates

The time course of the fiber-sheet strains during early relaxation is shown in Figure 4-5. Significant stretch along the fiber direction (E_{ff}) was observed during early relaxation ($P < 0.001$), particularly in the epicardium ($P = 0.005$, Table 4-1). In addition, sheet strain (E_{ss}) was positive at end-systole and decreased significantly during early relaxation ($P < 0.001$), with a significant effect of depth ($P = 0.007$), indicating substantial shortening of the sheet plane perpendicular to the muscle fiber axis, particularly in the endocardium ($P = 0.007$, Table 4-1). No significant change was observed in the strain normal to the fiber-sheet plane (E_{nn} , $P = 0.775$).

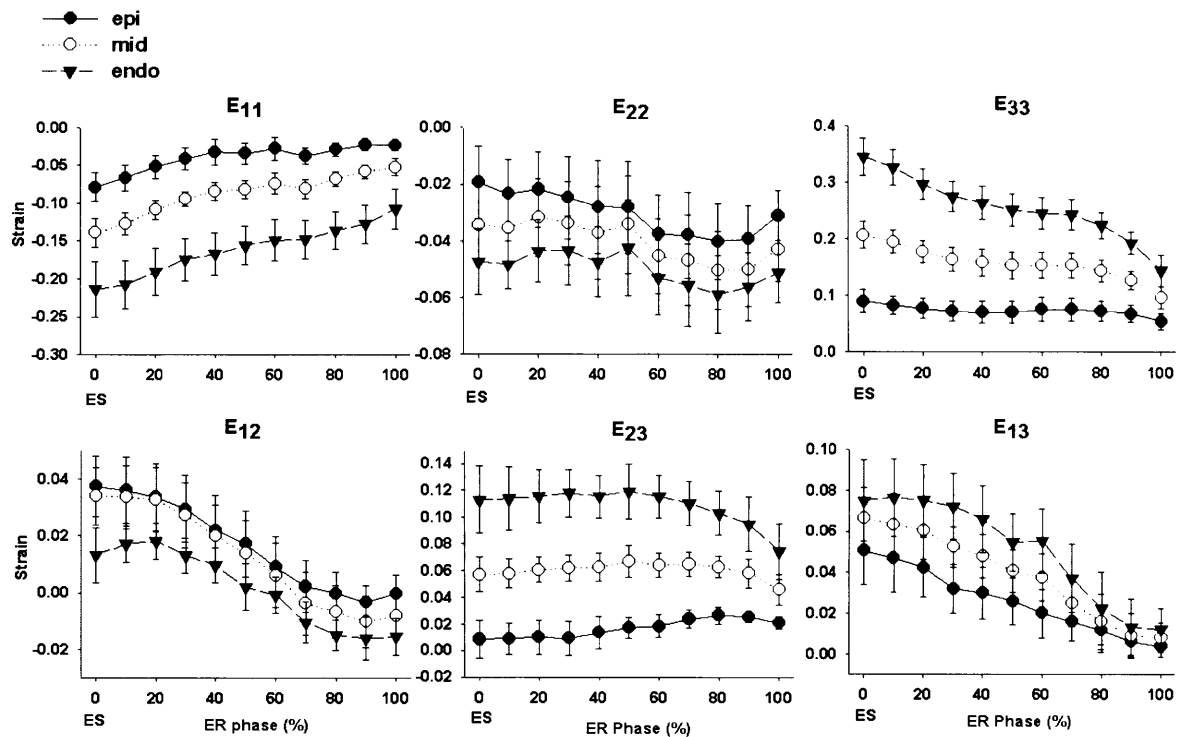


Figure 4-4. Time course of finite strains during early relaxation in local cardiac coordinates. Note significant endocardial circumferential stretch (E_{11}), endocardial wall thinning (E_{33}), epicardial torsional recoil (E_{12}), transverse shear (E_{23} , E_{13}) during early relaxation ($P < 0.05$). Values are means \pm SE. epi: epicardium, mid: midwall, endo: endocardium, ER: early relaxation. ES (end-systole, time = 0%), End of ER (time = 100%). Note different scales for each strain.

Cardiac Coordinates				Fiber-Sheet Coordinates			
Strain		ES	End of ER	Strain		ES	End of ER
$E_{11}^{*\dagger\ddagger}$	Epi	-0.079 ± 0.019	-0.023 ± 0.007	$E_{ff}^{*\dagger\ddagger}$	Epi	-0.092 ± 0.021	-0.028 ± 0.012
	Endo	-0.214 ± 0.036	-0.108 ± 0.027		Endo	-0.112 ± 0.024	-0.081 ± 0.018
E_{22}^{\dagger}	Epi	-0.019 ± 0.013	-0.031 ± 0.009	$E_{ss}^{*\dagger\ddagger}$	Epi	0.053 ± 0.010	0.026 ± 0.007
	Endo	-0.047 ± 0.012	-0.051 ± 0.010		Endo	0.189 ± 0.034	0.063 ± 0.031
$E_{33}^{*\dagger\ddagger}$	Epi	0.090 ± 0.020	0.055 ± 0.014	E_{nn}^{\dagger}	Epi	0.032 ± 0.018	0.002 ± 0.011
	Endo	0.346 ± 0.033	0.144 ± 0.028		Endo	0.008 ± 0.062	0.004 ± 0.037
$E_{12}^{*\dagger}$	Epi	0.037 ± 0.011	0.000 ± 0.006	$E_{fs}^{*\dagger\ddagger}$	Epi	0.042 ± 0.017	-0.003 ± 0.008
	Endo	0.013 ± 0.010	-0.016 ± 0.007		Endo	0.111 ± 0.037	0.058 ± 0.026
$E_{23}^{*\dagger\ddagger}$	Epi	0.008 ± 0.014	0.021 ± 0.005	E_{sn}	Epi	-0.050 ± 0.016	-0.044 ± 0.008
	Endo	0.113 ± 0.025	0.074 ± 0.021		Endo	-0.019 ± 0.113	-0.012 ± 0.054
E_{13}^{*}	Epi	0.051 ± 0.016	0.004 ± 0.005	E_{fn}^{*}	Epi	-0.020 ± 0.014	-0.004 ± 0.002
	Endo	0.075 ± 0.020	0.012 ± 0.010		Endo	-0.057 ± 0.031	-0.009 ± 0.013

Table 4-1. Two-factor repeated measures analysis of variance during early relaxation. Values for epicardial (Epi) and endocardial (Endo) strains are means \pm SE. Statistically significant ($P < 0.05$) effects of time (\star), depth (\dagger), and interaction between time and depth (\ddagger) are shown.

Significant change during early relaxation was also observed in the fiber-sheet shear strain (E_{fs} , $P < 0.001$) and the fiber-normal shear strain (E_{fn} , $P < 0.001$), and E_{fs} exhibited a significant effect of depth ($P = 0.007$). The sheet-normal shear strain (E_{sn}) did not change significantly during early relaxation (Table 4-1).

Post-hoc analysis revealed that both E_{ff} and E_{ss} achieved significant change from the end-systolic baselines ($P < 0.05$) as early as 20% into the early relaxation phase (Figure 4-5). The LV

pressure was 63 ± 6 mmHg at this time point, which was 27 msec (mean) after end-systole. Therefore, significant change in both E_{ff} and E_{ss} occurred clearly before the mitral valve opening, namely, during isovolumic relaxation.

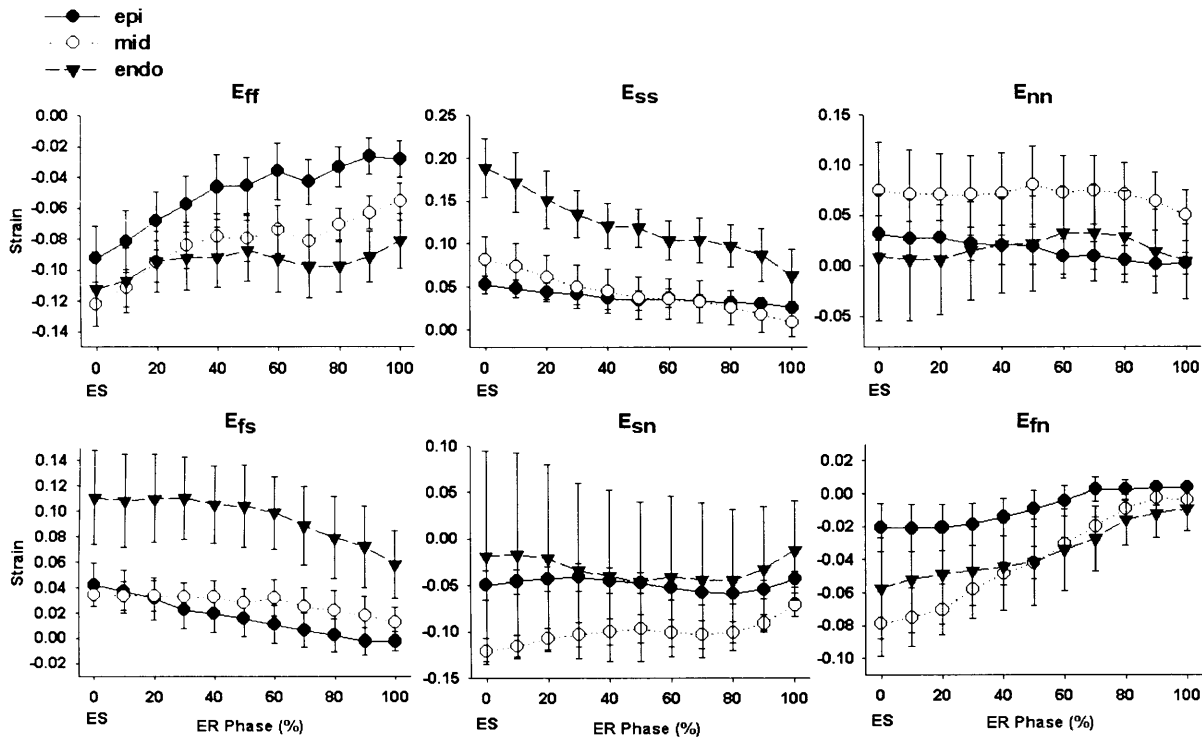


Figure 4-5. Time course of finite strains during early relaxation in fiber-sheet coordinates. Note significant epicardial stretch along the fiber direction (E_{ff}), endocardial sheet shortening (E_{ss}), fiber shear (E_{fs} , E_{fn}) during early relaxation ($P < 0.05$). Values are means \pm SE. epi: epicardium, mid: midwall, endo: endocardium, ER: early relaxation. ES (end-systole, time = 0%), End of ER (time = 100%). Note different scales for each strain.

4.5 Discussion

The objective of this study was to investigate the contribution of the fiber and sheet structures and their interaction during early relaxation. Early relaxation was defined as the time period between end-systole and the minimum LV pressure, which includes both isovolumic relaxation and early LV filling. The results indicate that early relaxation involves dynamic fiber-sheet mechanics characterized by stretch along the myofibers (E_{ff}) in the epicardial layers and shortening in the sheet plane transverse to the myofibers (E_{ss}) in the endocardial layers as well as significant shears (E_{fs} , E_{fn}). Notably, the stretch along the myofibers and the shortening in the sheet plane occurred during isovolumic relaxation before the mitral valve opening.

4.5.1 Fiber and sheet orientation

The fiber angle measurements exhibited a nearly symmetric transmural distribution with circumferential fibers located near midwall, consistent with the classic work of Streeter *et al* (225). An almost linear distribution of fiber angles was also found transmurally (Figure 4-3). Several lines of evidence suggest that both the symmetry and linearity of transmural fiber angle distribution have considerable regional variability. For example, Streeter *et al*. showed a linear distribution of fiber angles transmurally in the apical regions, and somewhat exponential distribution at the two surfaces (epicardium and endocardium) in the basal regions (225). On the

other hand, the transmural distribution of fiber orientation by Costa *et al.* was increasingly nonsymmetrical from base to apex, but was linear at both the basal and apical measurement sites (66). The symmetric and linear nature of the transmural fiber distribution in this study is likely to reflect the measurement site at the mid-anterior wall.

Although the laminar architecture of the myocardium has been recognized for many years, transmural distributions of the sheet orientation have only been obtained indirectly from measured projections in orthogonal planes (66). The direct sheet measurements in this study revealed sheet populations that have not been documented previously: two distinct populations of sheets $70 \sim 90^\circ$ apart at the most endocardial sites. Based on the hypothesis that the sheets are oriented along planes of maximum shear, Arts *et al.* (12) predicted two populations of sheets $\sim 90^\circ$ apart that occur in patches separated by distinct boundaries. Although Arts *et al.* often noticed transmural transition from one population to another, their measurements belonged to one population for a given transmural depth. In contrast, the results showed one population remaining relatively constant throughout the wall, with an emergence of another population in the inner wall. In the present study, the deepest site of the fiber-sheet strain calculation (75% wall depth) was selected above the layer where the second sheet population appears (80% wall depth), so that the coexistence of two separate families of sheet orientation would not affect the fiber-sheet mechanics data. The significance of this sheet structure near the endocardium is unknown.

4.5.2 Left ventricular mechanics during early relaxation

Finite strains at end-systole (Figure 4-4 and 4-5, ER Phase = 0%) are consistent with previous data in the literature, although significant regional variation is known (42, 66, 86, 144, 151, 176, 177, 245, 246, 258). The strains during early relaxation in cardiac coordinates (Figure 5-4) were in agreement with data in human hearts using magnetic resonance imaging (MRI) with tissue tagging (144). Although MRI is a promising tool that allows noninvasive strain measurements at multiple sites, its utility in describing cardiac mechanics during diastole has some drawbacks at present. Tagged MRI images do not provide an accurate estimate of the end-diastolic geometry, or the reference configuration, for the strain calculation, because the first image after the ECG R-wave does not show contrast between blood pool and the LV wall (144). Further, both the transmural and temporal resolution of MRI are still relatively low compared to this cineangiographic method. In addition, MRI determination of quantitative structural data is in its infancy (77, 234), and does not allow calculation of fiber and sheet dynamics (234).

In the present study, diastolic LV deformation involved complex fiber-sheet mechanics, which exhibited substantial transmural heterogeneity (Table 4-1). The wall thinning process (E_{33}) during early relaxation, which is likely to aid early ventricular filling, provided an example of intricate fiber-sheet mechanics. Costa *et al.* discovered that both sheet extension (E_{ss}) and shear (E_{sn}) contribute equally to systolic wall thickening (E_{33}), which exhibits a transmural gradient with progressively increasing strain towards the endocardium (66). Wall thinning (E_{33}) during early relaxation in this study was also greatest in the endocardium. Significant reduction in endocardial E_{33} was accompanied by reduction in endocardial E_{ss} , or sheet shortening, while E_{sn} remained unchanged. This finding implies that wall thinning during early relaxation results mainly from sheet shortening, and sheet shear E_{sn} returns to baseline later in diastole and further promotes wall thinning. This temporal sequence of sheet mechanics raises the important implication that diastolic sheet shear (E_{sn}) restoration may require substantial wall expansion resulting from ventricular filling.

E_{12} during early relaxation was most prominent in the epicardium, returning nearly to baseline at the end of early relaxation (Table 4-1 and Figure 4-4). This is consistent with the

observation that the majority of torsional recoil takes place during early relaxation (32, 34, 202, 226). Although change in global LV torsion about the LV central axis usually accompanies change in E_{12} (258), these two parameters are not equivalent. Global torsion is calculated as an angle change measured from the displacement of markers or tags about the LV central axis system, and may be most closely associated with local circumferential-radial shear (E_{13}). MRI tagging studies have provided important clues as to the relationship between these two parameters. Global LV torsion is higher in magnitude in the endocardial layers than in the epicardial layers (42, 73, 161, 202, 258), and this transmural gradient produces the E_{13} shear (258). In contrast, epicardial E_{12} is significantly greater than endocardial E_{12} in the apical and mid regions, whereas endocardial E_{12} is the greater in the basal regions (37). This may be related to the change in global LV torsion sense from counterclockwise at the apex to clockwise at the base, which is also supported by the change in sign of E_{13} from positive at the apex and negative at the base (258). Because the bead sets were located between mid and apical regions, the E_{12} and E_{13} measurements are consistent with MRI tagging data.

The data indicate significant epicardial stretch along myofibers (E_{ff}) during early relaxation (Table 4-1 and Figure 4-5). This finding is consistent with the previous work of Rodriguez *et al.* (206) who observed almost complete restitution of the sarcomere length during early relaxation in epicardial layers, but not in the endocardial layers. Epicardial predominance of fiber stretch (E_{ff}) during early relaxation supports a proposed mechanism of global torsional deformation (123). Spirally aligned myofibers in the heart convert one-dimensional fiber deformation into global LV torsional deformation. Both positive (systolic torsion) and negative (diastolic torsional recoil) torsional deformations primarily result from the sum of torque forces developed by shortening of epicardial and endocardial fibers, and because myofibers in these two surfaces are wrapped in helices of opposite sense, they develop counter-rotating torques. The epicardial fiber torque exceeds the endocardial counterpart and drives global LV torsional deformation during the bulk of systole, because epicardial fibers are at a greater radius from the LV central long axis, and thus have longer lever arms than endocardial fibers to produce a greater moment. Furthermore, the epicardium contains more fibers in a given epicardial volume shell than an endocardial volume shell of the same thickness. Therefore, global LV torsional deformation appears to be controlled by the epicardial myocardium (123).

The predominance of epicardial E_{ff} during early relaxation may also be facilitated by electrical heterogeneity of the normal heart. Epicardial fibers repolarize earlier than endocardial fibers (254), and the greater stretch of epicardial than endocardial fibers during early relaxation (E_{ff} , Figure 4-5) alters the balance of epicardial/endocardial moments, leading to torsional recoil. The critical role of epicardial myofibers during diastole is also supported by a transmural gradient in several molecular components of the myofibers. Torsional recoil is driven by restoring forces likely deriving from systolic deformation of the fiber structure, such as sarcomeric components (e.g. titin) and extracellular matrix (e.g. perimysial collagen fibers along myofibers), below slack length (111). The canine myocardium co-expresses, at the level of the half sarcomere, two main classes of cardiac titin isoforms, N2B and N2BA (53). N2B is smaller and stiffer than N2BA, and a transmural gradient in ratios of N2BA to N2B exists, decreasing from endocardium to epicardium (32). Thus, titin-based stiffness is largest at the epicardium, and progressively decreases towards the endocardium. Because there is little transmural gradient in fiber shortening (E_{ff}) at end-systole (66), the stiffer properties of titin at the epicardium would be expected to produce a greater restoring force in the epicardium than in the endocardium. In addition, a transmural gradient of myosin light chain (MLC) phosphorylation allows epicardial fibers to generate a greater force than endocardial fibers during systole, facilitating LV systolic torsional deformation (73). The MLC phosphorylation gradient produces greater systolic tension

in the epicardium, possibly resulting in a greater restoring force development in the epicardium than in the endocardium. All of these transmurally heterogeneous factors (timing of repolarization, titin isoforms and MLC phosphorylation) likely contribute to the predominance of epicardial E_{ff} observed in the current study.

Another potential source of restoring force to drive diastolic torsional recoil is systolic deformation within the sheet structure. During systole, there is significant shearing of the fibers within the sheet plane. This fiber-sheet shear (E_{fs}) exhibited a significant transmural gradient, being greater in the endocardium than in the epicardium, and decreased significantly during early relaxation (Table 4-1 and Figure 4-5). Such systolic fiber-sheet shearing is likely to accumulate energy in the deforming extracellular matrix (e.g. collagen struts connecting myofibers). Release of this energy during early relaxation could facilitate the restoration of the end-diastolic configuration of the fibers in the sheet plane, contracts the sheets (E_{ss}) to cause wall thinning (E_{33}), and contributes to torsional recoil in collaboration with epicardial fiber stretch.

4.5.3 Limitations

In the present study, 3-D finite deformation of the LV wall was examined in open-chest, anesthetized dogs at higher than normal heart rates. Therefore, the fiber-sheet dynamics that was observed may not precisely reflect the cardiac mechanics in closed-chest, awake animals. Intravenous thiopental was also used for induction anesthesia. Thiopental has cardiodepressant effects, which may have affected the local mechanics. Species difference (canine vs. human) is another factor to consider when these results are clinically extrapolated, because little is known about species variations in fiber-sheet structures. However, regional variations in cardiac strains in human are very similar, and a recent study by Bogaert *et al* (37) estimated E_{ff} in human which showed a similar transmural gradient. The fiber-sheet dynamics may also exhibit regional variations, considering substantial regional variations in the fiber and sheet distributions (66, 150, 225). The data represent the fiber-sheet mechanics in the LV mid anterior wall, and further study will be needed to clarify this point. In addition, the fiber-sheet mechanics at the very endocardial layers was not determined because of presence of two distinct sheet populations. How these two perpendicular sheet structures participate in normal cardiac mechanics at a given depth will require further study.

4.6 Conclusions

Normal LV mechanics during early relaxation involves substantial deformation of fiber and sheet structures of the myocardium. Fiber-sheet mechanics exhibited significant transmural heterogeneity during this part of the cardiac cycle, characterized by significant stretch along myofibers in the epicardial layers, sheet shortening and shear in the endocardial layers. Importantly, predominant epicardial stretch along the fiber direction occurred during isovolumic relaxation, which appears to drive global torsional recoil. These findings suggest that epicardial myofibers and extracellular structures along myofibers as well as the sheet structure between the fibers are potential sources of restoring forces during early relaxation, which control the myocardial deformation to aid early ventricular filling.

Chapter 5

Regional mechanics during relaxation in hypertrophied heart

5.1 Abstract

Diastolic dysfunction in volume overload hypertrophy by aortocaval fistula is characterized by increased passive stiffness of the LV. It was hypothesized that the changes in passive properties are associated with abnormal myolaminar sheet mechanics during diastolic filling. Three-dimensional (3-D) finite deformation of myofiber and myolaminar sheets was determined in LV free wall of 6 dogs using cineradiography of implanted markers during development of volume overload hypertrophy by aortocaval fistula. After 9 ± 2 weeks of volume overload, all dogs developed edema of extremities, pulmonary congestion, elevated LVEDP (5 ± 2 vs. 21 ± 4 mmHg, $P < 0.05$) and increased LV volume. There was no significant change in systolic function (dP/dt_{\max} 2476 ± 203 vs. 2330 ± 216 mmHg/s, $P = \text{n.s.}$). Diastolic relaxation was significantly reduced (dP/dt_{\min} -2466 ± 190 vs. -2076 ± 166 mmHg/s, $P < 0.05$; τ 32 ± 2 vs. 43 ± 1 ms, $P < 0.05$), while duration of diastolic filling was unchanged (304 ± 33 vs. 244 ± 42 ms, $P = \text{n.s.}$). Fiber stretch and sheet shear occur predominantly in the first third of diastolic filling, and chronic volume overload induced remodeling in lengthening of the fiber and reorientation of the laminar sheet architecture. Sheet shear was significantly increased and delayed at the subendocardial layer ($P < 0.05$), whereas the magnitude of fiber stretch was not altered in volume overload ($P = \text{n.s.}$). These findings indicate that enhanced filling in volume overload hypertrophy is achieved by enhanced sheet shear early in diastole. These results provide the first evidence that changes in the motion of radially oriented laminar sheets of the myocardium may play an important functional role in the pathology of diastolic dysfunction in this model.

5.2 Introduction

The laminar structure of the myocardium consists of radial arrangement of myofiber bundles approximately four cells thick with extensive cleavage planes between the laminae (150). It has been established that the myolaminar sheets provide the key mechanism of regional systolic (66) and diastolic (17) function. For example, local shearing of the sheet structure is an important mechanism of ventricular wall thinning during diastole (17, 222).

Heart failure due to chronic volume overload induced by aortocaval fistula is associated with significant increase in passive stiffness of the LV (120, 165). One of the potential mechanisms may be remodeling of the extracellular matrix (ECM) during hypertrophy (113, 120). Because the myocardial sheet structure is enclosed and interconnected by the ECM (150), the ECM remodeling may mitigate the normal sheet mechanics, thus increasing the overall passive stiffness of the ventricle during diastole. Moreover, previous studies suggest that sheet shear may play an important role during diastolic filling (17, 230). Therefore, it was hypothesized that the changes in passive properties in chronic volume overload heart failure are associated with abnormal sheet mechanics during diastolic filling.

To test this hypothesis, myocardial 3-D finite deformation was determined in the LV anterior wall of dog *in vivo* in volume overload hypertrophy. The time course of myocardial strains in fiber-sheet coordinates referred to the end-diastolic configuration was determined during diastolic filling. Thus dynamic changes during diastolic filling were studied at the level of myofibers and sheet structures before and after development of diastolic dysfunction.

5.3 Materials and Methods

5.3.1 Experimental protocol

Six adult mongrel dogs (21-25 kg) were anesthetized with intravenous thiopental (8-10 mg/kg), mechanically ventilated with isoflurane (0.5-2.5%) and nitrous oxide (3L/min). Under

sterile conditions, the heart was exposed through a left thoracotomy at the fourth intercostal space. Gold beads (2mm) were sutured to the apical dimple (apex bead, Figure 5-1A) and at the bifurcation of the LAD and LCx (base bead, Figure 5-1A). To measure 3D myocardial deformation in each heart, transmural marker arrays or a 'bead set' was placed within the LV anterior free wall (Figure 5-1A, B), as described previously (17, 245). Briefly, an 8mm-thick Plexiglas template was sutured to the epicardium, with three holes forming a 10mm equilateral triangle to act as guides for the bead insertion trocar. Four to six 0.8mm-diameter gold beads were inserted one by one to create a total of three columns of beads spanning from endocardium to epicardium (Figure 5-1B). After the bead insertion was complete, the platform was removed, and a 1.7mm-diameter surface gold bead was sewn onto the epicardium above each column. Through a stab wound in the apex, a precalibrated micromanometer pressure catheter (model P6, Konigsberg Instruments, Inc., Pasadena, CA) was inserted to monitor LV pressure. A 9-Fr silicone catheter (IntiSilf, Access Technologies, Skokie, IL) was inserted into the left atrium (LA) to monitor LA pressure, which was used in every imaging study to correct for baseline drifting of the LV micromanometer. The chest was closed, and the animals were allowed to recover for 7-10 days. Control imaging studies were performed for each animal. Under sedation with intravenous propofol (5.5-7.0 mg/kg), the dogs were suspended in a sling in a biplane X-ray system (152).

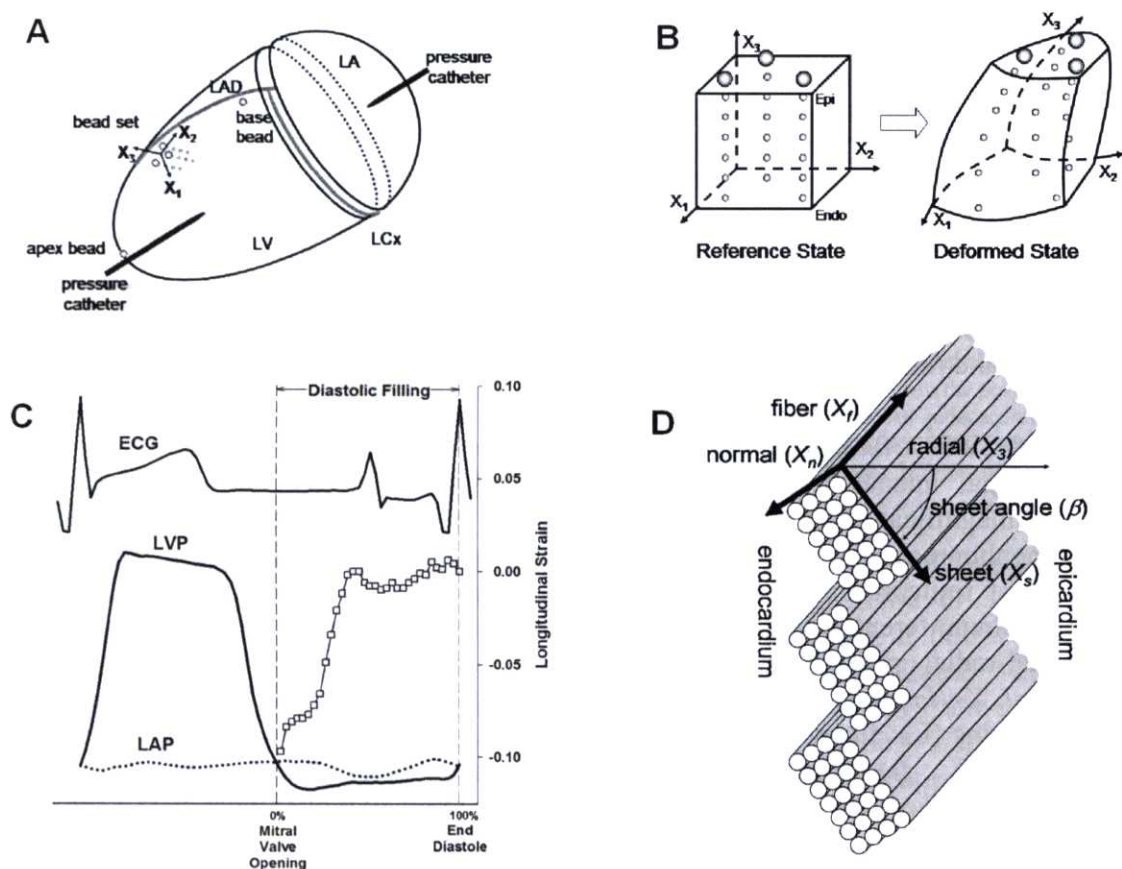


Figure 5-1. *A. Schematic representation of the heart.* X_1 : circumferential axis, X_2 : longitudinal axis, X_3 : radial axis, LAD: left anterior descending coronary artery, LCx: left circumflex coronary artery, LV: left ventricle, LA: left atrium. A precalibrated micromanometer pressure catheter was inserted into apex to monitor LV pressure. A 9-Fr silicone catheter was inserted into LA to monitor LA pressure, which was used in every imaging study to correct for baseline drifting of the LV micromanometer. *B. Bead set* consisted of three transmural columns of 4-6 gold beads (0.8mm) and a surface gold bead (1.7mm) above each column. Finite deformation of the myocardium was calculated from displacement of each material point (= bead) in space. *C. Diastolic filling.* ECG: surface electrocardiogram, LVP: left ventricular pressure, LAP: left atrial pressure. Diastolic filling was defined as

the period beginning at mitral valve opening (time=0%, pressure crossover of LVP and LAP) and ending at end diastole (time=100%, peak of ECG R-wave). White squares in the figure represent longitudinal strain (E_{22}) at 80% wall depth in a control animal. *D. Fiber-sheet coordinate system.* Each cylinder represents a myofiber. Myofibers are organized into laminar “sheets”, which are approximately four cells thick and roughly stacked from apex to base (150). Sheet angle (β) is measured with reference to the positive radial axis (X_3).

Biplane cineradiographic images (125 frames/sec) of the bead markers were digitally acquired (17) for at least one full respiratory cycle, and data used in the analysis were taken near end-expiration to minimize the effects from respiratory variation. Then through an abdominal incision under general anesthesia, the aorta and inferior vena cava were exposed below the renal arteries and a 1.0-1.2 cm side-to-side anastomosis was constructed (193, 231). The abdomen was closed, and patency of the shunt was evidenced by an audible murmur throughout the study. Imaging studies were repeated every week for 9 ± 2 weeks follow-up (see Results). After the final sedated imaging study, the animal was anesthetized and mechanically ventilated. In order to fix each heart in the end-diastolic configuration in a controlled manner at a known LV end-diastolic pressure (EDP), median sternotomy was performed and another imaging study was conducted at end expiration with LVEDP adjusted by phlebotomy to match the LVEDP in the control study. The animal was then euthanized with pentobarbital sodium, and the heart was perfusion-fixed *in situ* with 2.5% buffered glutaraldehyde at the LVEDP in the control study (257).

5.3.2 Histology

Because the heart was fixed at the same LVEDP, fiber and sheet angles in the fixed hearts were assumed to represent the fiber-sheet structure (150, 225) in the end-diastolic reference configuration of the final study *in vivo* matched to the LVEDP of the control study (17, 21, 66, 230). To avoid the distortional effects of dehydration and embedding, histological measurements were obtained using freshly fixed heart tissue (17, 21, 66, 230). In the transmural block of tissue within the implanted marker set, the fiber (α) and sheet angles (β) were determined from epicardium to endocardium at every 1-mm-thick section sliced parallel to the epicardial tangent plane, as described previously (17). α and β were measured with reference to the positive circumferential and radial axes, respectively (Figure 5-2).

5.3.3 Finite strain analysis

The digital images from the X-ray image intensifiers were corrected for spherical distortion and magnification to reconstruct the 3D coordinates of the markers in each frame, and continuous, nonhomogeneous transmural distributions of 3D finite strains were calculated (17). Six independent finite strains (E_{11} : circumferential strain, E_{22} : longitudinal strain, E_{33} : radial strain, E_{12} : circumferential-longitudinal shear, E_{23} : longitudinal-radial shear, and E_{13} : circumferential-radial shear) were computed in the local cardiac coordinate system (X_1 : circumferential, X_2 : longitudinal, X_3 : radial axis) (172), which were used to compute another set of six finite strains (E_{ff} : fiber strain, E_{ss} : sheet strain, E_{nn} : strain normal to the sheet plane, E_{fs} : fiber-sheet shear, E_{sn} : sheet shear and E_{fn} : fiber shear) in the local fiber-sheet coordinate system (X_f : fiber axis, X_s : sheet axis, X_n : axis normal to fiber-sheet plane) (Figure 5-1C) through an orthogonal transformation using α and β at each depth (66). In layers where two separate sheet populations were present (see results), the mode of the dominant sheet population was used to calculate sheet strains. α and β at a given time point in control and hypertrophy were calculated from myocardial deformation with the configuration of the respective time point as the deformed state and the end-diastolic configuration of the final open-chest study with matched LVEDP as the reference state (230). In each set of finite strains, three normal strain components reflect myocardial stretch or shortening along each axis, and three shear strains represent angle changes

between pairs of the initially orthogonal axes. The data analysis includes fiber strain (E_{ff}), sheet strain (E_{ss}), and sheet shear (E_{sn}). Because the sign of sheet shear can be positive or negative depending on β , the absolute value of E_{sn} was used in the data analysis to reflect the absolute change of sheet shear from the reference configuration at end diastole.

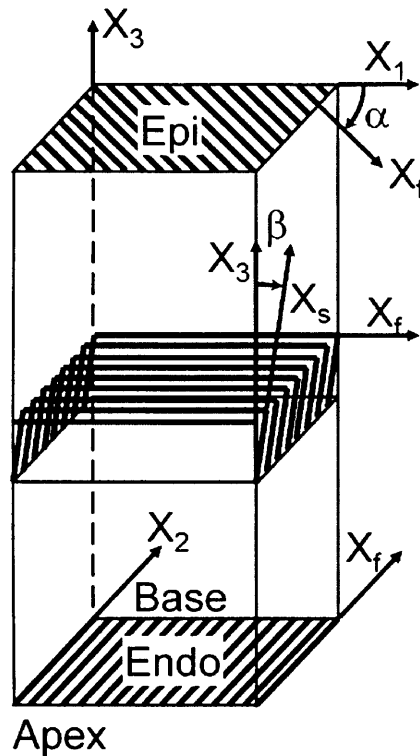


Figure 5-2. Illustrative account of fiber (α) and sheet (β) angle measurement. A transmural rectangular block of tissue in the implanted bead set was carefully removed from the ventricular wall, with the edges of the block cut parallel to the local circumferential (X_1), longitudinal (X_2) and radial (X_3) axes of the LV. The block was sliced into 1mm-thick sections parallel to the epicardial tangent plane. In each 1mm-slice tissue, fiber angle (α) was measured with reference to the positive circumferential axis (X_1). Note the orientation of the fiber axis (X_f) rotates counterclockwise from epicardium to endocardium. The 1mm-slice tissue was sectioned perpendicular to the mean fiber direction, and sheet angle (β) was measured in the section plane with reference to the positive radial axis (X_3). This process was repeated in all the 1mm-slice tissues from the epicardium (Epi) to the endocardium (Endo). X_s : sheet axis.

Transmural finite strains were calculated for each frame as a deformed configuration during diastolic filling, with end diastole (ED, peak of ECG R-wave) as the reference configuration. Diastolic filling was defined as the period beginning at mitral valve opening (MVO, crossover of LV and LA pressures) and ending at end diastole (Figure 5-1B). The strain data in each animal during diastolic filling were linearly interpolated at 10% increments in time between MVO (time=0%) and ED (time=100%). The strain time course was determined at three wall depths: 20% (subepicardium), 50% (midwall) and 80% (subendocardium) depth from the epicardial surface.

5.3.4 Statistical analysis

Values presented are means \pm SE, unless otherwise specified. A paired t-test was used to compare hemodynamic parameters. Two-factor repeated measures analysis of variance (ANOVA) was used to determine the effects of hypertrophy and depth on transmural fiber and sheet angles, and the effects of hypertrophy and time during diastolic filling on each strain

component. The Student-Newman-Keuls method was used for ANOVA post-hoc analysis. Statistical tests were performed using SigmaStat 3.0 (SPSS, Inc. Chicago, IL). Statistical significance was accepted at $P < 0.05$.

5.4 Results

The dogs were followed for 9 ± 2 weeks after construction of the fistula, and all dogs ($n=6$) developed clinical signs of heart failure, including edema of extremities, pulmonary congestion, elevated LVEDP and increased LV volume estimated from the apex-base length and basal diameter (20). However, there was no significant change in body weight (22.3 ± 0.6 vs. 22.5 ± 0.8 kg, $P=n.s.$). The measurement site was located $68 \pm 4\%$, of the distance from base to apex along the LV long axis, in a region of the anterior LV free wall 1~2cm septal of the anterolateral papillary muscle. Mean wall thickness at the measurement site was 11 ± 1 mm, and the deepest bead was located at $97 \pm 3\%$ wall depth from the epicardial surface. The heart weight was 280 ± 31 g, LV weight was 171 ± 18 g, and the ratio of LV weight (g) to body weight (kg) (LV/BW) was 7.7 ± 0.9 g/kg. Volume changes within the bead sets indicated a 21 % increase in the myocardial tissue volume at the measurement site.

5.4.1 Hemodynamic parameters

All the animals remained in sinus rhythm for the entire duration of the study. Although the heart rate increased from 105 ± 9 to 130 ± 12 bpm, the duration of diastolic filling was variable and there was no significant difference between control and hypertrophy (304 ± 33 vs. 244 ± 42 ms, $P=n.s.$) (Table 5-1). The indices of systolic function (LVP_{max} and dP/dt_{max}) were unchanged ($P=n.s.$), whereas those of relaxation were significantly altered in hypertrophy. The magnitude of dP/dt_{min} decreased (-2466 ± 190 vs. -2076 ± 166 mmHg/sec, $P<0.05$), and τ , the time constant of isovolumic LV pressure decline (174, 219, 247), significantly prolonged from 32 ± 2 to 43 ± 1 ms ($P<0.05$).

	Control	Hypertrophy	P value
Heart rate (bpm)	105 ± 9	130 ± 12	<0.05
LVP_{max} (mmHg)	113 ± 7	117 ± 5	n.s.
LVP at MVO (mmHg)	4 ± 2	19 ± 4	<0.01
LVEDP (mmHg)	5 ± 2	21 ± 4	<0.05
Diastolic filling (ms)	304 ± 33	244 ± 42	n.s.
dP/dt_{max} (mmHg/sec)	2476 ± 203	2330 ± 216	n.s.
dP/dt_{min} (mmHg/sec)	-2466 ± 190	-2076 ± 166	<0.05
τ (ms)	32 ± 2	43 ± 1	<0.05

Table 5-1. Hemodynamic parameters. Values are means \pm SE ($n=6$). LVP_{max} : maximum left ventricular pressure, MVO: mitral valve opening, LVEDP: left ventricular end-diastolic pressure, dP/dt_{max} , dP/dt_{min} : peak positive and negative dP/dt , respectively, τ : time constant of isovolumic LV pressure decline, fiber strain: E_{ff} , sheet strain: E_{ss} , sheet shear: E_{sn} .

5.4.2 Transmural fiber and sheet angles

There was no difference in transmural fiber angle distribution between control and hypertrophy at MVO. Either in control and hypertrophy, transmural fiber angles did not significantly change from MVO to ED ($P=n.s.$) (Figure 5-3). Similarly, transmural sheet angles did not change during diastolic filling in control ($P=n.s.$). In contrast, transmural sheet angles significantly decreased from MVO to ED in hypertrophy ($P<0.05$). Because transmural sheet

angles were negative at MVO, a decrease in angle indicates that the sheets become more oblique to the radial axis towards end diastole in hypertrophy, contributing to diastolic wall thinning (Figure 5-4).

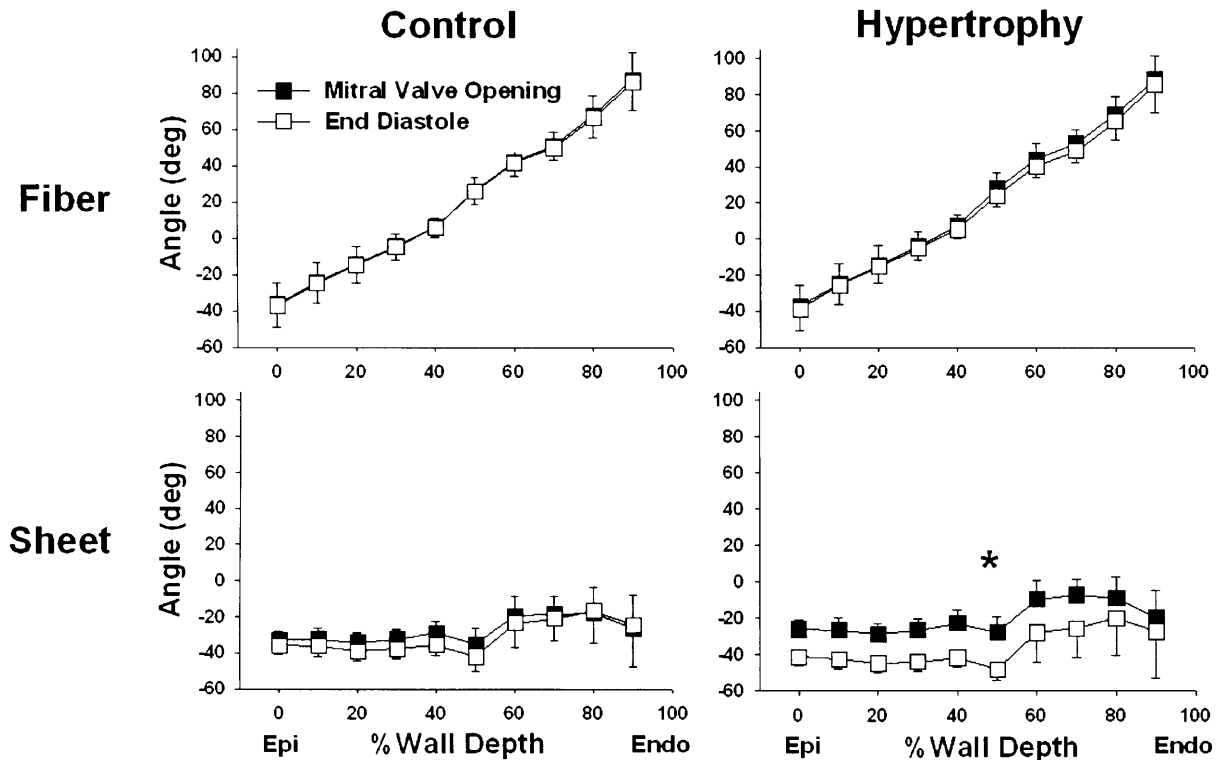


Figure 5-3. Transmurals fiber and sheet angles during diastolic filling. Values are means \pm SE (n=6). Closed square: mitral valve opening, open square: end diastole, Epi: epicardial surface, Endo: endocardium. Both in control and hypertrophy, transmural fiber angles did not significantly change from mitral valve opening to end diastole ($P=n.s.$). Similarly, transmural sheet angles did not change during diastolic filling in control ($P=n.s.$). In contrast, transmural sheet angles significantly decreased from mitral valve opening to end diastole in hypertrophy (*: $P<0.05$).

5.4.3 Strain time course

Figure 5-5 shows the time course of cardiac strains at the control study during at subepicardial and subendocardial layers. The reference configuration was ED for each contraction. All cardiac strain components exhibited a substantial transmural gradient at MVO which was less apparent later in diastole. The greatest change in strain values occurred in the first third of the diastolic filling, or early ventricular filling. For example, E_{33} at the endocardium achieved 73% of the total diastolic deformation during the first third of diastole (0.297 ± 0.063 to 0.081 ± 0.024). Typically, there was little deformation in the last third of the diastolic filling period, which is consistent mechanically with the E/A ratio >1 in transmitral flow measurement of normal heart.

Figure 5-6 shows the time course of strains rotated into the fiber-sheet coordinate system and calculated with two different reference configurations. Figure 5-6A shows strain values calculated with the reference configuration at ED in control, which illustrates both the tissue remodeling and increase in diastolic dimensions that occurred with volume overload hypertrophy. Note that at MVO (diastolic filling period=0%), fiber strains (E_{ff}) in hypertrophy were significantly greater than control indicating that tissue in the fiber direction is substantially longer in hypertrophy. These changes were sustained throughout the diastolic filling period, and ED fiber strain in hypertrophy at the subepicardium and subendocardium was 0.106 ± 0.032 and

0.159 ± 0.053 , respectively, indicating that the myofibers underwent a stretch of greater than 10% at each diastole relative to the control heart.

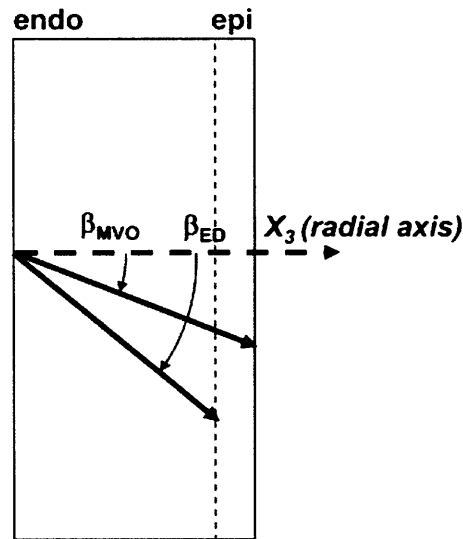


Figure 5-4. Direction of sheet angle change during diastolic filling. Endo: endocardium, epi: epicardium, X_3 : radial axis, β_{MVO} , β_{ED} : sheet angle at mitral valve opening (MVO) and end diastole (ED), respectively. Because transmural sheet angles were negative at MVO, a decrease in sheet angle during diastolic filling (Fig. 2) indicates that the sheets become more oblique to the radial axis towards ED.

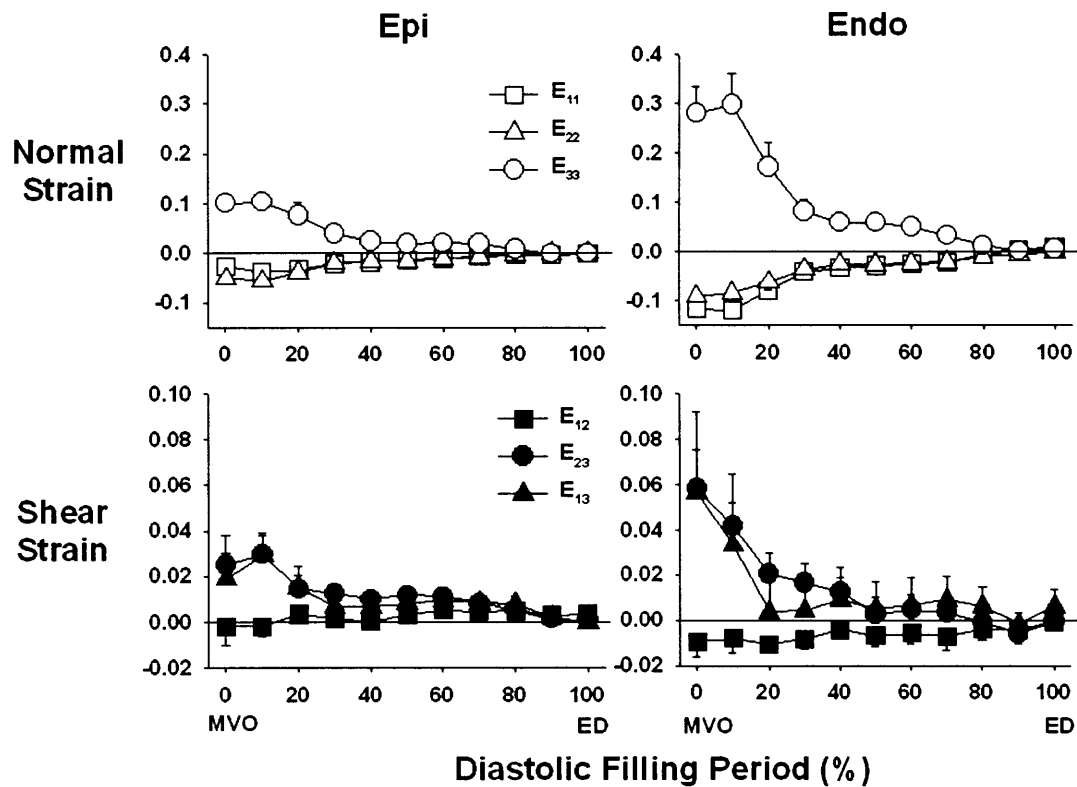


Figure 5-5. Cardiac strain time course during diastolic filling in control. Values are means \pm SE ($n=6$). Epi, endo: 20%, 80% wall depth from the epicardial surface, respectively. MVO: mitral valve opening, ED: end diastole.

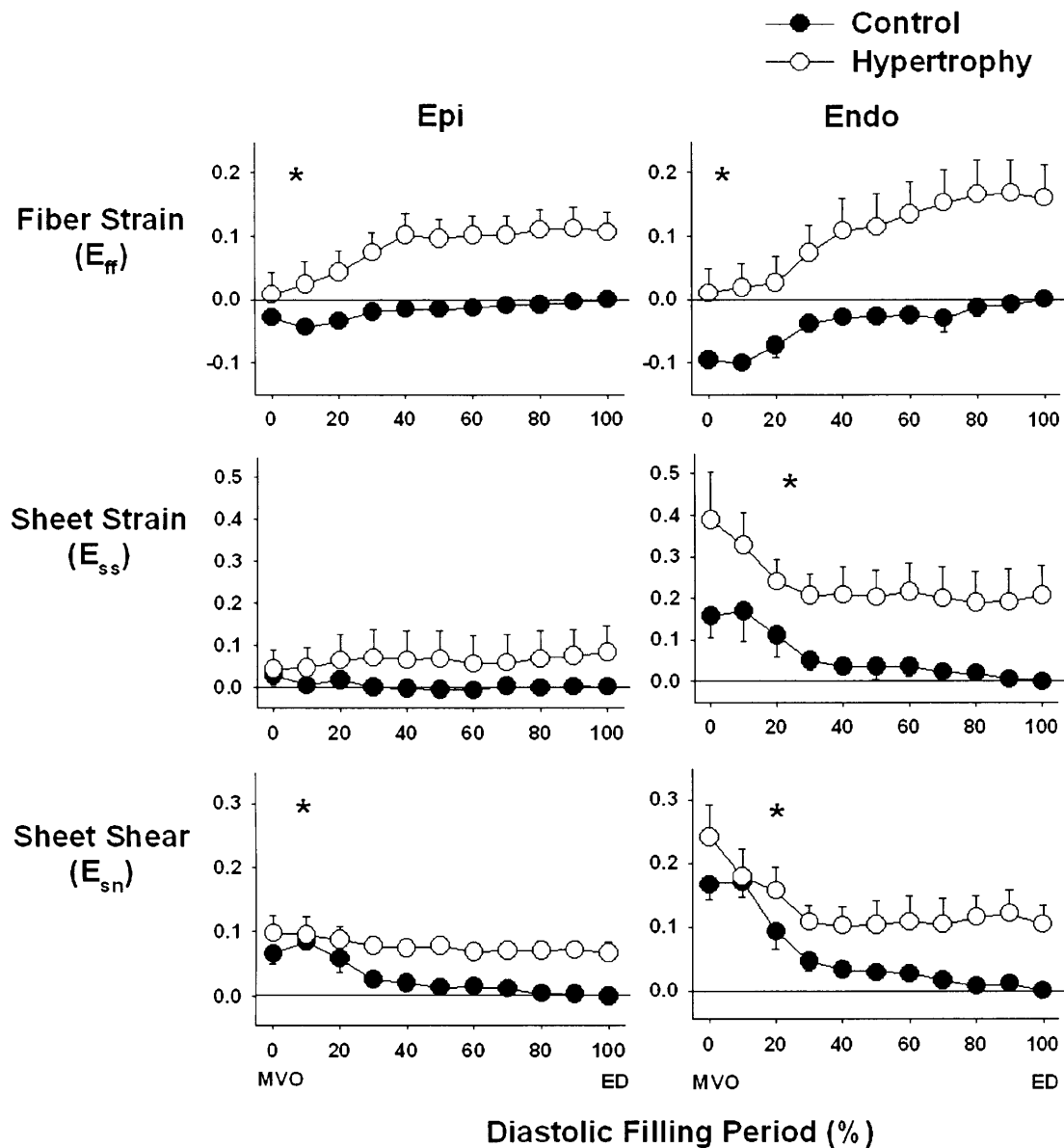


Figure 5-6A. Fiber-sheet strain time course during diastolic filling. The reference configuration for both control and hypertrophy was determined at the end diastole of the control study. Values are means \pm SE ($n=6$). Fiber strain: E_{ff} , sheet strain: E_{ss} , sheet shear: E_{sn} . Epi, endo: 20%, 80% wall depth from the epicardial surface, respectively. MVO: mitral valve opening, ED: end diastole. Closed circle: control, open circle: hypertrophy. *: $P<0.05$ by two-factor repeated measures ANOVA (control vs. hypertrophy).

As a result, the time course of fiber strain between control and hypertrophy was significantly different ($P<0.05$). Sheet strain at subepicardium in both control and hypertrophy was small during diastolic filling, and there was no significant difference in the time course between control and hypertrophy. In contrast, subendocardial sheet strain was significantly greater in hypertrophy than in control. At MVO, sheet strain in hypertrophy was 0.388 ± 0.116 , whereas that of control was 0.157 ± 0.053 . ED sheet strain in hypertrophy at subendocardium was 0.205 ± 0.073 , indicating that there was a diastolic extension in the sheet direction of approximately 20% relative to the control heart. At both subepicardium and subendocardium, this shear strain was greater in hypertrophy than in control during diastolic filling.

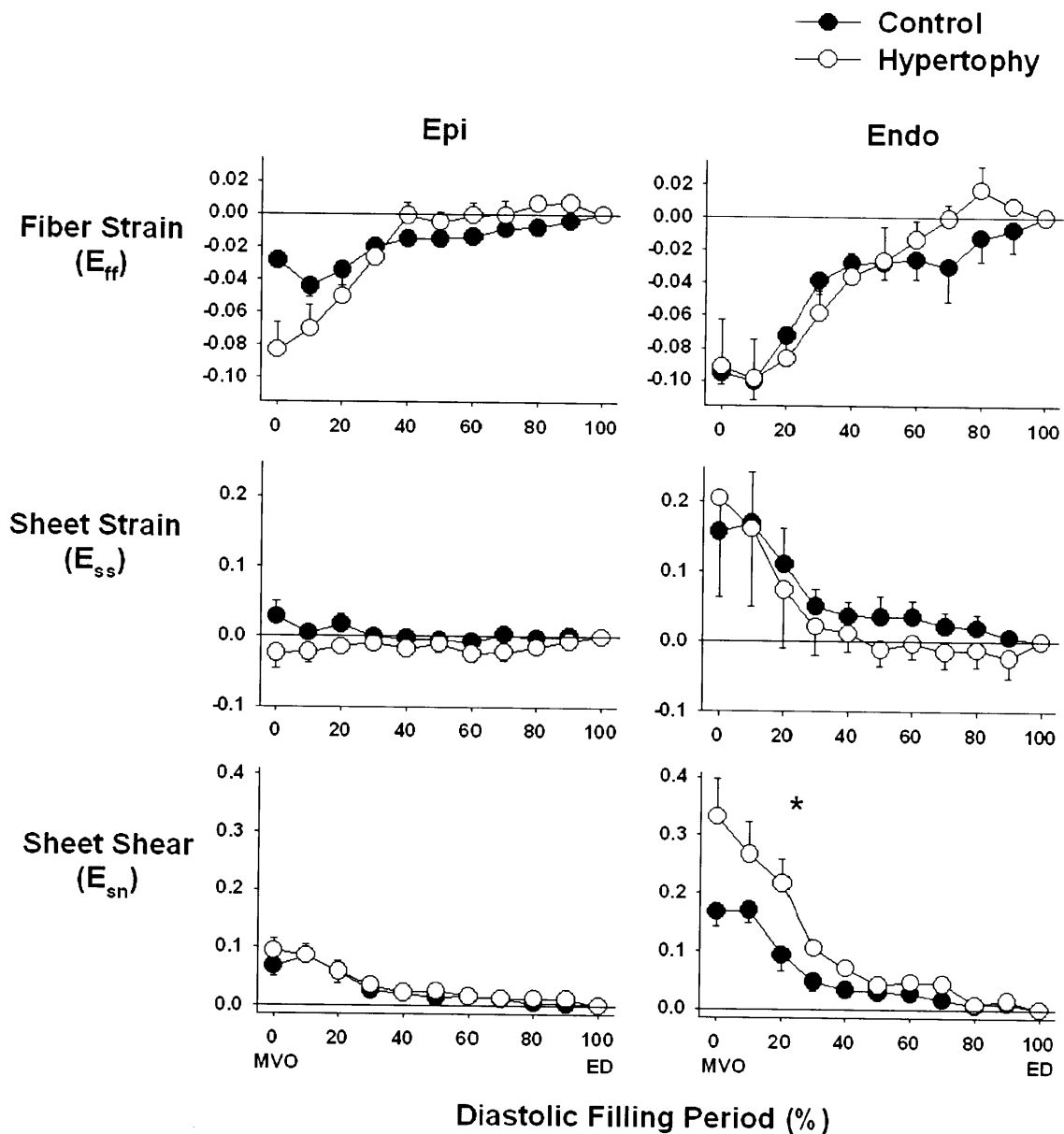


Figure 5-6B. Fiber-sheet strain time course during diastolic filling. The reference configuration for control and hypertrophy was determined at the end diastole of the control and hypertrophic state, respectively. Values are means \pm SE (n=6). Fiber strain: E_{ff} , sheet strain: E_{ss} , sheet shear: E_{sn} . Epi, endo: 20%, 80% wall depth from the epicardial surface, respectively. MVO: mitral valve opening, ED: end diastole. Closed circle: control, open circle: hypertrophy. *: $P < 0.05$ by two-factor repeated measures ANOVA (control vs. hypertrophy).

To compare the time course of diastolic deformation in control and volume-overload hypertrophy independent of end-diastolic remodeling, another set of fiber-sheet strains was calculated with the reference configuration at ED of the respective state (Figure 5-6B). The overall time course of fiber strain was not significantly different between control and hypertrophy ($P = \text{n.s.}$), indicating that hypertrophy did not affect fiber stretch during diastolic filling relative to ED configuration. At the subepicardium, the majority of the fiber deformation (E_{ff}) occurred during the first third of the diastolic filling period in both control and hypertrophy. In contrast, at the subendocardium, there is substantial deformation in hypertrophy occurring

during diastasis and in the last third of diastole, corresponding to the time of atrial contraction. Sheet strain (E_{ss}) was greater at subendocardium than subepicardium in both control and hypertrophy, and there was no significant difference in the time course between control and hypertrophy ($P=n.s.$). Sheet shear (E_{sn}) in control showed a significant transmural gradient, being greater at subendocardium than subepicardium (0.167 ± 0.025 vs. 0.067 ± 0.017 , $P < 0.05$). Sheet shear in hypertrophy exhibited an even greater transmural gradient with a marked increase of sheet shear at subendocardium compared with subepicardium (0.331 ± 0.067 vs. 0.094 ± 0.021 , $P < 0.05$). As a result, there was a significant difference in the time course of the sheet shear at subendocardium between control and hypertrophy ($P < 0.05$). Because end-systolic sheet shear strains in control and hypertrophy were similar (Table 5-2), this result indicates that hypertrophy caused a significant delay, or rightward shift, of the time course of sheet shear during diastole.

End-systolic strains	Control	Hypertrophy	P value
Fiber strain (E_f)	-0.104 ± 0.010	-0.108 ± 0.008	n.s.
Sheet strain (E_{ss})	0.136 ± 0.029	0.121 ± 0.071	n.s.
Sheet shear (E_{sn})	-0.123 ± 0.023	-0.146 ± 0.036	n.s.

Table 5-2. End-systolic strains.

5.5 Discussion

The aim of the present study was to examine the changes in diastolic deformation in the LV wall after hypertrophic growth induced by chronic volume overload. As the myocardium remodeled in response to volume overload, there was elongation in both the fiber and sheet directions, which were particularly prominent at the endocardium, and the orientation of the laminar sheets of the myocardium became less radial. The results show for the first time that the majority of fiber deformation in the anterior LV free wall occurs during the first third of the diastolic filling period and there is little or no fiber strain late in diastole. During the early diastolic time period there was also substantial shearing deformation, which was particularly prominent in the endocardium following volume overload. This enhanced shearing deformation was not accompanied by increased fiber strain. These results imply that the enhanced early diastolic filling is associated primarily with remodeling-induced changes in the laminar architecture.

5.5.1 Diastolic hemodynamics and volume overload hypertrophy

LV filling dynamics is a result of a complex interaction of filling pressure (256), mitral valve mechanics (130) and LV wall properties (32), which is primarily determined by active relaxation and passive stiffness (67, 267). Impairment of these LV wall properties is associated with a clinical syndrome characterized by the signs and symptoms of heart failure despite preserved systolic function (266, 267). The concept of “diastolic heart failure” is clinically well characterized (1, 240), and it represents a major public health issue that accounts for almost a half of all heart failure cases (239) and >25% of the total cost of heart failure treatment (71, 191). Nevertheless, the proposed mechanism of diastolic heart failure is widely heterogeneous (268), and at a basic level, whether or not there exists consistent abnormality of intrinsic diastolic properties that can explain the occurrence of diastolic heart failure is still a topic of active debate (46, 132, 266).

In chronic volume overload induced by aortocaval shunt, diastolic dysfunction in both active relaxation and passive stiffness has been documented. The LV end-diastolic pressure-volume curve in this model of chronic volume overload is similar to that of clinically observed

chronic volume overload, most commonly mitral and aortic regurgitation. Both are characterized by a progressive rightward shift and an increase in the slope, or passive stiffness (51, 64, 165). The rightward shift of the curve in chronic volume overload is ascribed not only to myofiber elongation (100, 193) and rearrangement (20) but also to diastolic creep, or time-dependent elongation of myofiber (6, 165), which may be present in pressure overload (154) and chronic infarction, where infarct scar tissue has replaced portions of the LV (127). In the present study, diastolic relaxation was significantly reduced despite no significant change in indices of systolic function. Therefore, this preparation appears to be a good model of diastolic dysfunction. The present study has identified abnormal sheet mechanics in this model of diastolic dysfunction, however, whether this mechanical abnormality may or may not be found in the clinical population of diastolic heart failure remains to be seen.

5.5.2 Diastolic fiber and sheet mechanics and volume overload hypertrophy

Results of the present study indicate that the majority of diastolic deformation in the LV anterior wall occurs during the first third of the diastolic filling period. This temporal pattern is consistent with the diastolic deformation obtained noninvasively in human by tagged MRI (144) and ultrasound strain rate imaging (112). There is little or no fiber strain late in diastole (Figure 5-5). During early diastolic filling there was substantial shearing deformation, which was particularly prominent in the endocardium following volume overload (Figure 5-6B). To examine the remodeling that occurs in the ventricular wall following volume overload, the diastolic strains with the initial control ED as the reference were examined. The results demonstrate that fiber strain, sheet strain and sheet shear strain were significantly greater in hypertrophy compared to control (Figure 5-6A). Although the study was not designed to separate the factors responsible for these changes, the increase in tissue length is compatible with the known increases in cell length, cell rearrangement, and increases in diastolic pressure observed in this model (20, 100, 193). There was also a significant increase in the change of transmural sheet angles between control and hypertrophy during diastolic filling (Figure 5-3), likely reflecting an increased filling due to volume overload. However, because end-diastolic remodeling in β between control and hypertrophy was not significant (20), the dynamic decrease of β during diastolic filling in hypertrophy is mainly accounted for by a change of β at MVO (Figure 5-3 and 5-7).

To more clearly elucidate the effects of ventricular filling on deformation in the LV wall and to partially separate them from the effects of tissue remodeling, strains calculated with ED of each contraction as the reference configuration were examined (Figure 5-6B). Fiber and sheet strains with reference to the end-diastolic configuration of the hypertrophic state were similar to those of the control state. Because both diastolic volume and stroke volume are increased in this model (165, 207, 208, 231), the lack of increase in fiber strain during diastole following volume overload was an unexpected finding.

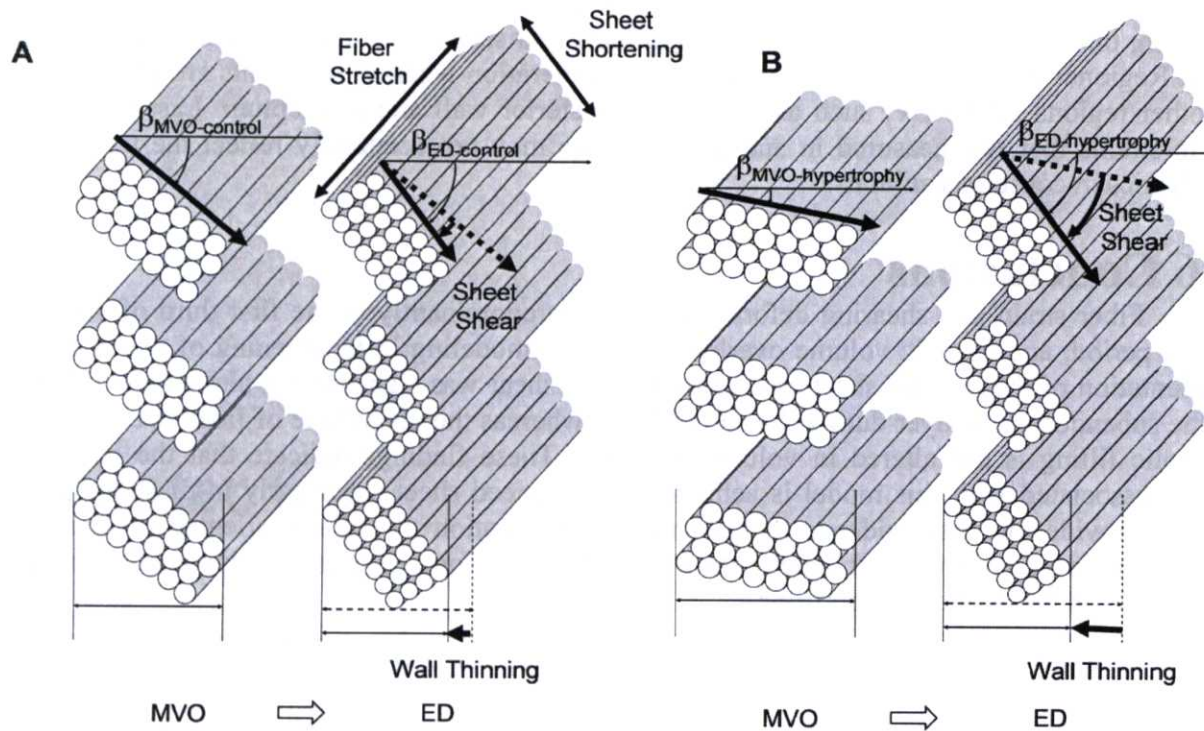


Figure 5-7. Schematic representation of fiber-sheet strains during diastolic filling. A: control, B: hypertrophy. β_{ED} is not significantly different between control ($\beta_{ED-control}$) and hypertrophy ($\beta_{ED-hypertrophy}$). In contrast, β_{MVO} is greater in control ($\beta_{MVO-control}$) than in hypertrophy ($\beta_{MVO-hypertrophy}$). The net result is a significantly greater sheet shear (E_{sn}), which contributes to greater wall thinning, during diastolic filling in hypertrophy than in control. Fiber stretch: E_{ff} , sheet shortening: E_{ss} , MVO: mitral valve opening, ED: end diastole.

In contrast, sheet shear (E_{sn}) was enhanced at the subendocardial layer, resulting in a rightward shift of the time course (Figure 5-6B). These results suggest that enhanced ventricular filling in this model is achieved by enhanced shearing of the radially oriented laminar sheet structure which could contribute to wall thinning. Spotnitz *et al* (222) have elegantly demonstrated that motion of the sheets contributes importantly to wall thinning during volume increases in the heart and recent studies have shown predicted sheet motion in normal diastole in the open chest dog heart (230). The results in the present study indicate that factors that influence sheet motion may have important implications for ventricular function under pathologic conditions. Volume-overload hypertrophy is associated not only with myofiber lengthening and rearrangement but also with dramatic changes in the arrangements of ECM components (209). It has been demonstrated that this model of volume-overload is associated with no changes in collagen concentration (113), although the nature of the collagen crosslinks may be changed (113, 120). Thus it is speculated that the mechanism of a reduction in interlaminar stiffness may not be associated with a reduction in collagen amount but more likely a shift to a more compliant type III collagen or to disruption of interlaminar struts.

5.5.3 Limitations

A structural model for the myocardium was assumed that is based on the average fiber angle and the mode of the dominant sheet population at each layer. α and β were also measured at only one configuration in each animal in the fixed heart, and calculated angle changes based on deformation. Although the equations transforming strains from cardiac to fiber-sheet coordinates are exact (230), errors in measurement of strains (the spatial resolution of the biplane X-ray system is ~ 0.02 mm) or transposing the anatomic reference system from microscopic

measurements to the cardiac coordinate system *in vivo* may have been a source of variation. In addition, the data describe remodeling of myofibers and sheet structures in the LV anterior free wall. Regional variations should be taken into consideration when these results are extrapolated to other regions of the LV, such as the lateral, posterior wall and the septum. Lastly, the 3-D finite strains that we measured in anesthetized dogs may not accurately reflect the transmural mechanics in conscious animals.

5.6 Conclusions

Fiber strain and shearing deformation occur predominantly in the first third of diastolic filling period, and chronic volume overload induces remodeling in lengthening of the fiber and reorientation of the laminar sheet architecture. Sheet shear was significantly altered and delayed at the subendocardial layer during diastolic filling, whereas the magnitude of fiber stretch during diastolic filling is not altered in volume overload. These findings indicate that the enhanced filling associated with this model is achieved by enhanced sheet shear early in diastole. These results provide the first evidence that changes in the motion of radially oriented myolaminar sheets may play an important functional role in the pathology of diastolic dysfunction in this model of volume overload hypertrophy.

Chapter 6

Regional electromechanics

in normal heart

6.1 Abstract

Whether transmural mechanics could yield insight into the transmural electrical sequence was investigated. Although the concept of transmural dispersion of repolarization has helped explain a variety of arrhythmia, its presence *in vivo* is still disputable. The time course of transmural myofiber mechanics in the anterior LV of normal canine *in vivo* (n=14) was studied using transmural bead markers under biplane cineradiography. In four of these animals, plunge electrodes were placed in the myocardial tissue within the bead set to measure transmural electrical sequence. The onset of myofiber shortening was earliest at endocardial layers and progressively delayed toward epicardial layers ($P<0.001$), resulting in transmural dispersion of myofiber shortening (TDS_{short}) of 39msec. The onset of myofiber relaxation was earliest at epicardial layers, and most delayed at subendocardial layers ($P=0.004$), resulting in transmural dispersion of myofiber relaxation (TDR_{relax}) of 83msec. There was no significant transmural gradient in electrical repolarization ($P=n.s.$). In conclusion, despite lack of evidence of significant transmural gradient in electrical repolarization *in vivo*, there is transmural dispersion of myofiber relaxation as well as shortening.

6.2 Introduction

Over the past decade, the concept of transmural dispersion of repolarization (TDR_{repol}), or electrical heterogeneity, of the ventricular myocardium (7, 8) has provided a framework to understand normal and abnormal cardiac electrophysiology (9, 169, 217, 253, 254). Nevertheless, it is still unclear whether TDR_{repol} is present *in vivo*, where myocardial cells are electrically coupled (10). Some studies suggest that there is no significant TDR_{repol} in a healthy heart (126, 228).

Although the primary function of the heart is mechanical, little attention has been paid to mechanical correlation of TDR_{repol} (63), primarily because many studies of TDR_{repol} were performed *in vitro*, using wedge preparations of perfused ventricular myocardium. Measurements pertaining to mechanical function *in vivo* might yield insight into transmural electrical sequence. Earlier studies suggest the presence of transmural dispersion of myofiber shortening (22) as well as myofiber relaxation (17) *in vivo*.

To test the hypothesis that there is transmural dispersion of both myofiber shortening and relaxation, the time course of transmural myofiber mechanics was studied in the LV anterior wall of normal canine heart *in vivo* using transmurally implanted markers and biplane cineradiography with high spatiotemporal resolution.

6.3 Materials and Methods

All studies were performed according to the *Position of the American Heart Association on Research Animal Use*. All protocols were approved by the Animal Subjects Committee of the University of California, San Diego, which is accredited by the American Association for Accreditation of Laboratory Animal Care (AAALAC).

6.3.1 Experimental protocol

Adult mongrel dogs (n=14, 20-30 kg) were studied to measure the time course of transmural myofiber mechanics in the anterior LV *in vivo* during normal sinus rhythm or atrial pacing with pacing wires sutured on the left atrial (LA) surface. To measure 3-D transmural myofiber mechanics, under general anesthesia and median sternotomy, three transmural columns of four to six 0.8-mm-diameter markers and a 1.7-mm-diameter surface marker above each

column were placed within the anterior wall between the first (D_1) and the second diagonal branches (D_2) of the left anterior descending (LAD) coronary artery (Figure. 6-1) (17).

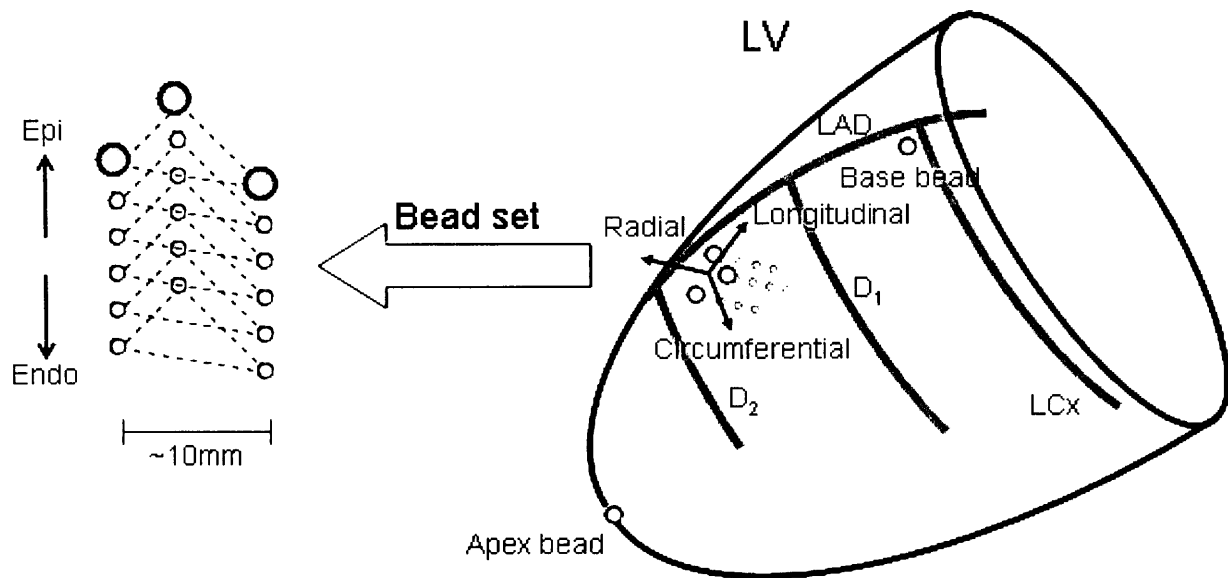


Figure 6-1. *Schematic representation of the heart.* The transmural bead set was implanted between the first (D_1) and the second (D_2) diagonal branch of the left anterior descending coronary artery (LAD) to measure finite deformation of the myocardial tissue across the wall. Epi, epicardium; Endo, endocardium; LV, left ventricle; LCx, left circumflex coronary artery.

To provide end-points for a LV long axis, 2-mm-diameter gold beads were sutured to the apical dimple (apex bead) and on the epicardium at the bifurcation of the LAD and LCx (base bead). To measure transmural electrical sequence (minimum sampling rate = 1 kHz), a subset of four of the 14 dogs were studied. For these four dogs, three pairs of bipolar plunge electrodes with terminal distance of 1-3 mm were inserted in subepicardial, midwall and subendocardial layers of the myocardial tissue within the bead set. The transmural location of the electrodes was histologically determined after euthanasia. Each animal was positioned in a biplane radiography system, and synchronous biplane cineradiographic images (125 frames/sec) of the bead markers were digitally acquired with mechanical ventilation suspended at end expiration. The LV pressure (LVP), central aortic pressure (AoP), LA pressure (LAP), surface and bipolar plunge ECGs were recorded simultaneously with the cineradiographic images. At the end of the study, the animal was euthanized with pentobarbital sodium and the heart perfusion-fixed with 2.5% buffered glutaraldehyde at the end-diastolic pressure measured in the study (17, 257). Because the heart was fixed at end-diastolic pressure, fiber orientations in the fixed hearts were assumed to represent the fiber structure in the end-diastolic reference configuration *in vivo* (17, 66, 230).

6.3.2 Histology

To avoid the distortional effects of dehydration and shrinkage associated with embedding, histological measurements were obtained using freshly fixed heart tissue. In the transmural block of tissue within the implanted bead set, the mean myofiber angle was measured with reference to the positive circumferential direction, and was determined from epicardium to endocardium at every 1-mm-thick section sliced parallel to the epicardial tangent plane (17, 66).

6.3.3 Data analysis

The time reference was defined as the peak R-wave on surface ECG for both mechanical and electrical data. The digital images from biplane X-ray were corrected for magnification and spherical distortion (17) to reconstruct the 3-D coordinates (158) of the bead markers. Continuous, nonhomogeneous transmural distributions of 3-D strains were computed for each frame as a deformed configuration with the peak R-wave on surface ECG as the reference state (66). The strain with respect to the local fiber coordinate, or fiber strain, was calculated from the strains and histologically measured myofiber angles at each depth. The strain time course was determined at 10 transmural layers: from 0% (epicardial surface) to 90% wall depth (subendocardium) by 10% increments. By convention in continuum mechanics, a negative strain represents shortening, whereas a positive strain represents stretch. The onset of myofiber shortening at each depth was defined as the time of peak positive strain. The onset of myofiber stretch, or myofiber relaxation, at each depth was defined as the time of peak negative strain. Transmural dispersion of myofiber shortening (TDS_{Short}) was defined as the transmural range of the onset of myofiber shortening. Transmural dispersion of myofiber relaxation (TDS_{Relax}) was defined as the transmural range of the onset of myofiber relaxation.

An established method of bipolar electrical analysis in the literature was followed, most recently used by Sengupta *et al* (216). Briefly, the electrical activation was defined as the first peak of the derivative of QRS in the regional bipolar deflection, and the electrical repolarization was defined as the steepest terminal phase of the T-wave of the bipolar electrocardiogram (11) (Figure 6-2). The same definition was applied when the T wave was inverted. A strong correlation exists between the activation-recovery intervals measured from the first order derivatives of QRS and T waves on the bipolar electrograms and the refractory periods and transmembrane action potential durations measured directly in cardiac tissues (108, 173).

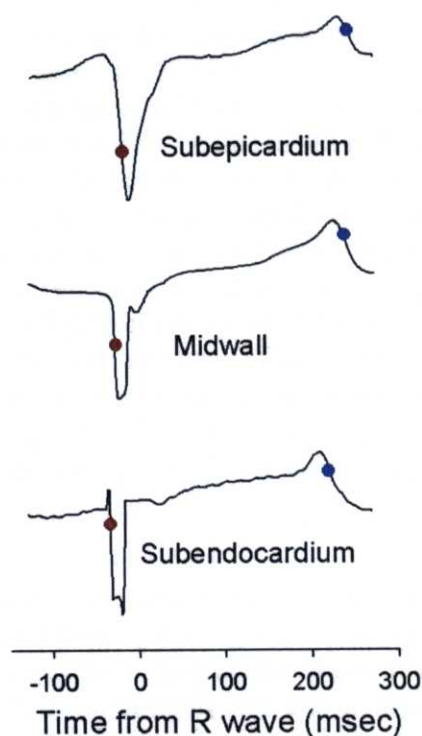


Figure 6-2. Bipolar electrograms from plunge electrodes. Red and blue dots mark the time points of steepest portion of initial bipolar QRS waveforms and end of T-wave, respectively. Note the endocardial-to-epicardial direction of depolarization, whereas no clear transmural dispersion of repolarization is observed.

6.3.4 Statistical analysis

Values are means \pm SD. To make the study comparable to previous similar studies (56, 126), a sample size of 14 dogs was chosen for the mechanical data and a sample size of four dogs was chosen for the electrical data. One-way repeated-measures analysis of variance (RMANOVA) was used to assess the effect of wall depth on the onset of shortening, relaxation, electrical activation and repolarization. For the mechanical data, a paired t-test was used to compare the two transmural ends, i.e., 0% vs. 90% wall depth. For the electrical data, a paired t-test was used to compare the subendocardial layer to the subepicardial layer. For both the mechanical and the electrical data, ordinary linear regression was used to obtain an unbiased estimate of the absolute value of the slope of wall depth as a function of the time from the ECG R wave. Statistical significance was accepted at $P < 0.05$. Statistics were performed using SigmaStat 3.0 (SPSS, Inc. Chicago, IL).

6.4 Results

The site of fiber strain measurement was located 55 ± 18 % of the distance from base to apex along the LV long axis, in a region of the anterior LV free wall 1-2 cm septal of the anterolateral papillary muscle. Mean wall thickness at the measurement site was 12 ± 3 mm. Hemodynamic parameters are summarized in Table 6-1.

Parameter	Value
Cycle Length (msec)	632 ± 119
LVP _{max} (mmHg)	100 ± 13
dP/dt _{max} (mmHg/sec)	$2,187 \pm 443$
dP/dt _{min} (mmHg/sec)	$-2,082 \pm 426$

Table 6-1. *Hemodynamic parameters*. Values are mean \pm SD (n=14). LVP_{max}, maximum left ventricular pressure; dP/dt, first derivative of pressure over time; dP/dt_{max}, peak positive dP/dt; dP/dt_{min}, peak negative dP/dt.

6.4.1 Fiber orientation

The transmural fiber orientation (Figure 6-3) was consistent among all the animals studied. The mean fiber angles ranged approximately from -60° to $+60^\circ$, from epicardium to endocardium, respectively, resulting in a transmural gradient of approximately 120° .

6.4.2 Myofiber mechanics

The onset of myofiber shortening typically occurred earlier in endocardium than epicardium (Figure 6-4). The delay of myofiber shortening at epicardial layers resulted from a brief period of myofiber stretch (= prestretch) that preceded myofiber shortening (Figure 6-4A). Myofiber shortening (Figure 6-5, open circles) started earliest at a subendocardial layer (90% wall depth, 6 ± 13 msec), and was progressively delayed toward the epicardium ($P < 0.001$ by RMANOVA). There was a significant transmural gradient in the onset of myofiber shortening ($P = 0.003$, 0% wall depth, 46 ± 42 msec vs. 90% wall depth by the paired t-test). The mean TDS_{short} was 39 msec. Linear regression of the onset of myofiber shortening at each depth indicates that the mean propagation velocity of myofiber shortening from endocardium to epicardium was 0.25 m/s (Figure 6-6, open circles).

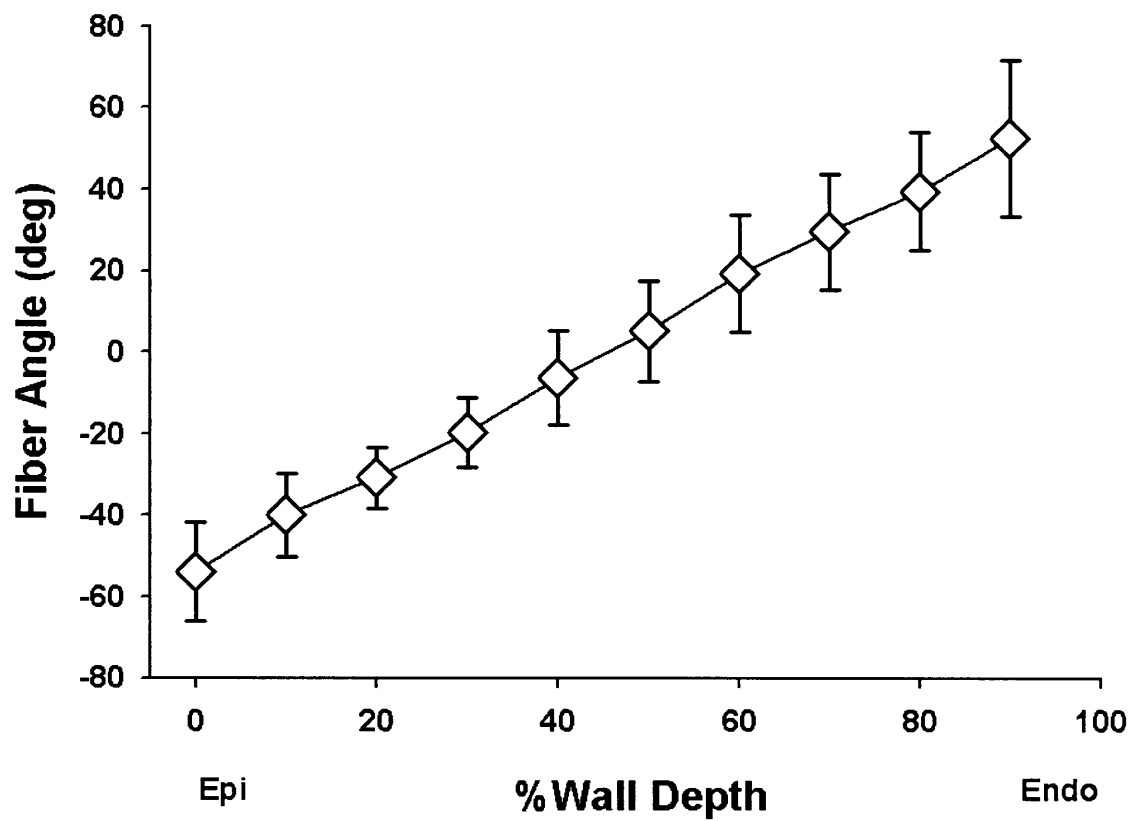


Figure 6-3. *Transmurial fiber orientation.* Values are mean \pm SD (n=14). Fiber angles were measured with reference to the positive circumferential direction. Epi, epicardium; Endo, endocardium.

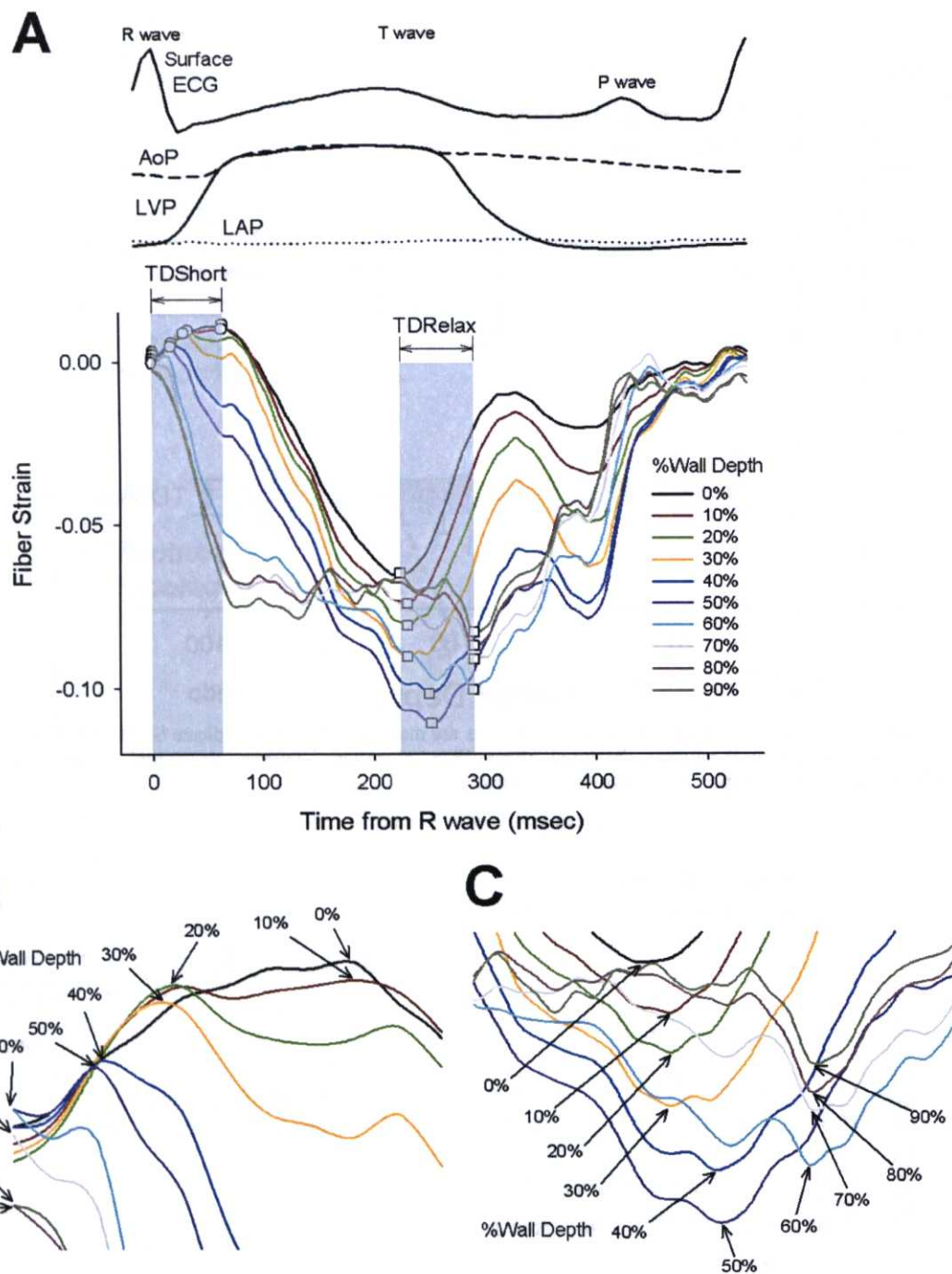


Figure 6-4. Time course of transmural fiber strains. A. Entire cardiac cycle. Different colors represent the percent wall depth from the epicardial surface. Open circles, the onset of myofiber shortening; open squares, the onset of myofiber relaxation; TDSHORT, transmural dispersion of myofiber shortening; TDRRELAX, transmural dispersion of myofiber relaxation; ECG, electrocardiogram; AoP, central aortic pressure; LVP, left ventricular pressure; LAP, left atrial pressure. B. A closer look at TDSHORT. C. A closer look at TDRRELAX.

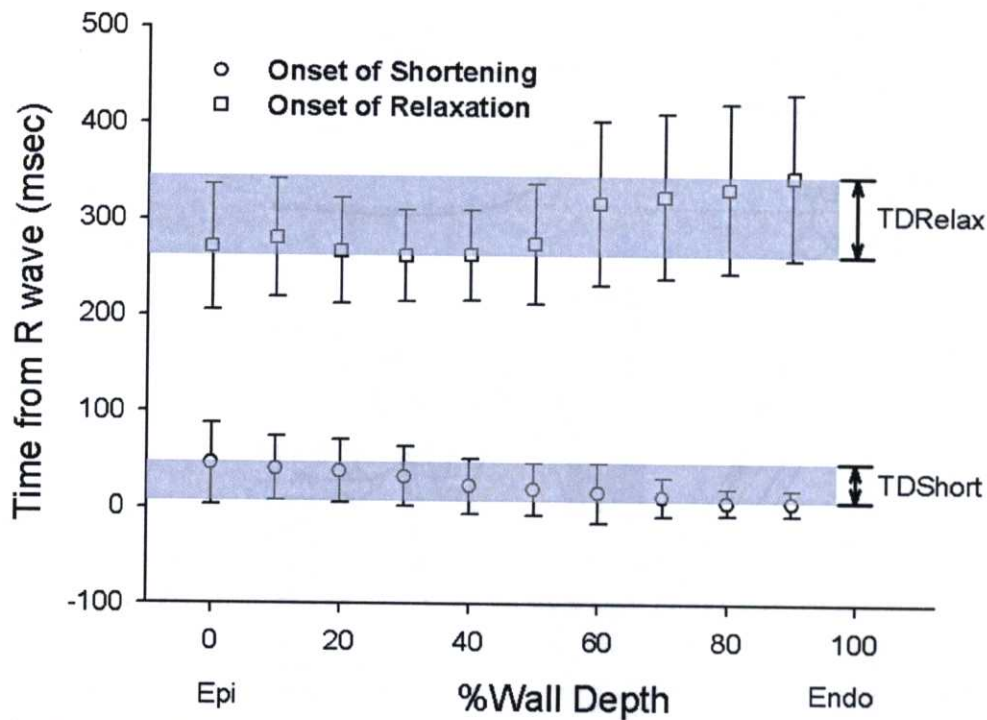


Figure 6-5. *Transmural dispersion of myofiber mechanics.* Values are mean and error bars indicate SD (n=14). Open circles, the onset of myofiber shortening; open squares, the onset of myofiber relaxation; TDShort, transmural dispersion of myofiber shortening; TDRelax, transmural dispersion of myofiber relaxation.

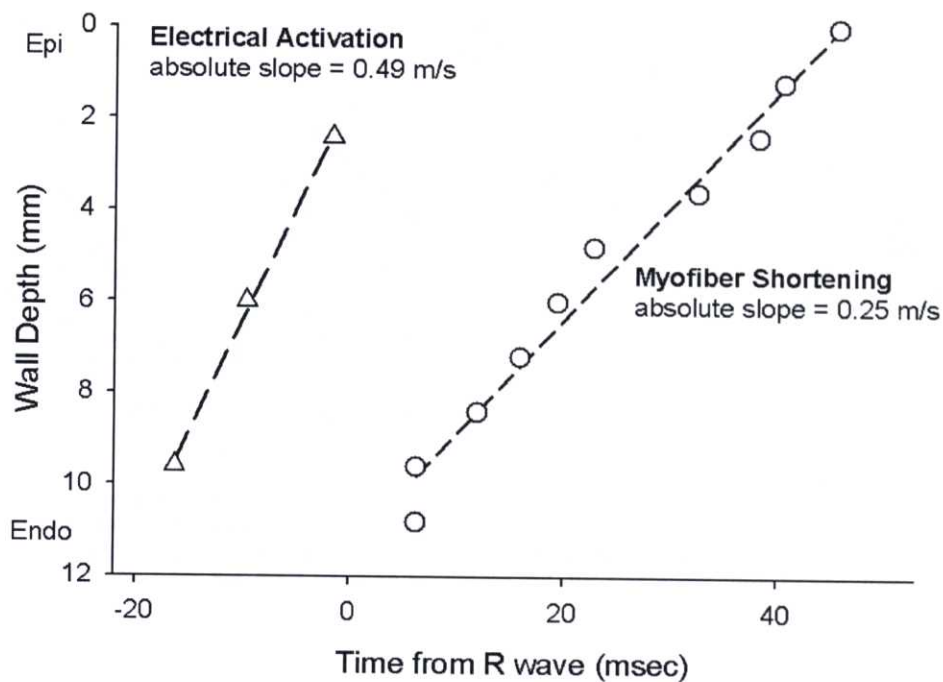


Figure 6-6. *Electrical activation (open triangles) and the onset of myofiber shortening (open circles) vs. mean wall depth.* The open triangles represent the electrical activation (n=4) mean value at each depth (mm). The open circles represent the onset of myofiber shortening (n=14) mean value at each depth (mm).

In contrast, the onset of myofiber relaxation typically occurred earlier in epicardium than endocardium (Figure 6-4C). The onset of myofiber relaxation (Figure 6-5, open squares) was earliest at a subepicardial layer (30% wall depth, 262 ± 48 msec), and was progressively delayed toward the endocardium ($P=0.004$ by RMANOVA). There was a significant transmural gradient in the onset of myofiber relaxation ($P<0.001$, 0% wall depth, 271 ± 65 msec vs. 90% wall depth, 345 ± 86 msec by the paired t-test). The mean TDRelax was 83 msec. Linear regression of the onset of myofiber relaxation at each depth indicates that the mean propagation velocity of myofiber relaxation from epicardium to endocardium was 0.10 m/s (Figure 6-7, open squares); however, the relationship was not as linear as that for myofiber shortening. Of note, a second peak of myofiber shortening was observed at several layers in 8 animals during diastolic filling that was smaller in magnitude than the initial peak shortening. This second peak is also observed in epicardial layers (0-50%) in Figure 6-4.

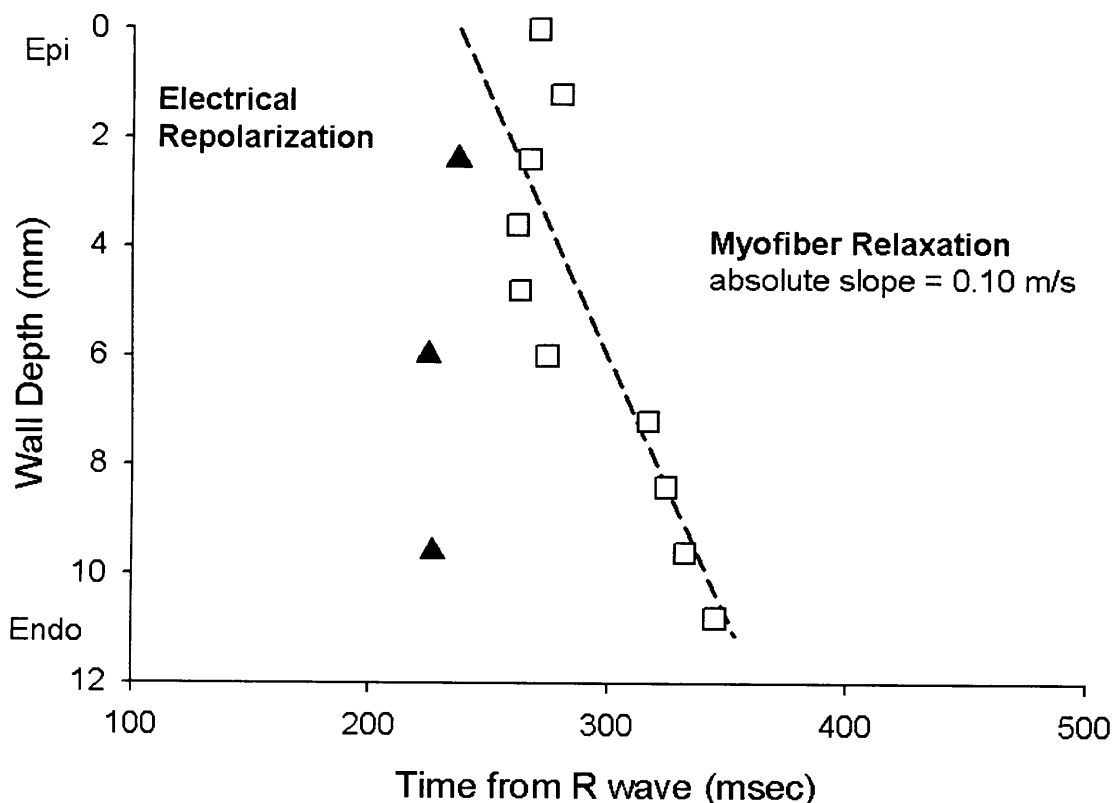


Figure 6-7. Electrical repolarization (closed triangles) and the onset of myofiber relaxation (open squares) vs. mean wall depth. The closed triangles represent the electrical repolarization ($n=4$) mean value at each depth (mm). The open squares represent the onset of myofiber shortening ($n=14$ mean value at each depth (mm)).

6.4.3 Bipolar electrical recordings

There was a significant transmural gradient in electrical activation ($P=0.035$ by RMANOVA, Figure 6-6); activation at subepicardium was significantly delayed compared with that of subendocardium ($P=0.029$ by the paired t-test). Linear regression of electrical activation indicates that the mean electrical conduction velocity from endocardium to epicardium was 0.49 m/s (Figure 6-6, open triangles). Electrical repolarization at subendocardial, midwall and subepicardial layers was almost synchronous (227 ± 38 , 225 ± 58 , and 237 ± 41 msec, respectively),

and there was no significant transmural gradient ($P=n.s.$ by both RMANOVA and the paired t-test) (Figure 6-7, closed triangles).

6.5 Discussion

Although heterogeneity of the onset of shortening and relaxation between subendocardium and subepicardium has been studied (104, 205, 215), this is the first study to comprehensively examine the depth-dependent difference of myofiber mechanics *in vivo*. The results demonstrate that myofiber mechanics is transmurally and temporally heterogeneous, and global events such as LV end diastole and end systole do not uniquely correlate with the regional myofiber mechanics at individual depths.

6.5.1 Transmural sequence of electrical activation and myofiber shortening

The mean electrical conduction velocity (0.49 m/s, Figure 6-6) was consistent with reported values for transmural conduction velocity (195, 196). Because the transmural propagation velocity of myofiber shortening (0.25 m/s) was slower than the electrical conduction velocity (0.49 m/s), the electromechanical delay was longer in epicardium than in endocardium. This *in vivo* finding is contrary to derivations from finite element simulation (105) and *in vitro* studies (63). One explanation for this new observation is tissue tethering (167, 215). Because myofibers are physically coupled, myofiber mechanics at one layer might induce complex interactions within and between the layers, alter loading conditions, and thus make epicardial myofibers shorten later than they would *in vitro*. Such tissue interactions can be seen in the relationship between the fiber and cross-fiber strains at epicardial and endocardial layers (Figure 6-8). Overall, epicardial fiber strain (solid purple line) and endocardial cross-fiber strain (broken green line) demonstrate a similar time course. Likewise, epicardial cross-fiber strain (broken purple line) and endocardial fiber strain (solid green line) demonstrate a similar time course. During isovolumic periods, fiber and cross-fiber strains in the same layer were always in opposite directions. For example, during isovolumic contraction (IVC), the epicardial myocardium stretched in the fiber direction (blue arrow, solid purple line), but shortened in the cross-fiber direction (red arrow, broken purple line). Similarly, during isovolumic relaxation (IVR), the endocardial myocardium shortened then stretched in the fiber direction (red arrow, solid green line), while it stretched then shortened in the cross-fiber direction (blue arrow, broken green line). These findings are consistent with previous reports (104, 205, 215).

Previous studies imply that the transmural sequence of the fiber mechanics of the apical and the basal regions of the anterior LV may be in the opposite directions (43, 216). However, the piezoelectric crystal pairs in these studies were not placed directly along the fiber direction. Therefore, these studies did not specifically examine the time course of true fiber strains, and are fundamentally different from this study.

6.5.2 Transmural sequence of electrical repolarization and myofiber relaxation

No significant transmural gradient of electrical repolarization in the mid-anterior LV was found *in vivo*, which is consistent with earlier studies in canine (11, 126), swine (216) and human (54, 228, 229). El-Sherif *et al* (81) found that activation-recovery interval (ARI) in canine *in vivo* was significantly longer at midmyocardium than epicardium and endocardium at longer cycle lengths, but transmural gradient was not significant at the range of cycle length in the study (600-

700 msec). Of note, electrical repolarization was later in subepicardium than subendocardium (Figure 6-6), although the difference was not significant. This finding, although contradictory to *in vitro* reports, has been previously documented (89, 216).

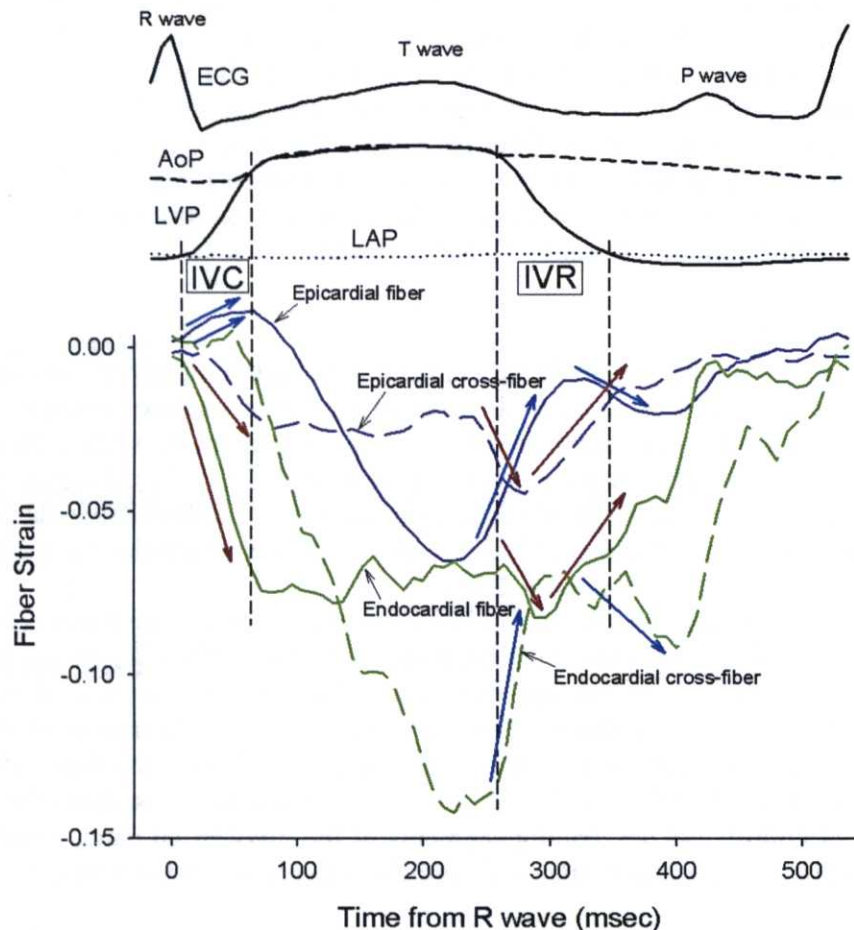


Figure 6-8. *Transmural tissue coupling.* Purple and green lines indicate strains in epicardial (0% wall depth) and endocardial (90% wall depth) layers, respectively. Solid and broken lines indicate fiber and cross-fiber strains, respectively. IVC, isovolumic contraction; IVR, isovolumic relaxation.

Despite lack of significant transmural gradient in electrical repolarization *in vivo*, the data indicate that there is a significant gradient in the onset of myofiber relaxation, which is progressively delayed in endocardial layers. This transmural sequence of myofiber relaxation is consistent with the reported data from isolated canine LV myocytes (63). This mechanical relaxation sequence is clearly different from the electrical repolarization sequence, and requires exploration of possible mechanisms.

One possible explanation is that TDRelax is a direct consequence of TDRepol; that is, transmural electrical repolarization sequence has a significant impact on mechanical relaxation of the ventricle. TDRepol may exist *in vivo*, and the reported lack of it may simply reflect technical difficulties associated with obtaining transmural electrical measurements. For example, Van Dam and Durrer (236, 237) noted that the spatial and temporal sequence of repolarization cannot be adequately studied by measuring the steepest portion of the T wave, using either bipolar or unipolar electrodes, because repolarization occurs much more slowly and is of lower voltage than depolarization. To overcome this limitation, Spach and Barr (221) measured potential distributions in closed-chest canine *in vivo*, and found that repolarization was earlier in

epicardium than endocardium. This result was consistent with refractory period measurements of Burgess *et al* (45).

Another explanation is that TDRelax results from mechanical interactions between each myofiber and its loading conditions. Myofiber relaxation *in vivo* is primarily determined by the balance between the loading conditions and generated force within the myofiber during diastole; myofiber relaxation occurs when the afterload overcomes the generated force of the myofiber. The delay of endocardial relaxation may be explained by the fact that the end-systolic fiber stress is highest at endocardium (105). Moreover, the transmural propagation velocity of myofiber relaxation was even smaller than that of myofiber shortening (0.10 vs. 0.25 m/s, respectively). This very slow transmural propagation velocity suggests that TDRelax may be of mechanical origin, rather than electrical. Both of these possible explanations are not mutually exclusive, and both may be in effect, at least partially, to cause TDRelax *in vivo*.

6.5.3 Clinical implications

The present study highlights a gap in our clinical understanding of electromechanical sequence in a normal heart, which was uncovered by recent studies on cardiac resynchronization therapy (87, 148). The results are consistent with recent reports presenting similar shortening-relaxation kinematics of the epicardial and endocardial layers (205, 215, 216). Delayed onset of relaxation is routinely encountered as a physiological phenomenon in normal humans and has been referred to as post-systolic shortening (241, 271), and experimental studies have confirmed endocardial shortening after aortic valve closure (216).

There has been a great clinical interest in the myocardial band hypothesis (44, 233), which has important surgical implications. This controversial hypothesis (242) is criticized as being oversimplified and having no anatomical foundation (68), and the anatomical data from this study also do not fit with this hypothesis. For example, the smooth transition of myofiber orientation from epicardium to endocardium in the mid-anterior LV (Figure 6-3), which are consistent with a number of published data (17, 65, 107, 150, 225), does not support the concept that there are discrete ascending and descending segments of the myocardial band, which would likely produce a more sudden change of transmural myofiber orientation in the midwall.

6.5.4 Limitations

The measurements were restricted to the mid-anterior LV, thus the findings may not be applicable to other regions of LV. It is possible that the electrical and mechanical measurements may have been affected by anesthetics and epicardial cooling associated with open-chest preparations. Some of the findings may have been affected by the damage caused by the bead implantation (57). However, measurements from noninvasive techniques such as MRI have shown similar transmural gradients in regional strains (37), thus the technique does not substantially affect the local mechanics.

6.6 Conclusions

There is transmural dispersion in the onset of myofiber relaxation as well as shortening *in vivo*, despite lack of evidence of significant transmural gradient in electrical repolarization.

Chapter 7

Regional electromechanics

in paced heart

7.1 Abstract

LV epicardial pacing acutely reduces wall thickening at the pacing site. Because LV epicardial pacing also reduces transverse shear deformation, which is related to myocardial sheet shear, it was hypothesized that impaired end-systolic wall thickening at the pacing site is due to reduction in myocardial sheet shear deformation, resulting in a reduced contribution of sheet shear to wall thickening. It was also hypothesized that epicardial pacing would reverse transmural mechanical activation sequence, and thereby mitigate normal transmural deformation. To test these hypotheses, the effects of LV epicardial pacing on transmural fiber-sheet mechanics were investigated by determining 3-D finite deformation during normal atrioventricular (AV) conduction and LV epicardial pacing in the anterior wall of normal dog hearts *in vivo*. The measurements indicate that impaired end-systolic wall thickening at the pacing site was not due to selective reduction of sheet shear, but rather resulted from overall depression of fiber-sheet deformation, and relative contributions of sheet strains to wall thickening were maintained. These findings suggest lack of effective end-systolic myocardial deformation at the pacing site, most likely because the pacing site initiates contraction significantly earlier than the rest of the ventricle. Epicardial pacing also induced reversal of the transmural mechanical activation sequence, which depressed sheet extension and wall thickening early in the cardiac cycle, whereas transverse shear and sheet shear deformation were not affected. These findings suggest that normal sheet extension and wall thickening immediately following activation may require normal transmural activation sequence, while sheet shear deformation may be determined by local anatomy.

7.2 Introduction

Cardiac resynchronization therapy (CRT) has proven to be effective in improving cardiac function in moderate-to-severe heart failure associated with an intraventricular conduction delay, most commonly of a left bundle branch block (LBBB) type (23, 35, 52, 133, 147, 187, 214). The advent of CRT has resulted in increasingly frequent use of left ventricular (LV) epicardial pacing in clinical settings. Despite clinical benefits of CRT, LV epicardial pacing is associated with detrimental effects on normal transmural function. Systolic wall thickening, which is an important component of regional cardiac function, is significantly reduced at the pacing site (244). Furthermore, LV epicardial pacing reverses the normal activation sequence of transmural depolarization into the epicardial-endocardial propagation (87, 92, 155), which significantly increases QT interval and transmural dispersion of repolarization (TDR), and enhances susceptibility to torsade de pointes (TdP) in a subset of patients (76, 169). To design more effective and safe pacing therapies, it is of critical importance to understand the effects of epicardial pacing on normal transmural function.

Several lines of evidence support the concept that transverse shear deformation is required for normal systolic wall thickening (150, 151, 222). Because the LV myocardium consists of helically woven myofibers (188, 225) that are arranged in transversely oriented myocardial sheets (150), transverse shear deformation is anatomically related to myocardial sheet shear, and sheet shear deformation contributes significantly to normal systolic wall thickening (66). Because LV epicardial pacing significantly reduces transverse shear deformation (244), it was hypothesized that impaired end-systolic wall thickening at the epicardial pacing site is due to reduction in myocardial sheet shear deformation, resulting in a reduced contribution of sheet shear to wall thickening. It was also hypothesized that LV epicardial pacing would reverse transmural mechanical activation sequence, and thereby mitigate normal transmural deformation. To test these hypotheses, the effects of LV epicardial pacing on

transmural fiber-sheet mechanics were investigated by determining 3-D finite deformation during normal atrioventricular (AV) conduction and LV epicardial pacing in the anterior wall of normal dog hearts *in vivo*. The measurements indicate that impaired end-systolic wall thickening at the epicardial pacing site was not due to selective reduction of sheet shear, but rather resulted from overall depression of fiber-sheet deformation, and relative contributions of sheet strains to wall thickening were maintained. Epicardial pacing also induced reversal of the transmural mechanical activation sequence, which significantly depressed sheet extension and wall thickening early in the cardiac cycle, whereas transverse shear and sheet shear deformation were not affected.

7.3 Materials and Methods

All animal studies were performed according to the NIH guidelines for the care and use of laboratory animals in research. All protocols were approved by the Animal Subjects Committee of the University of California, San Diego, which is accredited by the American Association for Accreditation of Laboratory Animal Care. A subset of data from the five animals included in this study has been presented previously (17), which described local ventricular deformation during early relaxation under normal AV conduction.

7.3.1 Experimental protocol

The protocol for surgical preparation was described in detail previously (17). Briefly, five adult mongrel dogs (19-28 kg) underwent median sternotomy under general anesthesia, with the LV pressure, central aortic pressure and the surface ECG monitored throughout the study. Low-dose dopamine (2.5-5.0 $\mu\text{g/kg/min}$) was administered intravenously to maintain blood pressure in 2 animals. To measure 3-D myocardial deformation, three transmural columns of four to six 0.8-mm-diameter gold beads and a 1.7-mm-diameter surface gold bead above each column were placed within the anterior wall between the first (D_1) and the second diagonal branches (D_2) of LAD (Figure 7-1A). To provide end-points for a LV long axis, 2-mm-diameter gold beads were sutured to the apical dimple (apex bead, Figure 8-1A) and on the epicardium at the bifurcation of LAD and LCx (base bead, Figure 7-1A). Pacing wire pairs were sutured to the LA and the LV epicardial surface across the triangle of the surface gold beads (Figure 7-1A). Atrial pacing was performed by stimulating LA electrodes, and LV epicardial pacing was performed by stimulating both LA and LV electrodes (LA-LV delay = 20-40 ms), via a square-wave, constant-voltage electronic stimulator at a frequency 20% above baseline heart rate to suppress native sinus rhythm. Stimulation parameters (voltage 10% above threshold, duration 8 ms, and frequency) were kept constant in each animal. Each animal was positioned in a biplane radiography system, and synchronous biplane cineradiographic images (125 frames/sec) of the bead markers were digitally acquired with mechanical ventilation suspended at end expiration. Image acquisition for the two pacing modes (atrial pacing and LV epicardial pacing) was performed consecutively at the same heart rate to minimize variation in hemodynamic conditions. At the end of the study, the animal was euthanized with pentobarbital sodium and the heart perfusion-fixed with 2.5% buffered glutaraldehyde at the end-diastolic pressure measured in the study (17, 257). Because the heart was fixed at end-diastolic pressure, fiber and sheet orientations in the fixed hearts were assumed to represent the fiber-sheet structure in the end-diastolic reference configuration *in vivo* (17, 66, 230).

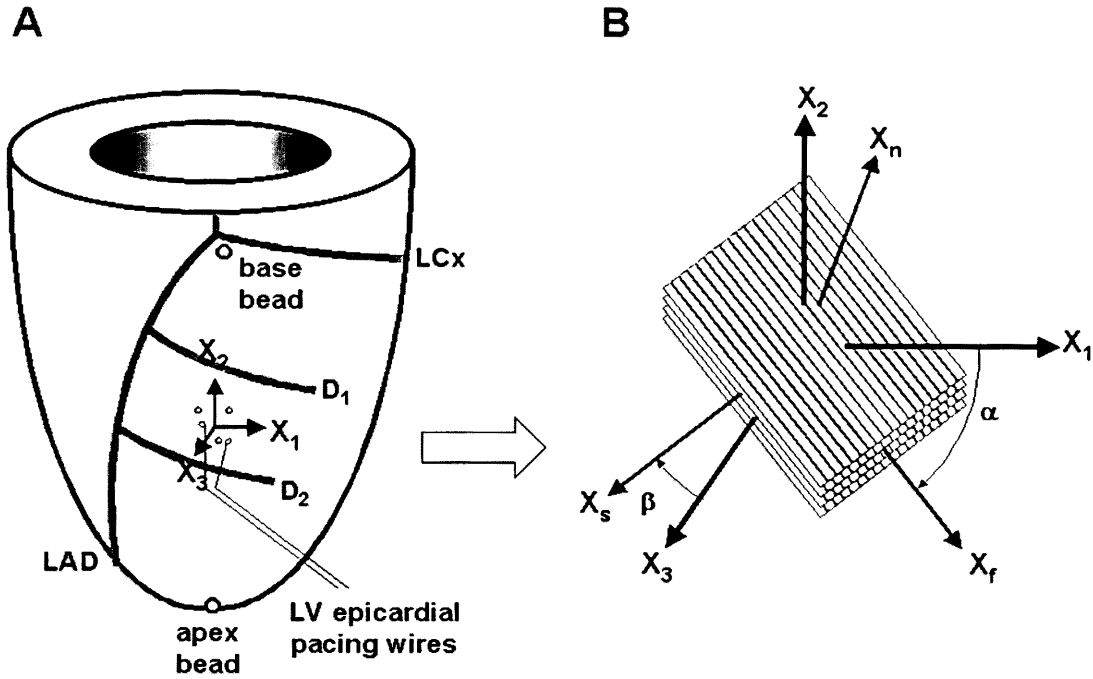


Figure 7-1: A: Schematic representation of the left ventricle. X_1 : circumferential axis, X_2 : longitudinal axis, X_3 : radial axis, LAD: left anterior descending coronary artery, D_1 , D_2 : first and second diagonal branch of LAD, respectively. B: Schematic representation of local fiber-sheet axes. Fiber angle (α) was measured in the circumferential-longitudinal (X_1 - X_2) plane at each wall depth with reference to the positive circumferential axis (X_1). Sheet angle (β) was measured in the plane perpendicular to the fiber angle at each wall depth with reference to the radial axis (X_3). X_f : fiber axis, X_s : sheet axis, X_n : axis oriented normal to the sheet plane. The X_f , X_s , and X_n axes present a Cartesian system.

To avoid the distortional effects of dehydration and shrinkage associated with embedding, histological measurements were obtained using freshly fixed heart tissue. In the transmural block of tissue within the implanted bead set, the mean fiber (α) and sheet angles (β) were determined from epicardium to endocardium at every 1-mm-thick section sliced parallel to the epicardial tangent plane (Figure 7-1B) (17, 66). The digital images from biplane X-ray were spherically corrected (17) to reconstruct the 3-D coordinates (158) of the gold bead markers. Continuous, nonhomogeneous transmural distributions of 3-D finite strains were computed (17). Six independent finite strains (E_{11} , E_{22} , E_{33} , E_{12} , E_{23} and E_{13}) were computed in the local cardiac coordinate system (X_1 , X_2 , X_3) (172), which were subsequently used to compute another set of six finite strains (E_{ff} , E_{ss} , E_{nn} , E_{fs} , E_{sn} and E_{fn}) in the local fiber-sheet coordinate system (X_f , X_s , X_n) (65) through an orthogonal transformation to convert the strain tensor using α and β at each depth. Finite strains were calculated for each frame (125 frames/sec) as a deformed configuration with end-diastole as the reference state at three wall depths: 25% (subepicardium), 50% (midwall) and 75% (subendocardium) wall depth from the epicardial surface. End-diastole was defined as the time of the peak of the ECG R-wave for atrial pacing and the V-spike for LV epicardial pacing. The V-spike was chosen rather than the peak of R-wave as the reference state for LV epicardial pacing, because the former reflects the timing of the activation of the pacing

site, as opposed to the latter that represents the timing of activation of the whole ventricle. End-systole was derived from the nadir of the dicrotic notch of the central aortic pressure.

Three phases were defined in the cardiac cycle: early contraction (EC) phase (beginning at end-diastole and ending at dP/dt_{\max}), ejection phase (beginning at dP/dt_{\max} and ending at end-systole), and early relaxation (ER) phase (beginning at end-systole and ending at minimum LV pressure) (17, 130) (Figure 7-2). The QT interval was defined as the time interval between the initial deflection of the QRS complex and the point at which a tangent drawn to the steepest portion of the terminal part of the T wave crossed the isoelectric line (169). Corrected QT (QTc) was calculated using Bazett's formula (31). TDR was defined as the interval between the peak to the end of the T wave ($T_{\text{peak-end}}$) on the surface ECG (9, 254).

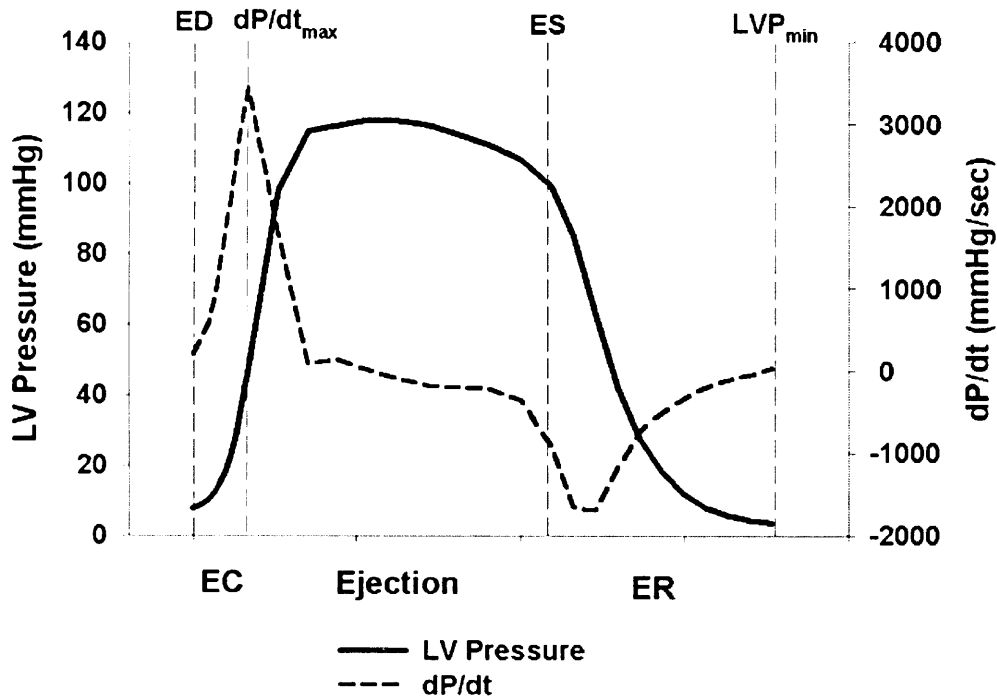


Figure 7-2: Three cardiac phases. EC: early contraction phase, Ejection: ejection phase, ER: early relaxation phase, ED: end-diastole, ES: end-systole, LVP_{\min} : minimum LV pressure.

To assess the fiber-sheet mechanics of impaired wall thickening (E_{33}) during epicardial pacing, the contribution of each term on the right-hand side of the following equation was investigated (66).

$$E_{33} = 2E_{sn} \sin \beta \cos \beta + E_{ss} \cos^2 \beta + E_{nn} \sin^2 \beta \quad (7-1)$$

It is evident from Eq. 7-1 that in terms of fiber-sheet coordinates, wall thickening (E_{33}) depends only on the sheet angle (β) and the fiber-sheet strain components in the (X_s, X_n) plane normal to the local fiber axis, namely E_{sn} , E_{ss} and E_{nn} (66).

To assess transmural mechanical activation sequence with both pacing modes, *mechanical activation time* (t_m) was defined as the time to reach 10% of the maximum fiber strain (E_{ff}) at each transmural depth. To evaluate the effect of reversed transmural mechanical activation sequence on transmural deformation, *transmural mechanical activation strains* (E') were defined in both the local cardiac and fiber-sheet coordinate system. With atrial pacing, the reference configuration was mechanical activation time at subendocardium ($t_{m\text{ENDO}}$) and the

deformed configuration was mechanical activation time at subepicardium (t_{mEPI}). Conversely, with epicardial pacing, the reference configuration was t_{mEPI} and the deformed configuration was t_{mENDO} . Because transmural mechanical activation sequence propagates from subendocardium to subepicardium with atrial pacing, and from subepicardium to subendocardium with epicardial pacing (See Results), E' strains describe mean transmural myocardial deformation when mechanical activation travels between subendocardium and subepicardium.

7.3.2 Statistical analysis

Values are means \pm SE unless otherwise specified. A paired t-test was used to compare atrial pacing and LV epicardial pacing for global hemodynamic parameters, time intervals, and each strain component. Two-factor repeated measures ANOVA was used for the time course analysis, with the effects of pacing mode (atrial vs. LV epicardial pacing) and time on each strain component determined at three depths (subepicardium, midwall and subendocardium) individually. Statistics were performed using SigmaStat 3.0 (SPSS, Inc. Chicago, IL). Statistical significance was accepted at $P \leq 0.05$.

7.4 Results

Anatomic measurements for these five animals were described previously (17). Briefly, the mean fiber angle ranged approximately from -60° (epicardium) to $+60^\circ$ (endocardium). The mean sheet angle was predominantly negative with smaller variations across the wall (-36° to -2°). The centroid of the bead set was 65 ± 1 % of the distance from base bead to apex bead, in the anterior LV free wall $1 \sim 1.5$ cm lateral from the LAD. Mean wall thickness at the bead set location was 10 ± 1 mm, and the deepest bead was located at 91 ± 2 % wall depth. Global parameters are summarized in Table 7-1.

	Atrial pace	Epicardial pace
Heart rate (bpm)	133 ± 12	133 ± 12
Peak LV pressure (mmHg)	119 ± 9	$109 \pm 10^*$
dP/dt_{max} (mmHg/sec)	3436 ± 858	$2754 \pm 791^*$
dP/dt_{min} (mmHg/sec)	-2105 ± 325	-1680 ± 219
LVEDP (mmHg)	8 ± 2	5 ± 1
LVESP (mmHg)	99 ± 6	89 ± 7
Tau (msec)	23 ± 5	$25 \pm 5^*$
Early contraction (ms)	34 ± 5	$102 \pm 14^*$
Ejection (ms)	186 ± 34	174 ± 23
Early relaxation (ms)	134 ± 15	138 ± 15
ED-ES (ms)	219 ± 35	$277 \pm 36^*$
QT (ms)	204 ± 16	$248 \pm 16^*$
QTc (ms)	446 ± 36	$539 \pm 21^*$
TDR (ms)	30 ± 3	$63 \pm 10^*$

Table 7-1: Hemodynamic parameters and time intervals. Values are means \pm SE (n=5). LV: left ventricle, dP/dt_{max} : peak positive dP/dt , dP/dt_{min} : peak negative dP/dt , EDP: end-diastolic pressure, ESP: end-systolic pressure, Tau: the time constant of LV isovolumic pressure decay (logarithmic method) (197, 247), ED-ES: time interval from end-diastole (ED) to end-systole (ES), QT: QT interval on surface ECG, QTc: corrected QT interval, TDR: transmural dispersion of repolarization. * $P < 0.05$ vs. atrial pacing.

7.4.1 End-systolic wall thickening and fiber-sheet strains during epicardial pacing

Epicardial pacing significantly reduced wall thickening (E_{33}) and transverse shear (E_{23} , E_{13}) ($P < 0.05$, Table 7-2). Epicardial pacing also depressed all the fiber-sheet strains, and all the terms on the right-hand side of Eq. 7-1 ($2E_{sn} \sin \beta \cos \beta$, $E_{ss} \cos^2 \beta$, and $E_{nn} \sin^2 \beta$). As a result, the relative contribution of each term to wall thickening ($2E_{sn} \sin \beta \cos \beta / E_{33}$, $E_{ss} \cos^2 \beta / E_{33}$, and $E_{nn} \sin^2 \beta / E_{33}$) was not significantly affected by epicardial pacing ($P = \text{NS}$).

	Atrial pace	Epicardial pace
E_{11}	-0.154 ± 0.019	$-0.060 \pm 0.016^*$
E_{22}	-0.043 ± 0.009	-0.027 ± 0.012
E_{33}	0.235 ± 0.032	$0.085 \pm 0.023^*$
E_{12}	0.030 ± 0.006	0.027 ± 0.005
E_{23}	0.066 ± 0.014	$0.018 \pm 0.012^*$
E_{13}	0.067 ± 0.009	$0.040 \pm 0.009^*$
E_{ff}	-0.118 ± 0.010	$-0.040 \pm 0.015^*$
E_{ss}	0.121 ± 0.024	$0.034 \pm 0.014^*$
E_{nn}	0.036 ± 0.027	$0.004 \pm 0.015^*$
E_{fs}	0.065 ± 0.015	$0.028 \pm 0.012^*$
E_{sn}	-0.078 ± 0.038	$-0.026 \pm 0.022^*$
E_{fn}	-0.055 ± 0.013	$-0.031 \pm 0.010^*$
$E_{ss} \cos^2 \beta$	0.096 ± 0.021	$0.028 \pm 0.011^*$
$E_{nn} \sin^2 \beta$	0.020 ± 0.010	$0.008 \pm 0.006^*$
$2E_{sn} \sin \beta \cos \beta$	0.119 ± 0.020	$0.049 \pm 0.016^*$
$\frac{E_{ss} \cos^2 \beta}{E_{33}}$	0.438 ± 0.070	0.333 ± 0.091
$\frac{E_{nn} \sin^2 \beta}{E_{33}}$	0.082 ± 0.038	0.043 ± 0.063
$\frac{2E_{sn} \sin \beta \cos \beta}{E_{33}}$	0.481 ± 0.047	0.631 ± 0.077

Table 7-2: End-systolic strains. Values are transmural average (subepicardium, midwall and subendocardium) \pm SE ($n=5$). E_{11} : circumferential strain, E_{22} : longitudinal strain, E_{33} : radial strain, E_{12} : circumferential-longitudinal shear strain, E_{23} : longitudinal-radial shear strain, E_{13} : circumferential-radial shear strain, E_{ff} : fiber strain, E_{ss} : sheet strain, E_{nn} : strain normal to the sheet plane, E_{fs} : shear strain within the sheet plane, E_{sn} : sheet shear strain, E_{fn} : fiber-normal shear strain, β : sheet angle, *: $P < 0.05$ vs. Atrial pace.

With either atrial or epicardial pacing, the relative contribution of the sheet shear term ($2E_{sn} \sin \beta \cos \beta$), sheet extension term ($E_{ss} \cos^2 \beta$), and sheet thickening term ($E_{nn} \sin^2 \beta$) was fixed at 48-63%, 33-44%, and 4-8%, respectively.

7.4.2 Time course of finite strains at the pacing site

With atrial pacing, most strain components underwent a simple contraction-relaxation pattern with the peak deformation near end-systole, reflecting synchronous contraction within the LV (Figure 7-3).

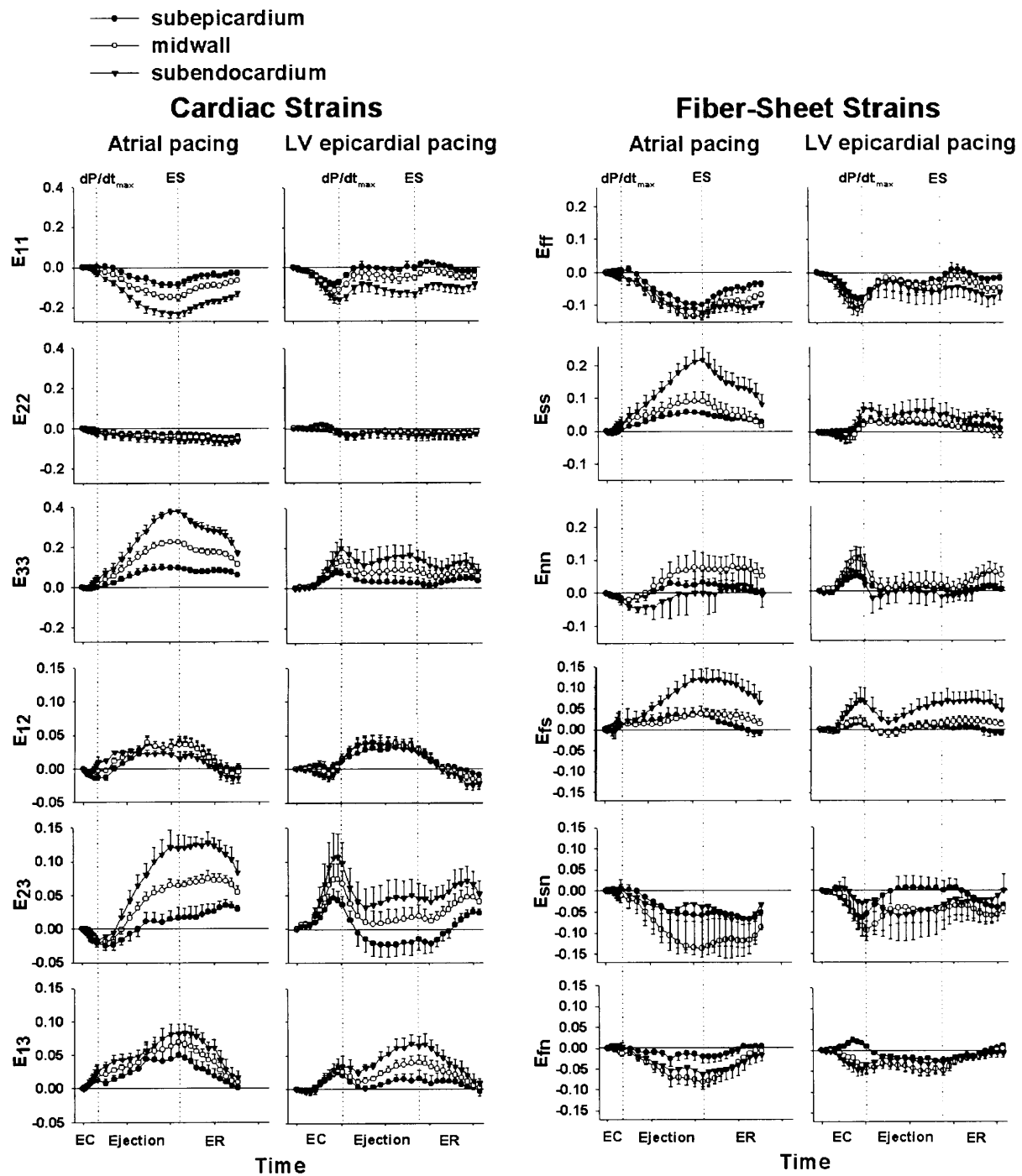


Figure 7-3: Temporal sequence of each strain component. Values are means \pm SE (n=5). Subepicardium, midwall, and subendocardium represents 25%, 50% and 75% wall depth from the epicardial surface, respectively. The reference state for strain calculation was end-diastole for both atrial pacing (peak of the ECG R-wave) and LV epicardial pacing (V-spike). dP/dt_{max} : the timing of LV peak positive dP/dt , ES: end-systole, EC: early contraction, ER: early relaxation. Note different scales for shear and normal strains.

Epicardial pacing markedly changed the time course of all strain components in both cardiac and fiber-sheet coordinates, indicated by a significant interaction between the effects of pacing mode and time ($P < 0.05$). The hallmark effect of epicardial pacing was multiple phases

of deformation, which are exemplified by E_{ff} . The myofibers started to shorten immediately after the epicardial pacing pulse, while the LV was still in diastole. This early shortening occurred prior to ventricular ejection, and was at its maximum before dP/dt_{max} . The myofibers subsequently underwent elongation during the ejection phase, followed by shortening, which reached the next peak near end-systole. The myofibers then underwent stretch and shortening again, followed by another peak shortening during the ER period and subsequent stretch. Although the early peak shortening near dP/dt_{max} ($E_{ff} = -0.091 \pm 0.018$) was comparable to the end-systolic shortening with atrial pacing ($E_{ff} = -0.124 \pm 0.009$, $P = NS$), it clearly preceded aortic valve opening and did not contribute to ejection. The wall thickening that occurred at this time point also did not contribute to ejection. The subsequent peak shortening near end-systole ($E_{ff} = -0.055 \pm 0.031$) was significantly decreased ($P < 0.05$). The peak shortening during ER ($E_{ff} = -0.053 \pm 0.016$) was also significantly decreased compared with end-systolic shortening with atrial pacing ($P < 0.05$). Most strains exhibited multiple peaks of deformation similar to E_{ff} .

7.4.3 Transmural mechanical activation sequence at the pacing site

Epicardial pacing reversed the normal transmural sequence of fiber shortening at the pacing site (Figure 7-4, Table 7-3). With atrial pacing, t_m was 30 ± 8 ms earlier in subendocardium than in subepicardium ($P < 0.05$), reflecting the normal electrical activation sequence in the endocardial-epicardial direction.

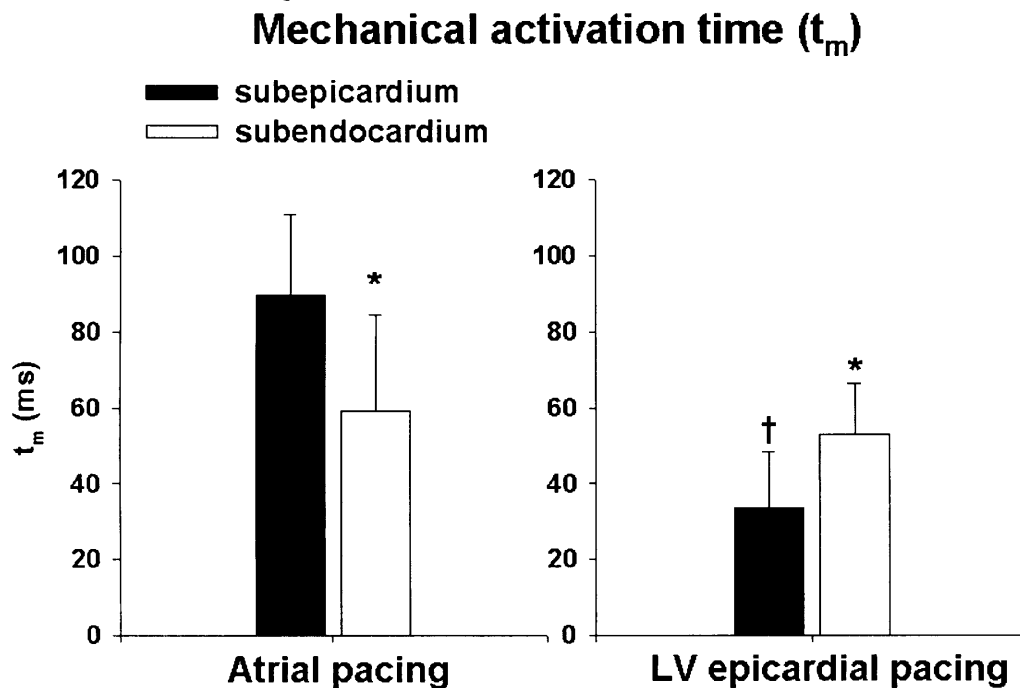


Figure 7-4: Transmural delay in mechanical activation time (t_m). Values are means \pm SE ($n=5$). Subepicardium and subendocardium refer to 25% and 75% wall depth, respectively. End-diastole was used as the reference state (time = 0) for both atrial pacing and LV epicardial pacing. Maximum fiber shortening in atrial pacing and LV epicardial pacing was found near end-systole and peak positive dP/dt (dP/dt_{max}), respectively. *: $P < 0.05$ vs. subepicardium of the same pacing mode, †: $P < 0.05$ vs. subepicardium of atrial pacing.

Epicardial pacing significantly reduced t_m in subepicardium ($P < 0.05$), whereas subendocardium was unaffected ($P = NS$). The net result was reversal of the transmural sequence of fiber shortening; subepicardial fiber shortening occurred 19 ± 5 ms earlier than subendocardial counterpart ($P < 0.05$, Figure 7-4).

	Atrial pace	Epicardial pace
E'_{11}	-0.042 ± 0.009	$-0.024 \pm 0.004^*$
E'_{22}	-0.023 ± 0.007	$-0.002 \pm 0.002^*$
E'_{33}	0.045 ± 0.008	$0.016 \pm 0.003^*$
E'_{12}	0.019 ± 0.004	$-0.002 \pm 0.003^*$
E'_{23}	-0.004 ± 0.006	0.007 ± 0.003
E'_{13}	0.022 ± 0.005	$0.003 \pm 0.002^*$
E'_{ff}	-0.024 ± 0.003	-0.020 ± 0.003
E'_{ss}	0.029 ± 0.006	$0.006 \pm 0.004^*$
E'_{nn}	-0.026 ± 0.009	$0.003 \pm 0.004^*$
E'_{fs}	0.014 ± 0.005	$0.004 \pm 0.003^*$
E'_{sn}	-0.017 ± 0.011	-0.006 ± 0.003
E'_{fn}	-0.022 ± 0.005	$-0.005 \pm 0.003^*$

Table 7-3: Transmural mechanical activation strains (E'). Values are transmural average (subepicardium, midwall and subendocardium) \pm SE (n=5). *: $P < 0.05$ vs. Atrial pace.

Because the reference and deformed configurations of E' strains were defined by transmural changes of fiber strains, fiber shortening (E'_{ff}) was not affected by reversal of transmural mechanical activation sequence ($P = \text{NS}$). Despite normal fiber shortening, most E' strains were significantly reduced ($P < 0.05$), including wall thickening (E'_{33}), sheet extension (E'_{ss}) and sheet thickening (E'_{nn}). However, transverse shear (E'_{23}) and sheet shear (E'_{sn}) were not significantly altered by reversal of transmural mechanical activation sequence ($P = \text{NS}$).

7-5 Discussion

Although the effect of LV epicardial pacing on fiber strain has been described at single selected layers at the pacing site, including the subepicardium (75, 199) and midwall (168, 200, 251, 252), the present study is the first to examine the transmural gradient of fiber-sheet strains at the pacing site.

7.5.1 Mechanism of impaired endocardial wall thickening at the epicardial pacing site

Based on reduced transverse shear deformation at the epicardial pacing site, it was hypothesized that impaired end-systolic wall thickening results from reduction in myocardial sheet shear. However, the results indicate that impaired end-systolic wall thickening at the epicardial pacing site was not due to selective reduction of sheet shear, but rather resulted from overall depression of sheet deformation. In fact, all end-systolic fiber-sheet strains were significantly depressed by epicardial pacing (Table 7-2). Relative contributions of sheet shear, sheet extension or sheet thickening to wall thickening were consistent with the results of Costa *et al.* (66), and were not altered significantly by epicardial pacing. These findings imply that impaired wall thickening results from lack of effective myocardial deformation, most likely due to insufficient calcium levels at end-systole at the pacing site. Intracellular calcium levels at the pacing site may be depleted by the time LV reaches end-systole, because the pacing site initiates contraction earlier than the rest of the ventricle, and the time interval from electrical activation to end-systole is significantly increased (ED-ES duration, Table 7-1). Moreover, early myofiber shortening at a pacing site is unloaded (131, 200), and unloaded shortening is associated with increased rates of decay of intracellular calcium transient (255).

7.5.2 Reversal of transmural mechanical activation

The measurements demonstrate that epicardial pacing reversed the transmural mechanical activation sequence, resulting in an earlier onset of myofiber shortening in the epicardium. Notably, this is the first study to show that the onset of fiber shortening in the subendocardium leads that of the subepicardium, and that this mechanical sequence is reversed when the transmural sequence of activation is reversed with epicardial pacing. To assess the effect of reversed transmural mechanical activation sequence on transmural deformation, transmural mechanical activation strains (E') was defined, which describe mean transmural myocardial deformation when mechanical activation travels between subendocardium and subepicardium. Because transverse shear (E'_{23}) and sheet shear deformation (E'_{sn}) were not affected by epicardial pacing, these shear deformations do not depend on the transmural sequence of mechanical activation, but depend on the magnitudes of fiber shortening. This finding implies that the direction and the magnitude of sheet shear deformation may be determined by local anatomy, and supports the concept that sheet shear deformation is required for normal systolic wall thickening (66, 150, 151, 222). In contrast, other E' strain components were significantly depressed by epicardial pacing. For example, sheet extension (E'_{ss}) and wall thickening (E'_{33}) were significantly reduced, when 'afterload' is low. These results suggest that a normal transmural mechanical activation sequence may be required for normal sheet extension and therefore wall thickening. Normal endocardial-epicardial activation sequence may allow optimal coordination of sequential fiber shortening and sheet mechanics across the wall to maximize wall thickening.

7.5.3 Limitations

The data describes transmural mechanics in the LV mid-anterior wall from epicardium to 90% wall depth. Regional and transmural variations should be taken into consideration when these results are extrapolated to other regions of the LV, such as the lateral, posterior wall and the septum. In addition, the 3-D finite strains that we measured in open-chest, anesthetized dogs may not accurately reflect the transmural mechanics in closed-chest, conscious animals. Lastly, the magnitude of baseline dP/dt_{max} and dP/dt_{min} was relatively high for open-chest dogs in this study, most likely due to dopamine use in two out of five animals during surgical procedure, which may have affected the normal transmural mechanics. To minimize the confounding effects of surgery, anesthesia, and dopamine between normal AV conduction and epicardial pacing, two pacing modes were studied consecutively in a short period of time.

7.6 Conclusions

Impaired end-systolic wall thickening at the epicardial pacing site is not due to selective reduction of sheet shear, but rather results from overall depression of fiber-sheet deformation, and relative contributions of sheet strains to wall thickening are maintained. These findings suggest lack of effective end-systolic myocardial deformation at the pacing site, most likely because the pacing site initiates contraction significantly earlier than the rest of the ventricle. Epicardial pacing also induced reversal of the transmural mechanical activation sequence, which significantly depressed sheet extension and wall thickening early in the cardiac cycle, whereas transverse shear and sheet shear deformation were not affected. These findings suggest that normal sheet extension and wall thickening immediately following activation may require normal transmural activation sequence, while sheet shear deformation may be determined by local anatomy.